T2R2 東京科学大学 リサーチリポジトリ
Science Tokyo Research Repository

論文 / 著書情報
Article / Book Information

題目(和文)	光活性なヘキサアザフェナレン配位子からなるネットワークとその応用
Title(English)	Photoactive Hexaazaphenalene Ligand-based Frameworks and Their Applications
著者(和文)	KrittanunDeekamwong
Author(English)	Deekamwong Krittanun
出典(和文)	学位:博士(理学), 学位授与機関:東京工業大学, 報告番号:甲第11880号, 授与年月日:2021年3月26日, 学位の種別:課程博士, 審査員:河野 正規,石谷 治,岩澤 伸治,川口 博之,植草 秀裕
Citation(English)	Degree:Doctor (Science), Conferring organization: Tokyo Institute of Technology, Report number:甲第11880号, Conferred date:2021/3/26, Degree Type:Course doctor, Examiner:,,,,
学位種別(和文)	博士論文
Type(English)	Doctoral Thesis

Powered by T2R2 (Science Tokyo Research Repository)

Doctoral Thesis

Photoactive Hexaazaphenalene Ligand-based Frameworks and Their Applications

Krittanun Deekamwong

Department of Chemistry

Tokyo Institute of Technology

2020

STATEMENT OF CONTRIBUTION

I declare that all work described in this thesis was performed by myself except where otherwise stated and that this work has not been submitted in any form for another dissertation or diploma at any other institution. Information derived from the publication or unpublished work of others has been acknowledged in the text and a list of references provided.

Krittanun Deekamwong

Dec 2020

ABSTRACT

Photo-induced reactive oxygen species (ROSs) generated by photosensitizers (PSs) are widely employed for chemical transformations which involve oxidation processes. Porous coordination networks (PCNs) are a class of molecular materials that have been successfully utilized as heterogenous photosensitizers. However, introduction of desired functionalities into PCN structures, to create materials with specific properties, remains a challenging task. The aim of this thesis is to develop a novel photosensitizer system based on tris(4-pyridyl) hexaazaphenalene (TPHAP) molecule and incorporate it into heterogeneous PCN scaffolds. The structural and physical properties of the resultant materials were interrogated using a variety of techniques, and their ability to promote photooxidation reactions was explored.

Chapter 1, The background of phenalenyl and pyridinium chemistries, as well as the role of reactive oxygen species in photoredox-catalyzed reactions are introduced. In addition, the field of molecular photosensitizers and their applications to photooxidation of alkanes is outlined.

Chapter 2, The generation of reactive oxygen species via photochemical charge transfer and energy transfer processes from the excited state of TPHAP were explored using a selective photooxidation reaction, scavenger agents and spectroscopic analysis. TPHAP-based porous coordination network was synthesized, characterized by X-ray diffraction analysis, and applied for photooxidation reactions.

Chapter 3, Pyridinium-based TPHAP derivatives were synthesized via the N-alkylation reaction of terminal substituted pyridyl groups to modify the electronic and redox properties of the parent molecule. The crystal structure analysis revealed a plethora of additional interactions compared to TPHAP. The spectroscopic and electrochemical properties of the resultant compounds were investigated by UV-Vis spectroscopy, cyclic voltammetry, spectroelectrochemical analysis and DFT calculation.

Chapter 4, Pyridinium-TPHAP analogues featuring free carboxylate/carboxylic acid groups were prepared by hydrolysis of the corresponding esters or direct N-alkylation reaction.

Their reactions with various transition metal salts were explored for the purpose of generating coordination networks. The resultant compounds were characterized by X-ray diffraction and spectroscopic analysis and further applied for the photooxidation of 1,5-dihydroxynaphthalene.

Chapter 5, A summary of the research results is provided with the discussion of their significance. The future directions for this research topic are outlined.

TABLE OF CONTENTS

LIST OF FIGURES

LIST OF SCHEMES

LIST OF TABLES

Chapter 1

General Introduction

1.1 Chemistry of Phenalenes

Phenalene is a polycyclic aromatic hydrocarbon with molecular formula of $C_{13}H_{10}$, which was first reported in 1944.[1] It can be deprotonated by a strong base, such as methoxide or benzenide to turn into phenalenyl anion.[2] These two compounds, phenalene and phenalenyl anion, can be readily oxidized by air and change to a phenalenyl radical which has a highly symmetric (D_{3h}) structure. As shown in Figure 1-1, the resonance structure of this radical specie contains an unpaired electron delocalized between C1, C3, C4, C6, C7 and C9 positions. The nature of its singly occupied molecular orbital (SOMO) indicates that the non-bonding character provides the same π-electron delocalization energy for all redox states, namely cation, neutral radical and anion, as determined from the Hückel molecular orbital calculations. As a result of these electronic structures, the phenalenyl radical shows a long-term stability in the absence of air.[3, 4] There has been an immense interest in the unique electronic and physical properties of this system, with numerous experimental and theoretical studies reported to date.[5-9] As a result, these compounds offered a new type of stable organic radical with great potential in several applications, such as optoelectronic and spintronic devices, ferromagnets, conductive materials, thermochromic devices, two-photon absorption and field-effect transistors.[10-19]

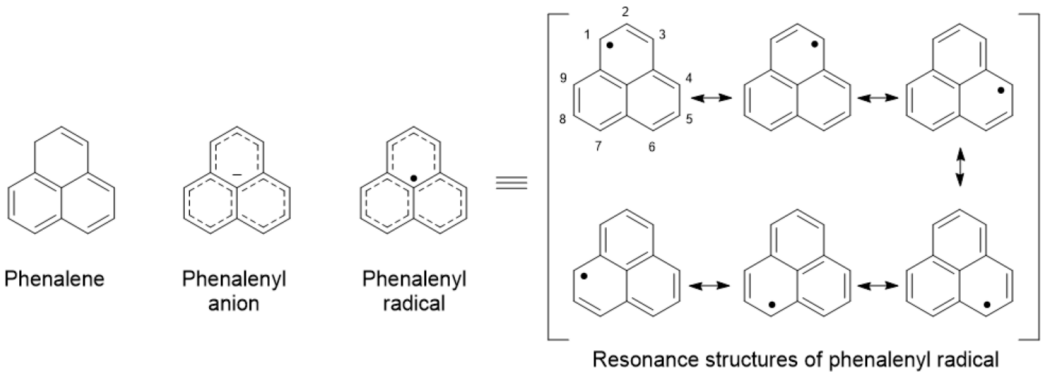

Figure 1-1 Phenalene, phenalenyl anion and resonance structures of phenalenyl radical.[3]

Some phenalene-based systems have severe drawbacks due to difficult synthesis, poor stability, and propensity of their radicals to dimerize, which limits their practical use. These deleterious characteristics can be partially ameliorated by addition of suitable substituents to their core structure. For example, as shown in Figure 1-2, the results reported by Ouyang and Morita showed that the introduction of bulky tertiary butyl groups at C2, C5 and C8 positions helped to stabilize phenalenyl radicals. Another derivative, containing nine bulky chloro groups, was synthesized by Haddon. These molecules could be isolated in sufficient quantities to analyze their crystal structures, and electronic and redox properties.[11, 12, 20]

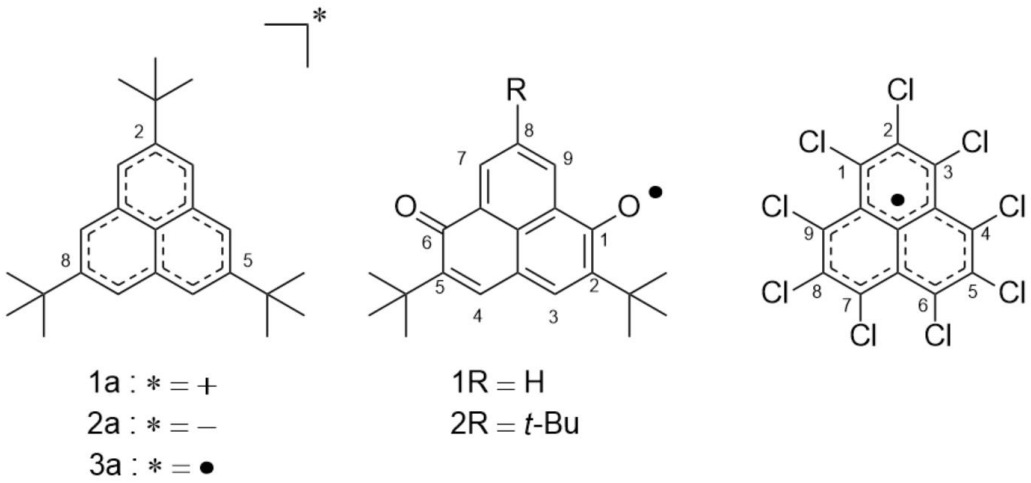

Figure 1-2 Examples of phenalenyl radical derivatives with bulky *t*-butyl and chloro groups.[11, 12, 20]

In addition, replacement of carbon atoms in the phenalenyl core with more electronegative nitrogen, as shown in Figure 1-3, has also be demonstrated to be highly effective in improving the stability. Morita *et. al.* reported synthesis and single crystal structures of a series of 1,3-diazaphenalenyl analogues, which contained nitrogen atoms at C1 and C3 positions. They found that the presence of nitrogen offered enhanced stability of the resultant radical species due to lowering of the HOMO energy levels.[21, 22] In other reports, Zheng *et. al.* obtained mono- and tri-substituted nitrogen-containing phenalenyl radicals, 2-azaphenalenyl and 2,5,8-

triazaphenalenyl, which were found to be more resistant toward dimerization relative to the purely carbon-based compounds.[23, 24]

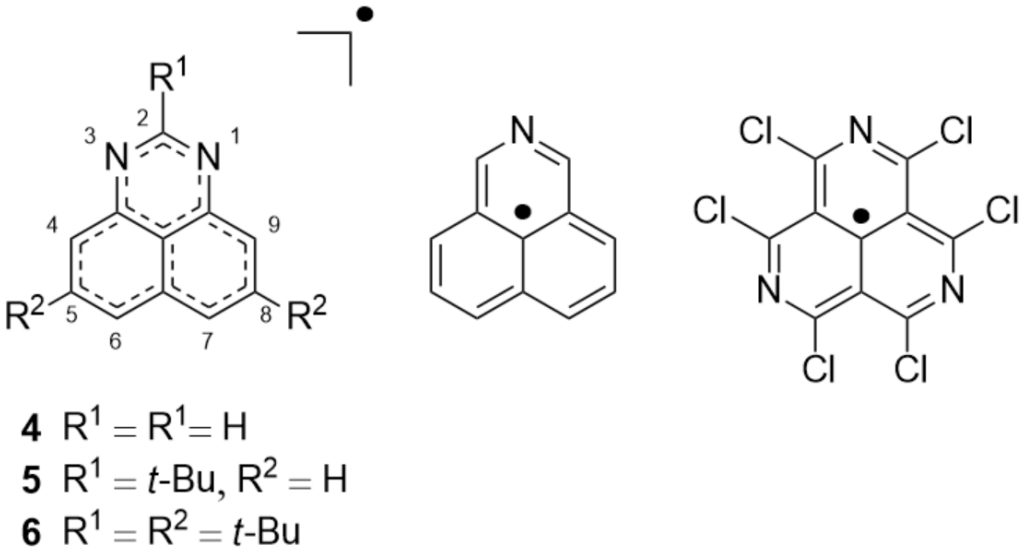

Figure 1-3 Examples of nitrogen-containing phenalenyl radicals.[21-24]

An even more heavily nitrogen substituted analogue, 1,3,4,6,7,9-hexaazaphenalene (HAP) anion, was first synthesized by Tomlin in 1965 to be used as a ligand in coordination complexes. Its chemistry was investigated in greater detail by Suzuki *et. al.* HAP is a highly symmetric heterocycle with six nitrogen atoms featuring lone-pairs parallel to the plane of the molecule that can form coordination bonds with metal ions. In addition, the HAP anion displayed exceptionally high stability among the phenalenyl anions due to its significantly lowered HOMO energy level. Structures of potassium salt of HAP, K[HAP], and its complex with Cu(II), $[Cu(NH_3)_4(HAP)_2]$ revealed the presence of multiple intermolecular and intramolecular interactions: 1) π-π stacking of HAP molecules, 2) hydrogen bonds, and 3) Cu-N coordination bonds.[25, 26]

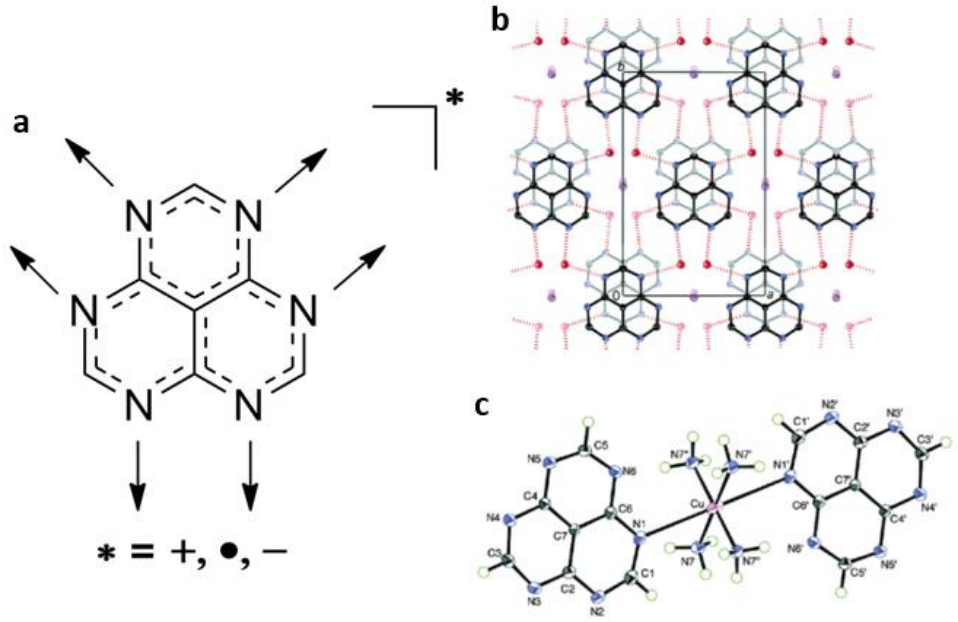

Figure 1-4 a) The structure of HAP, b) the crystal structure of K[HAP] showing π-π stacking and hydrogen bonding interactions and c) The crystal structure of $[Cu(NH_3)_4(HAP)_2]$ complex, showing coordination bonds between Cu and HAP; C – gray, N – blue, O – red, K – purple and Cu – magenta.[25]

The conventional methods for the synthesis of phenalenyl systems are limited in their low product yields and difficulties of introducing new functionalities to the HAP core. An important breakthrough was achieved by Morita who developed a new approach using one-pot condensation of corresponding amidine and tricyanomethanide in *N*,*N*′-dimethylacetamide as a solvent. This method enabled substitution of different groups at 2, 5 and 8 positions, and improved overall product yield.[27] The synthetic procedure was further developed by Yakiyama *et. al.*, who synthesized a pyridyl analogue, 2,5,8-tris(4-pyridyl) hexaazaphenalene (TPHAP), as a potassium salt. The procedure involves a solvent-free reaction between tricyanomethanide and pyridine-4-carboximidamide hydrochloride at 200 °C, which provides K[TPHAP] in superior yields compared to earlier solvent-based methods.[28]

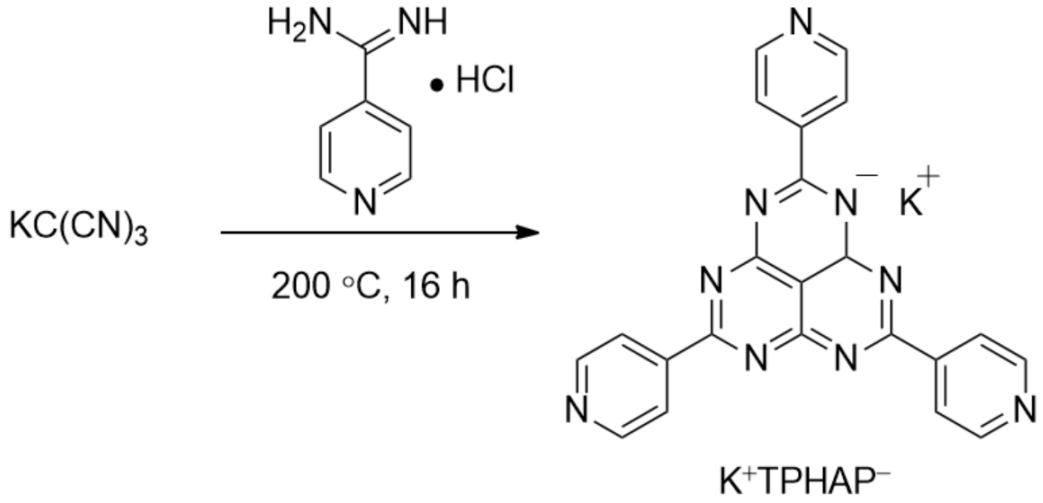

Scheme 1-1 One-pot synthesis of K[TPHAP].[28]

Due to the presence of the three pyridyl groups around the HAP skeleton, TPHAP was investigated as a bridging ligand to form coordination networks. Variations of the metal centers and crystallization conditions resulted in a wide array of network structures. Reaction of K[TPHAP] and $Co(NO_3)_2 \cdot 6H_2O$ in a methanol/nitrobenzene solution at 14 °C using layer-by-layer diffusion generated a kinetic porous coordination network, $[Co(TPHAP)_2(MeOH)(H_2O)]\cdot$solvent, which consisted of one-dimensional Co(II) chains connected by one monodentate and two bidentate TPHAP anions. This metastable phase underwent a transformation to another structure on the crystal surface after a few days corresponding to the thermodynamic network, as shown in Figure 1-5. The structure of the transformed crystal was $[Co(NO_3)(TPHAP)(MeOH)_2]\cdot$solvent and consisted of one-dimensional Co(II) chains bridged by bidentate TPHAP anions. During structural change, NO_3^- displaced monodentate TPHAP anions and water molecules around the cobalt centers in the original kinetic structure. This result indicated that the multi-interactive nature of the TPHAP ligand can efficiently trap and crystallize intermediate kinetic states that occur during network formation.[28]

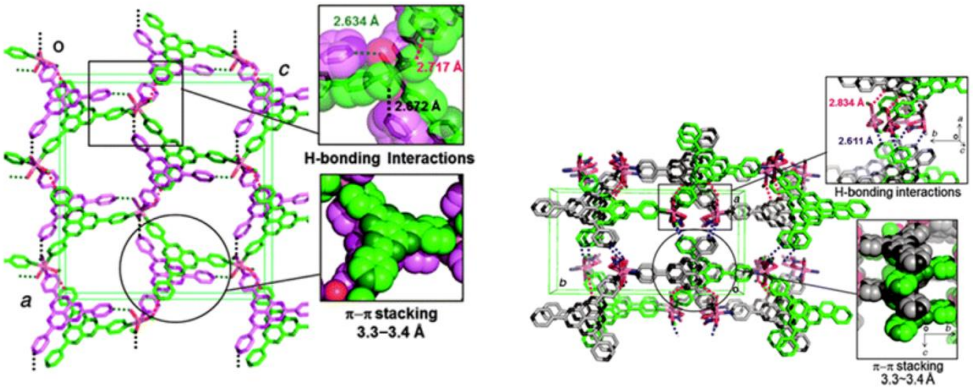

Figure 1-5 The structure of the kinetic $[Co(TPHAP)_2(MeOH)(H_2O)]\cdot$solvent network (left) and its transformation to the thermodynamic $[Co(NO_3)(TPHAP)(MeOH)_2]\cdot$solvent network (right). Reproduced from ref 28 with permission from The Royal Society of Chemistry.

The favorable multi-interactive properties of TPHAP were taken advantage of in the reaction between ZnI_2 and K[TPHAP]. Simple variations of the reaction solvents led to the formation seven different coordination networks, as shown in Figure 1-6. The structures numbered **1**, **3**, **4** and **5** consisted of the same motif, [ZnI(TPHAP)], with different network packing. Interestingly, even changing the ratio of the mixed solvents used for the reaction, MeOH/PhOH, was sufficient to induce crystallization of different structures. These findings indicated that interactions between TPHAP anions and reaction solvent molecules via hydrogen bonding and π-π interactions could significantly alter network crystallization pathways.[29]

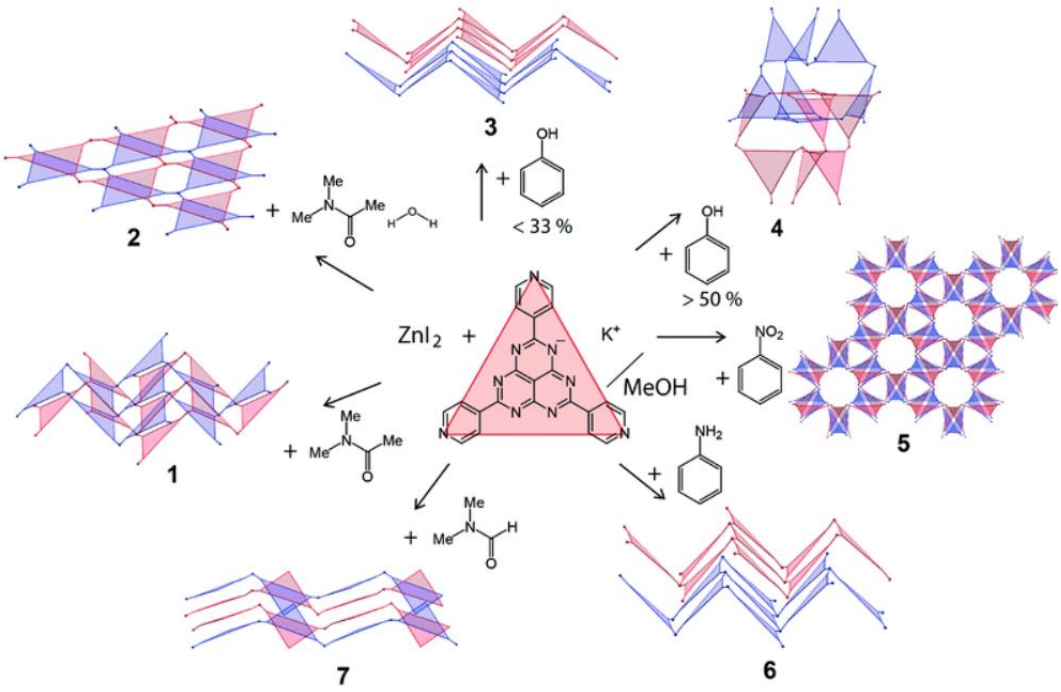

Figure 1-6 Diversity of networks obtained from K[TPHAP] and ZnI_2 in the presence of different additives. Reproduced from ref 29 with permission from The Royal Society of Chemistry.

The multi-interactive properties of TPHAP anion were also beneficial in other applications. Different crystalline phases of K[TPHAP] displayed different ion conductivities, as shown in Figure 1-7. When K[TPHAP] was first crystallized, its molecular packing exhibited a 1D-channel structure, with water molecules encapsulated through hydrogen bonding to nitrogen atoms on the HAP skeleton. The conductivity measurements of the pressed pellet of K[TPHAP] at 20 % relative humidity (RH) (structure **1**) showed that it was an insulator. When the RH was increased to 95 %, the conductivity increased to 3.4 $mS.cm^{-1}$. This transformation was caused by a structure change to a 2D layered packing (structure **2**). Upon dehydration of this 2D structure, a new phase appeared (structure **3**), which exhibited and insulating behavior.[30] To further expand the series of TPHAP-based ion conductors, ammonium and sodium salts of TPHAP were also synthesized. The molecular packing structures arising from different π-π stacking correlated with the stability of these salts and their humidity-dependent

conductivities.[31] In addition to the characterization in solid-state, the photophysical properties of K[TPHAP] in solution were explored by Nakanishi *et. al*. The absorption spectra contained a band at around 330 nm, which was assigned to the intramolecular charge transfer (ICT) transition from HOMO confined on the HAP skeleton and LUMO delocalized around the terminal pyridine units. Furthermore, the K[TPHAP] salt displayed emissive properties with unexpectedly large Stokes shifts of 5680-6650 cm^{-1} by excitation of the ICT transition.[32] The discovery of this emissive behavior in the TPHAP system makes it a suitable candidate as a light absorber in photochemical applications.

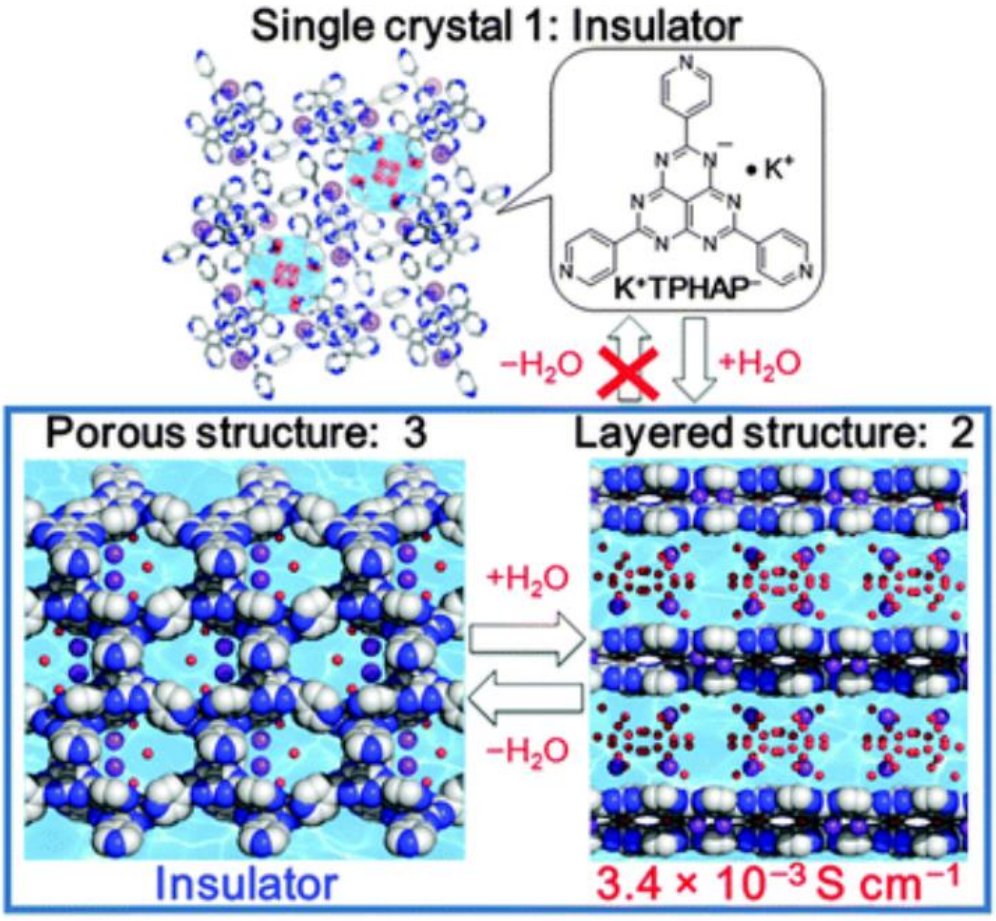

Figure 1-7 The structure transformation of K[TPHAP] depending on the humidity conditions and the accompanying changes in the ionic conductivities. Reproduced from ref 30 with permission from The Royal Society of Chemistry.

1.2 Pyridinium Chemistry

1.2.1 Background and Preparation

Pyridinium groups that contain a positively charged nitrogen centers are important components of many important chemicals, including natural products,[33-35] biologically-active compounds,[36-38] organic reagents,[39-44] and multi-stimuli-responsive materials.[45-50] Some pyridinium derivatives are also known as viologens. There are two general methods to prepare pyridinium compounds, as shown in Figure 1-8. The first route involves a S_N2 type reaction of pyridine with alkyl halides at elevated temperatures, which allows the preparation of alkyl pyridinium salts in one step.[51, 52] This synthetic strategy was widely applied to modulate the properties of viologen-based molecules by substituting different alkyl groups with varying chain length and steric bulk.[53, 54] The second commonly used synthetic procedure utilizes Zincke salt as a highly electrophilic intermediate that can be prepared from the reaction between pyridine groups and 1-chloro-2,4-dinitrobenzene, which is readily accomplished under conventional heating, microwave irradiation or ultrasound treatment.[55-57] In the second step, the dinitrobenzene group can be displaced with the appropriate amino derivative to get the corresponding pyridinium compound. This reaction is typically employed for the preparation of N-aryl pyridinium salts, such as π-extended viologens.[58-61] Several heterocyclic and polycyclic aromatic hydrocarbon moieties, including porphyrin,[62-66] thiophene,[67-69] thiazole,[70-72] pyrene,[73-75] triazine,[76-78] and triphenylamine,[79] which feature terminal pyridyl units were converted to the pyridinium salt, in order to improve their solubilities, photochemical properties, redox properties and catalytic activities. Importantly, Melánová *et. al.* found that the energy of intramolecular charge transfer transition of tris[(pyridine-4-yl)phenyl]amine experienced a redshift by 80 nm after conversion of pyridyl groups to pyridinium by N-alkylation.[80]

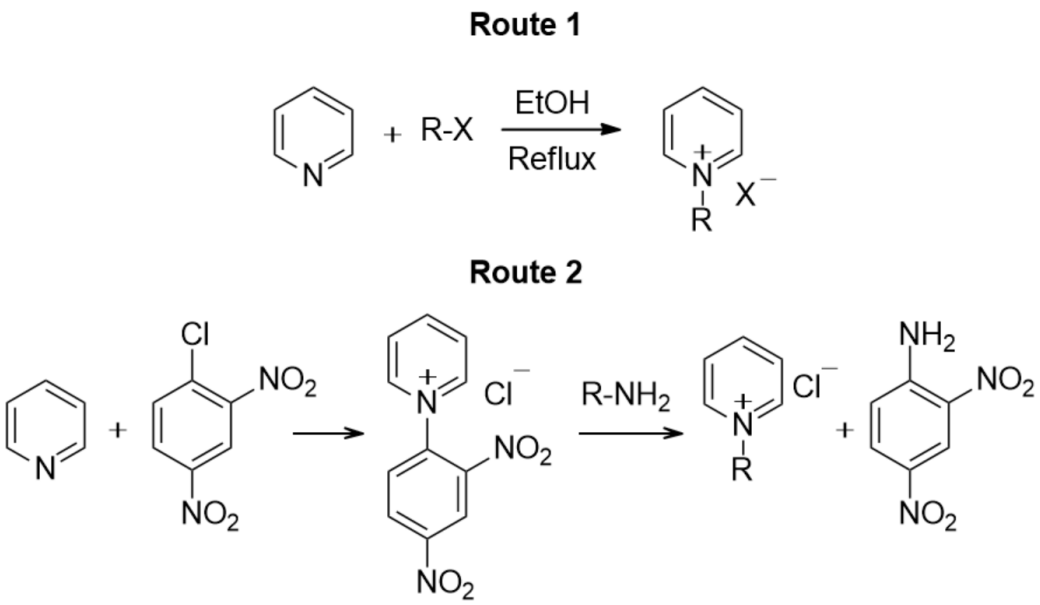

Figure 1-8 The common methods for pyridinium synthesis: route 1) N-alkylation with alkyl halides and route 2) Zincke reaction.

1.2.2 Application

1.2.2.1 Gas Separation

The separation of light gases and small hydrocarbons is an industrially important process because these compounds are used as feedstock for many chemical transformations.[81, 82] In order to isolate and purify these small molecules, absorption into porous materials is commonly utilized. There are several important considerations in the development of absorbents for a specific capture or separation task, including pore sizes, pore shapes and the availability of different interactive sites in the pore interior. Among several classes of porous materials, porous coordination networks (PCNs), also known as metal-organic frameworks (MOFs), and covalent-organic frameworks (COFs) are especially promising candidates because their chemical properties can be readily tailored for the desired application. To take the advantage of electrostatic interactions from positively charged pyridinium units, Higuchi *et. al.* reported the synthesis of [Zn_2(tpa)(cpb)], which incorporates two ligands, terephthalic acid (tpa) and 1-(4-carboxyphenyl)-4,4′-bipyridinium (cpb). This PCN was investigated as a

cationic molecular sieve. Methanol absorption and desorption experiments were carried out, which revealed that methanol adsorption isotherms exhibited a distinct hysteresis loop. The isosteric heat of adsorption was calculated to be in the range of 50-95 kJ.mol^{-1}, indicating a strong interaction between positive charges in the networks and methanol molecules compared to other alkaline cations.[83] Furthermore, Yuan *et. al.* investigated porous aromatic frameworks (PAFs) with anion-templated pore channels for separation of small gases. A series of PAFs was prepared with systematically varying pore sizes from 3.4 to 7.0 Å by changing the halide counter anion. Each material exhibited distinctive molecular sieving effect and was able to separate hydrogen, nitrogen, oxygen, methane, and carbon dioxide mixture. These results suggested that rationally designing the framework pore could yield beneficial properties for gas separation, particularly when involving size-exclusion effects.[84]

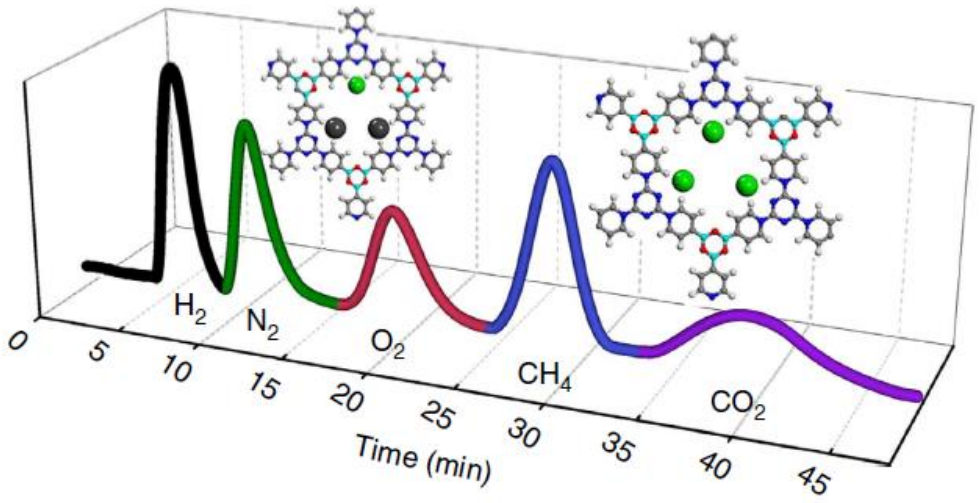

Figure 1-9 Gas chromatogram of the chloride and iodide templated pyridinium PAFs, showing the gas mixture separation. Reproduced from ref 84 with permission from Springer Nature.

1.2.2.2 Electrochromism

Materials that can change their properties when subjected to external stimuli have attracted considerable attention for potential application in memory devices,[85, 86] sensors[87] and electrochromic displays.[88, 89] The physicochemical properties of these molecules can be controlled and adjusted by application of external forces, such as light, pressure, electric field, heat or chemical additives.[90] Among numerous stimuli-responsive materials, viologen and its derivatives are particularly promising candidates because they undergo reversible one-electron reduction reactions at relatively mild potentials to form radical species. This redox change is often accompanied by a pronounced color change, a phenomenon known as electrochromism. One of the simplest derivatives, methyl viologen, shows a transition from colorless state for the dication to dark blue for the radical cation, and finally yellow for the neutral form. These states can be easily accessed by application of external potential.[91] Therefore, several viologen analogues, which were obtained by N-alkylation and allylation methods were investigated for their electrochromic properties and chemical/electro/photostability.[92-94] Recently, Woodward *et. al.* reported new viologen-based thiazole molecules that display strong fluorescence and electrochromism, as shown in Figure 1-10. The solutions of protonated, methyl, octyl, and benzyl substituted 2,5-bis(4-dipyridyl)thiazolo[5,4-*d*] thiazole (TTz^{2+}) undergo two reversible reduction peaks at potentials between -0.46 and -0.58 V vs SCE in DMSO supporting electrolyte, as measured by cyclic voltammetry. The absorption band at 616 nm attributed to the blue color appeared when reductive potentials were applied indicating a formation of the radical cation species in the first reduction process. Then, the second reduction at more negative potentials generated the diradical species, which has a strong adsorption band at 672 nm. Furthermore, the compounds exhibited changes of fluorescence behavior in solution. The electrochemical reduction of dication caused a significant drop in the emission intensity.[95]

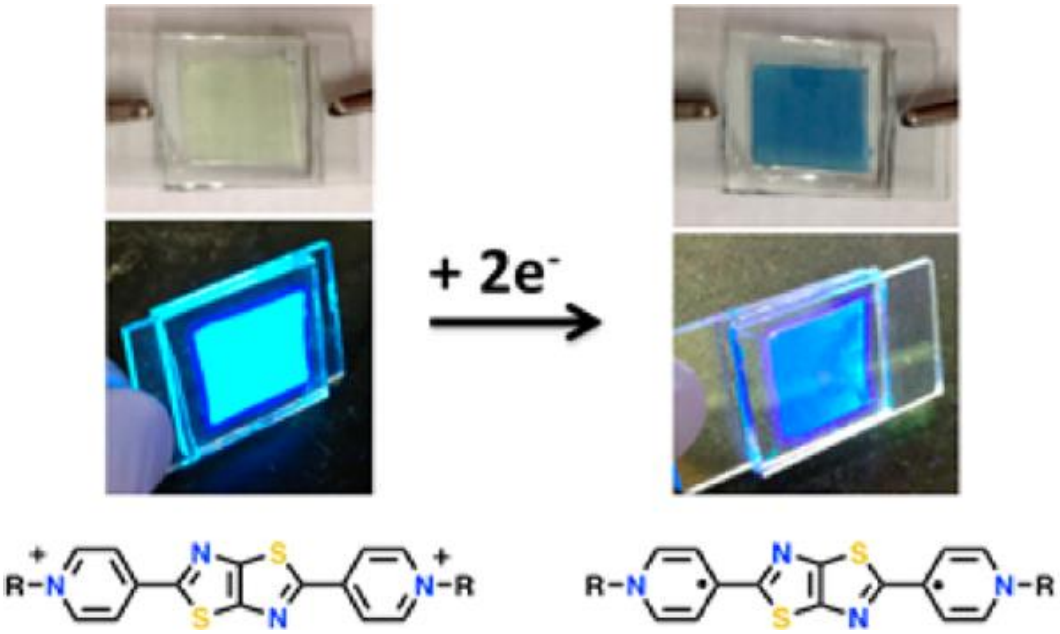

Figure 1-10 Images of neutral and reduced TTz^{2+} solutions in a transparent electrode window shown under ambient light (*above*) and under UV illumination (*below*), with the proposed reduced TTz structure. Reproduced from ref 95 with permission from American Chemical Society.

1.2.2.3 Catalytic Reactions

Pyridinium-based ionic liquids are widely used as solvents and catalysts, as shown in Figure 1-11.[96-98] The selective bromination of naphthalene by Br_2 in the presence of pyridinium as a solvent and an acid catalyst was reported to proceed with excellent yields. Similar to Fischer esterification of long chain aliphatic acids with alcohols, the Brønsted acidic ionic liquids (BAILs) proved to be highly active catalysts under ambient conditions with high isolated yields. A pyrrolidine-based chiral pyridinium compound was also prepared and applied for Michael addition of cyclohexanone to nitrostyrene. The pyridinium catalyzed reaction provided high product yields, high diastereoselectivities (*syn*/*anti* up to >99:1) and enantioselectivies (ee up to 99 %).

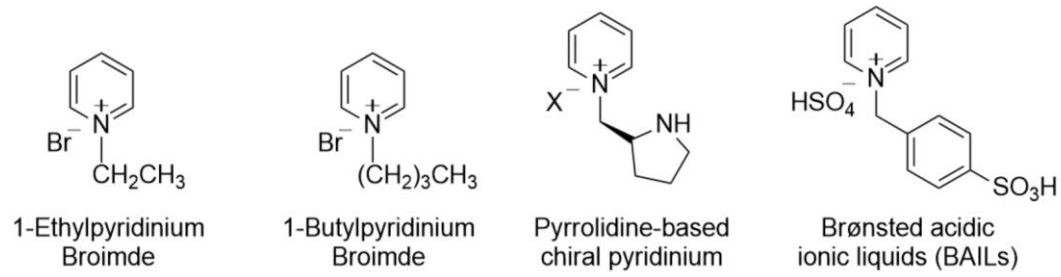

Figure 1-11 Examples of pyridinium-based ionic liquids that were used as catalysts.

Pyridinium salts were also investigates as organic electron donors (OEDs), which feature highly negative redox potentials allowing them to easily generate radicals or anionic intermediates by electron transfer. Due to their strong reductive potential, these compounds are attracting interests in several applications, such as polymerization initiators, greenhouse gas reduction, and reduction of arenes.[99-104]

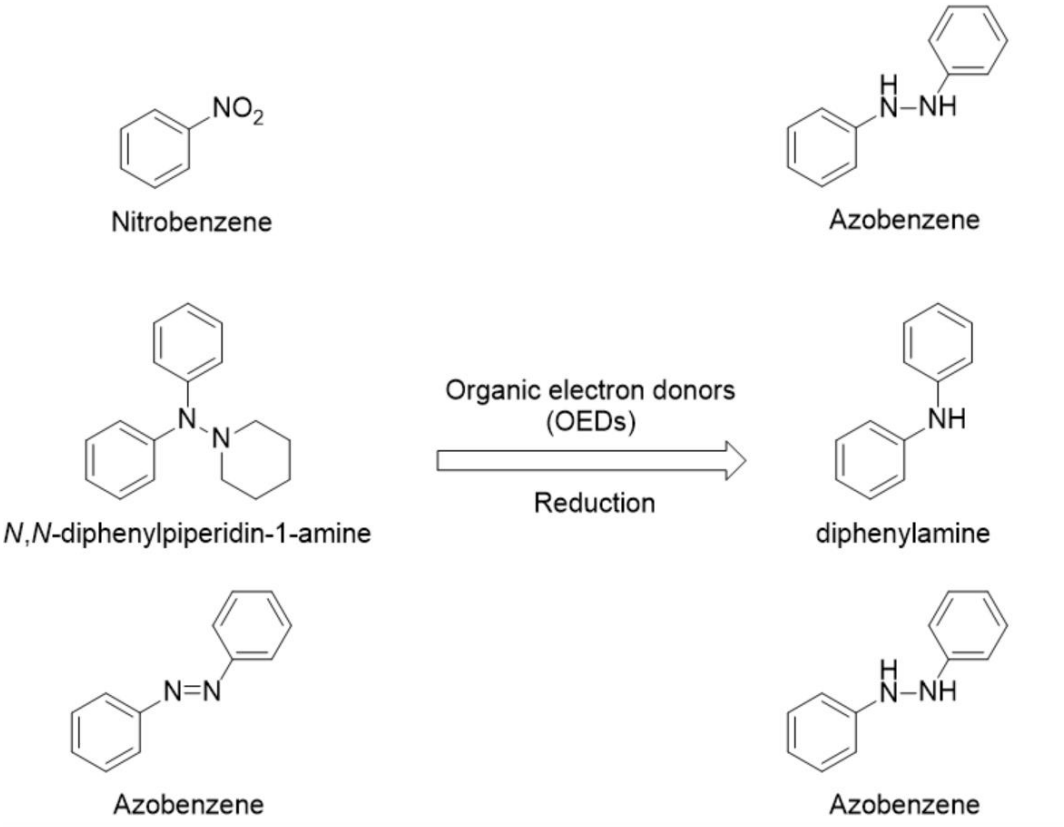

Figure 1-12 Reduction of nitroarenes, azoarenes and hydrazine by OEDs.[104]

N-methyl pyridinium carbonates (DMAP) were synthesized and thermally activated to generate a potent electron donor *in situ* by Tintori *et. al.* These DMAP species were introduced

for the reduction of various substrates in air, displaying full conversions for all substrates, except for naphthols, due to the protective effect of the adjacent alcohol group, as shown in Figure 1-13. These results demonstrated that this new generation of pyridinium OEDs could successfully handle oxygen-sensitive reactions, encouraging their broader utilization.[105]

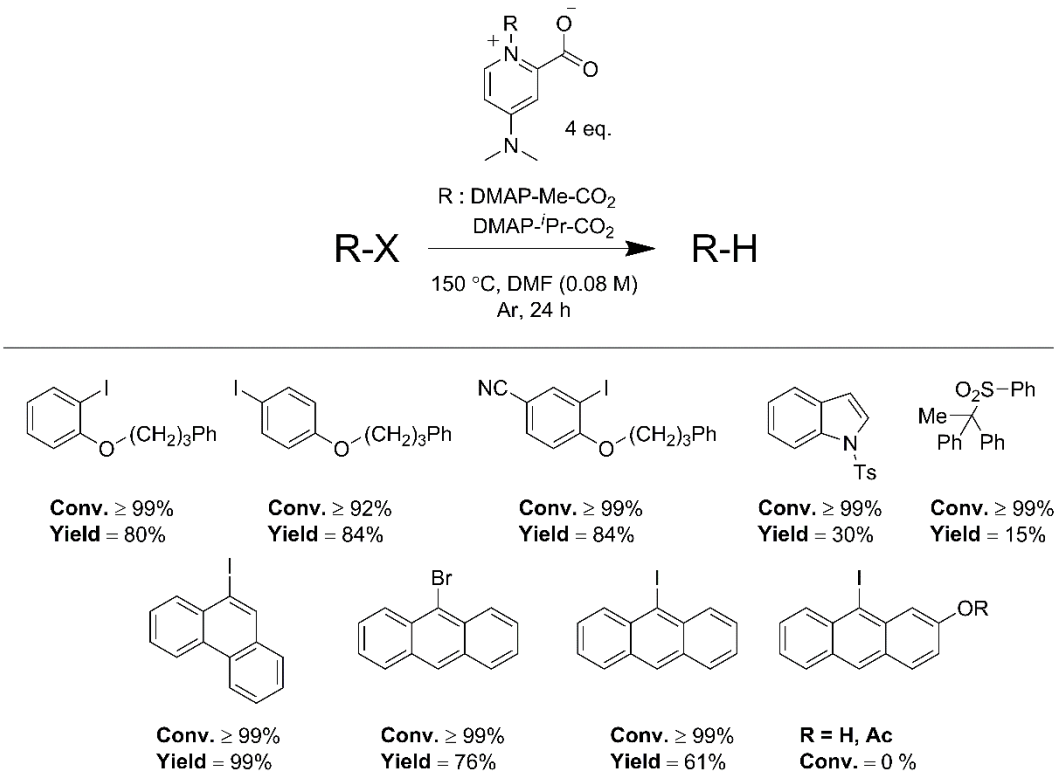

Figure 1-13 Reduction reactions catalyzed by pyridinium OEDs, showing a broad range of substrates.[105]

Recently, pyridinium salts have also been applied in radical reactions as radical reservoirs. A variety of N-functionalized pyridinium analogues have been modified to achieve site selectivity and generate radical species, such as alkyl, trifluoromethyl, N-centered radicals, and O-centered radicals. Basch *et. al.* reported nickel-catalyzed Suzuki-Miyaura cross coupling reactions of pyridinium salts with aryl boronic acids via the C-N bond activation of amines. The reaction mechanism involves pyridinium species **1** receiving one electron from a Ni(I) intermediate complex to form alkyl radical **3A**, which then undergoes the C-N bond dissociation to generate alkyl radical. Then, these radicals reform with a Ni(II) complex,

followed by reductive elimination to obtain the final coupled product **2**.[106] These radical generating abilities could also be applied to photoredox-catalyzed reactions, including deaminative alkylation,[107, 108] deaminative allylation,[109, 110] deaminative three-component dicarbofunctionalization,[111] and selective C−N borylation of alkyl amines.[112]

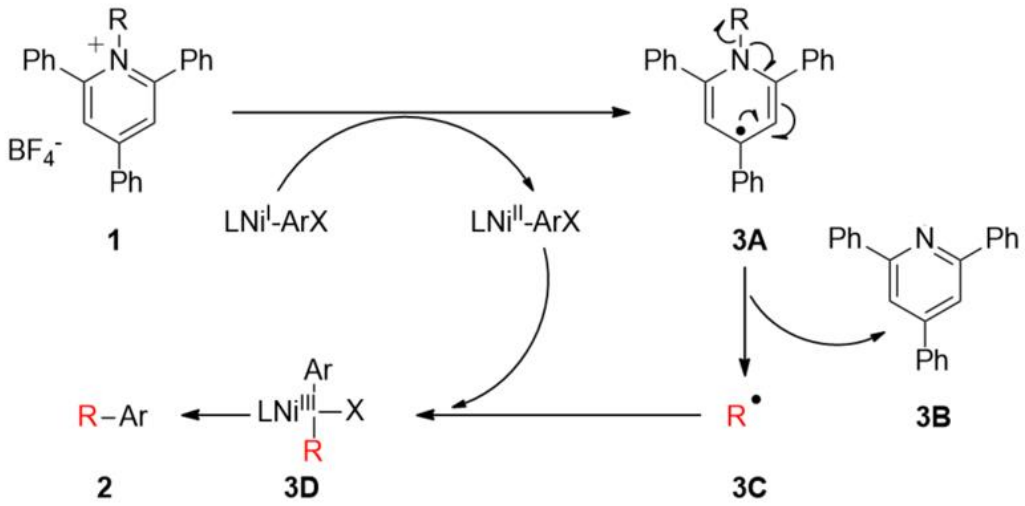

Figure 1-14 Nickel-catalyzed deaminative cross-coupling reaction of Katritzky salts and aryl boronic acids.[106]

1.3 Reactive Oxygen Species

Dioxygen has unique molecular properties and is one of the most abundant gases in the atmosphere. In the presence of external potential, such as chemical[113] or light, oxygen molecule can be converted into highly reactive states, with several possible reaction pathways depending on the availability of hydrogen atoms and radicals. Collectively, the resultant species are called reactive oxygen species (ROSs). The most convenient method for generation of ROSs is by using light irradiation (UV, visible light) in the presence of photosensitizers (PSs). Figure 1-15 depicts simple photochemical processes occurring during the photoexcitation of PSs. A ground state molecule (S_0) is promoted to an excited singlet state (S_1) by absorption of photon. This excited singlet state can undergo intersystem crossing (ISC) to the excited triplet state (T_1). A type I photochemical process involves electron transfer between the T_1 state of a PS and a substrate, such as small molecules or hydrocarbons. Molecular oxygen is a particularly potent electron acceptor as it is converted into radical-based ROSs, including superoxide radicals and hydroxyl radicals. A type II photochemical process involves the quenching of a triplet state by other paramagnetic species, especially the ground triplet state of oxygen molecule, which is then converted to the singlet oxygen, an example of non-radical-based ROS.[114]

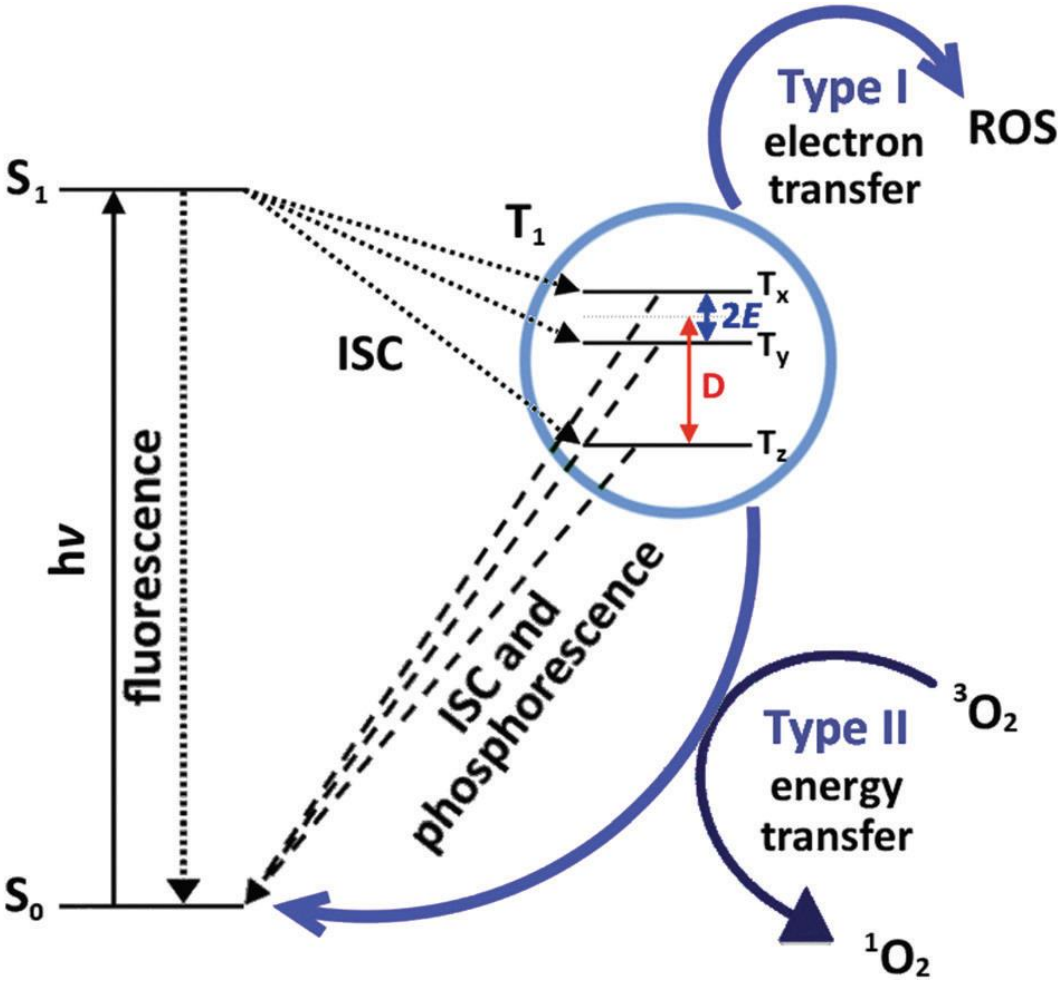

Figure 1-15 Jablonski diagram and accompanying photochemical processes after photoexcitation of a photosensitizer. Reproduced from ref 114 with permission from The Royal Society of Chemistry.

The ROSs generated by photoexcitation are widely used to drive various chemical transformations, with different reactivities depending on the type of ROSs. In the past, radical-based ROSs were applied for photodegradation of pollutants,[115] oxidation of alcohols,[116] amines,[117] alkenes and alkanes,[118] hydroxylation,[119, 120] C-C bond formation,[121] to name a few. On the other hand, singlet oxygen was shown to be effective for the endoperoxides reaction,[122] cycloaddition,[123] hydroperoxide addition to alkenes and phenols, sulfide and phosphine oxidation,[124] and C-H activation of ethereal hydrocarbons.[125]

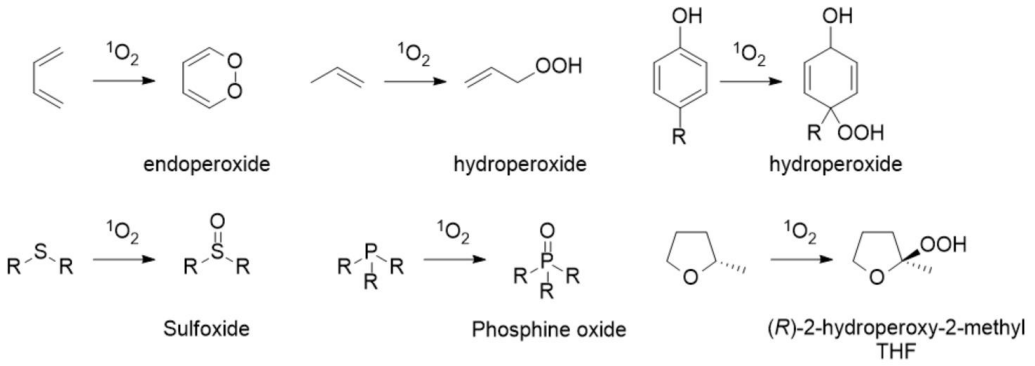

Figure 1-16 Reactions promoted by singlet oxygen.

1.4 Photosensitizers

The design of photosensitizers (PSs) with enhanced ROS generation abilities is an effective strategy for further improvements of the photocatalytic activities. It has been suggested that molecules with high molar extinction coefficients in the visible region, efficient ISC processes and long-lived triplet excited states are particularly suitable for the PS role.[126]

1.4.1 Classical Photosensitizers

Among several classes of PSs, transition metal complexes are unique since they possess many excited state electronic configurations and arrangements.[127] Importantly, the presence of heavy elements, such as Pt(II),[128] Ir(III),[129] Ru(II),[130] as well as iodo and bromo groups in some organic molecules[131] (Figure 1-17) enhances the ISC process due to the electrons in the frontier molecular orbitals generating large molecular orbit magnetic torque to flip the electron spin.[132] However, compounds containing these elements are highly cost inefficient, have low absorption coefficients and suffer from increased toxicity to be considered for further practical applications.

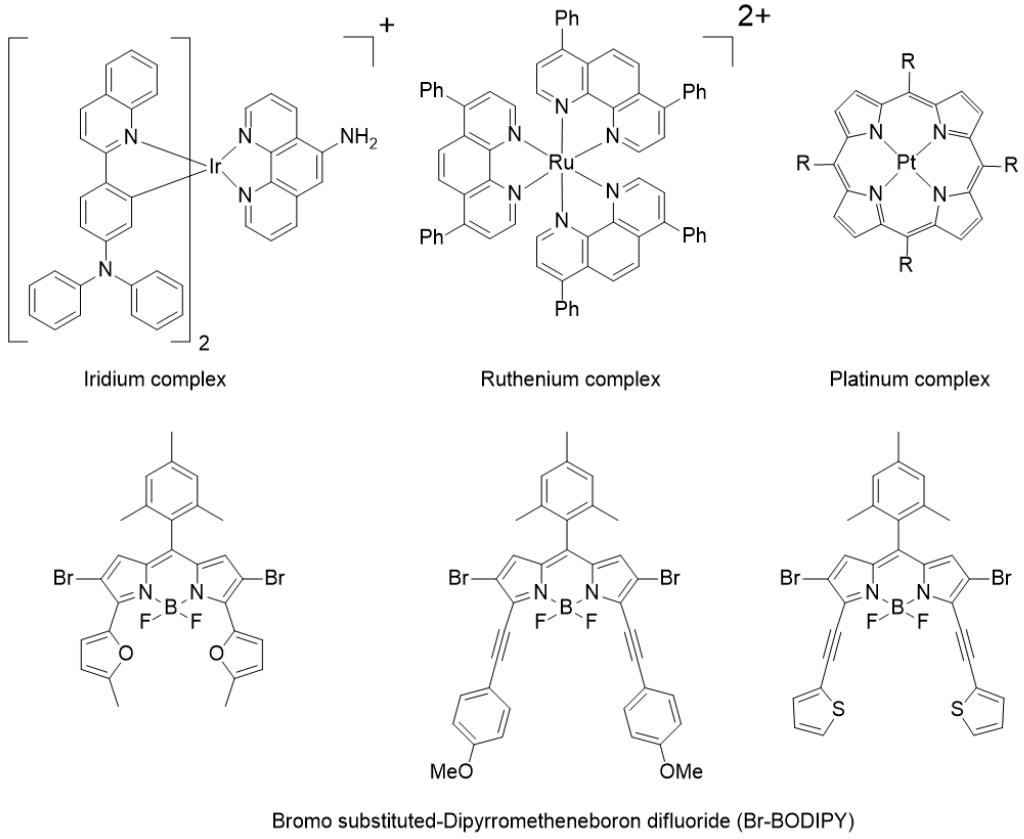

Figure 1-17 Examples of transition metal complexes and BODIPY analogues with bromo substituents that were used as PSs.

1.4.2 Heavy-Atom-Free Photosensitizers

To minimize these drawbacks, the development of PSs without heavy atoms is necessary. Several classes of purely organic molecules have been intensively studied and developed for this purpose.[132] General motifs, such as porphyrins,[133] chlorins,[134] methylene blue,[135] naphthalenediimide,[136] perylene bisimide,[137] anthracene,[138] BODIPY,[139] and phenalenone[140] have been explored for their ROSs generation properties and employed in various photochemical transformations. However, it is still a challenge to create heavy-atom-free PSs because the ISC process typically has low efficiency in the absence of a strong spin-orbit coupling effect.[141] Moreover, the ability to straightforwardly functionalize the PS skeletons is also important, as it allows for the direct control of their photophysical properties, which is necessary to achieve the desired performance.

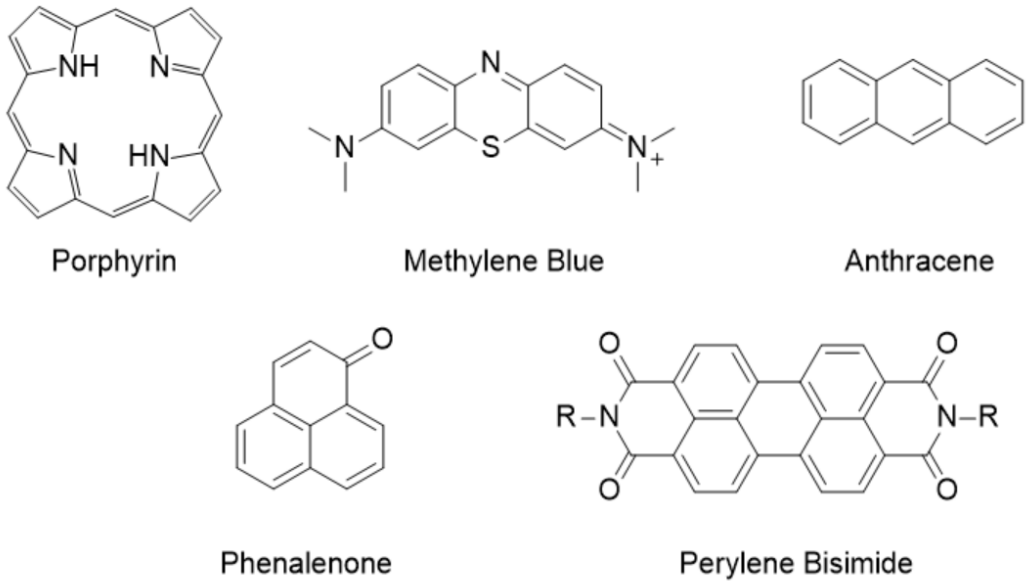

Figure 1-18 Common organic motifs that can be used as heavy-atom-free PSs.

1.4.3 Porous Coordination Networks

Heterogenous PSs offer several advantages over soluble molecules for catalyzing photochemical reactions since they can increase activity, limit degradation pathways, and simplify the sensitizer recycling[142]. Immobilization of conventional PS molecules into solid-state scaffolds, such as porous coordination networks (PCNs) is an effective strategy for the creation of such materials. In this case, PCN structures composed of photoactive bridging ligands and diamagnetic metal ions are constructed. This strategy permits ready functionalization of the ligand and therefore modulation of the network properties. Porphyrin-based ligands are particularly popular for the synthesis of PCNs because porphyrin macrocycle can be easily substituted with different coordinating groups, such as carboxylic acid,[143-145] tetrazole,[146] or pyridine,[147] as shown in Figure 1-19. In comparison, only a limited number of networks featuring perylenediimide, anthracene, and pyrene-based ligands were reported to date. Some examples include PCNs containing perylenediimide (FJI-Y10), anthracene (NNU-32, NNU-37) and pyrene (PCN-822, NU-1000).[148-152]

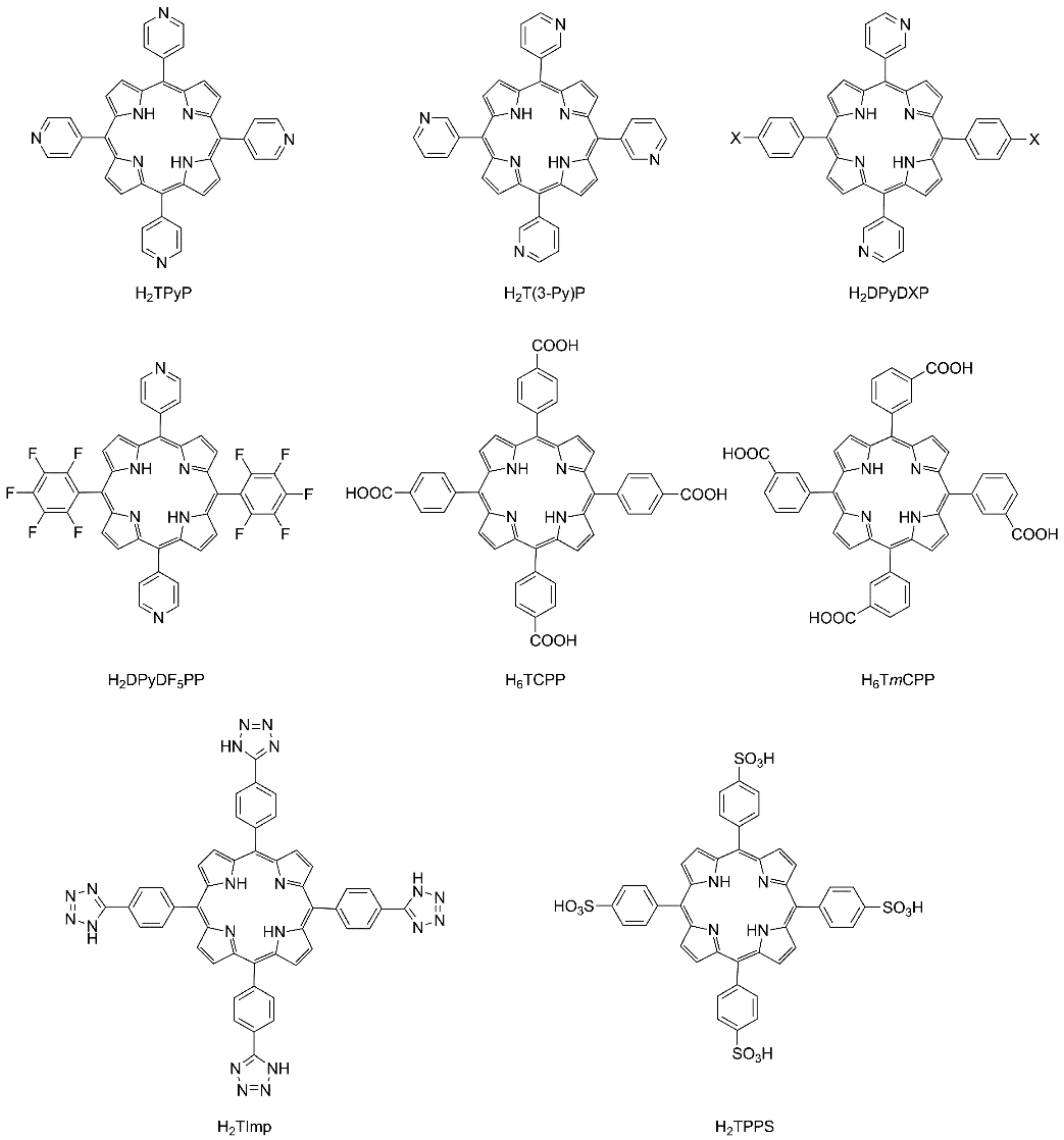

Figure 1-19 Examples of porphyrin-based ligands used for the construction of PCNs.[147]

1.5 Photooxidation of Alkanes

Photooxidation of alkanes catalyzed by both homogeneous and heterogeneous PSs was investigated for different catalytic systems, such as noble transition metal complexes,[153] metal oxides,[154] molecular cages[155] and organic molecules.[156] With the rapid advancements in PCN chemistry, several networks were investigated for their ability to catalyze oxidation of alicyclic alkanes, such as cyclohexane. Some of the materials used in these studies include UiO-66-NH_2(Zr),[118] MIL-125-NH_2(Ti),[157] and [Hf(TPY)] metal organic layer.[158] The functionalization of inert C-H bonds in small alkanes is exceedingly difficult because it has high activation barrier, which necessitates harsh synthetic condition and leads to unsatisfactory product selectivity. Therefore, the development of photocatalysts capable of efficient and selective oxidation of such substrates is still a formidable challenge.

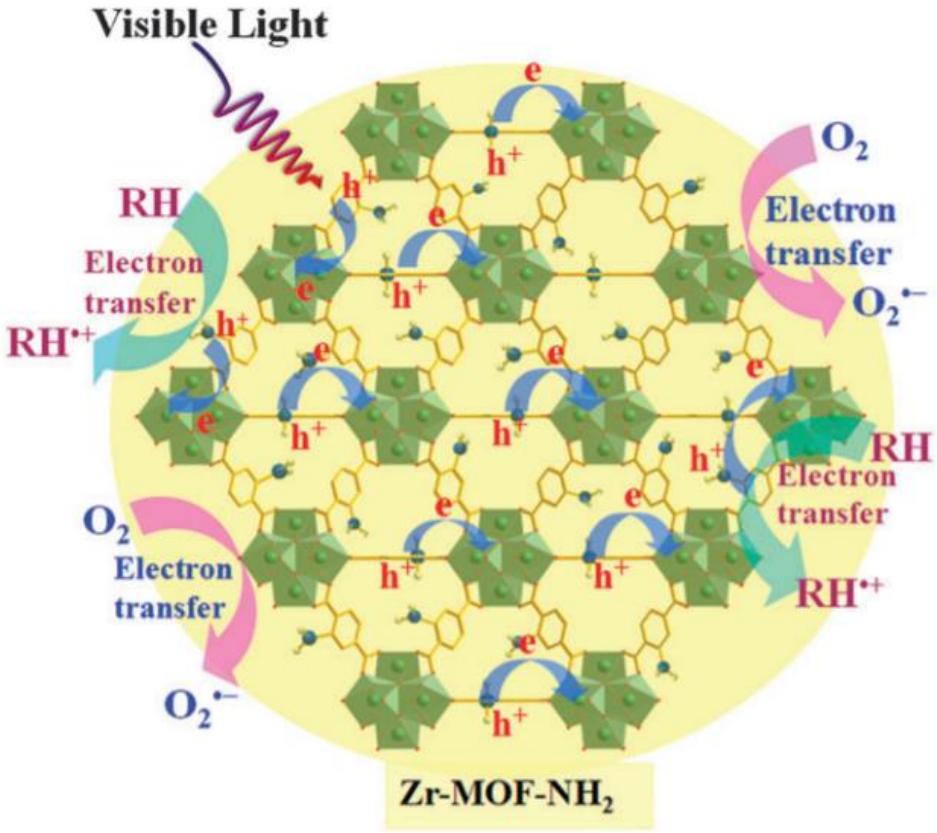

Figure 1-20 Proposed mechanism for the oxidation of hydrocarbons by UiO-66-NH_2; RH = hydrocarbon compound. Reproduced from ref 118 with permission from The Royal Society of Chemistry.

1.6 Scope of Thesis

This thesis describes the investigation of photochemical processes of TPHAP-based molecules as a novel photosensitizer system by chemical and spectroscopic methods. The parent TPHAP and pyridinium-TPHAP derivatives were synthesized and characterized for their structural and physical properties. These molecules were used as photocatalysts, both as soluble species and as part of a solid-state scaffolds, to promote photooxidation reactions.

Chapter 2, I prepared and characterized a tetrabutylammonium salt of TPHAP and incorporated it into cadmium-based porous coordination network, and then investigated their catalytic activity for alkane photooxidation reaction. The photochemical processes, including

charge transfer (Type I) and energy transfer (Type II) were explored by using selective photooxidation reactions, scavenger agents and spectroscopic analysis to evaluate the generated reactive oxygen species.

Chapter 3, I synthesized pyridinium-based TPHAP derivatives via the N-alkylation reaction of terminal pyridyl groups to modify the electronic and redox properties of the TPHAP system. The crystal structures of these compounds revealed a plethora of additional interactions, including electrostatic ion-ion interaction and weak hydrogen bonding, compared to the structure of the TPHAP salt. The changes of absorption spectra and reduction potentials were interrogated by UV-Vis spectroscopy, cyclic voltammetry, spectroelectrochemical analysis and DFT calculations.

Chapter 4, I prepared a pyridinium-based ligand, 2,5,8-tri(1-(4-carboxylatomethyl)pyridinium)-HAP by N-alkylation reaction with 2-bromoacetic acid, which was then incorporated into copper-based porous coordination network. Both the pyridinium ligand and the network were investigated for their catalytic activity towards a photooxidation reaction selective for the singlet oxygen. Their crystal structures of these compounds were obtained from the X-ray diffraction analysis.

Chapter 5, I summarized the key discoveries of this study, discussed its limitations, and proposed future direction for this research.

1.7 Publications and Presentations

Some aspects of this work have been published in peer-reviewed journals and presented at national and domestic conferences:

Publication:

1. K. Deekamwong, P. M. Usov, H. Ohtsu, M. Kawano, Pyridinium modification of a hexaazaphenalene skeleton: structure and spectroelectrochemical analysis, CrystEngComm, **2020**, 22, 5987-5994.

2. K. Deekamwong, P. M. Usov, H. Ohtsu, M. Kawano, Photoactive hexaazaphenalene ligand-based frameworks as a reactive oxygen species generator, in preparation

Presentation:

1. Deekamwong, K., Usov, P.M., Ohtsu, H., Kawano, M. Multi-interactive hexaazaphenalene-based pyridinium ligands and their incorporation into coordination networks. 7th Asian Conference on Coordination Chemistry 2019. 15-18 October **2019**, Kuala Lumpur, Malaysia. (Oral presentation)

2. Deekamwong, K., Nakanishi K., Ohtsu, H., Kawano, M. Photoactive hexaazaphenalene ligand-based frameworks and their applications. The 69th Conference of Japan Society of Coordination Chemistry. 21-23 September **2019**, Nagoya University, Nagoya, Japan. (Oral presentation)

3. Deekamwong, K., Nakanishi K., Ohtsu, H., Kawano, M. Multi-interactive hexaazaphenalene-based pyridinium ligands and their incorporation into coordination networks. CEMS International Symposium on Supramolecular Chemistry & Functional Materials 2019. 9-10 December **2019**, Tokyo University, Tokyo, Japan. (Poster presentation)

4. Deekamwong, K., Pavel P.M., Ohtsu, H., Kawano, M. Multi-carboxylic acids as co-ligands to extend voids in the structure of cadmium and 4-KTPHAP coordination system. Annual Meeting 2018 and General Assembly of CrSJ. 2018. 10-11 December **2018**, Tokyo Institute of Technology, Tokyo, Japan. (Poster presentation)

1.8 References

1. Lock, G. G., Gerhard, *Chem. Ges. B* **1944,** *77*, 461-465.
2. Reid, D. H., *Tetrahedron* **1958,** *3* (3), 339-352.
3. Uchida, K.; Kubo, T., *J. Synth. Org. Chem Jpn.* **2016,** *74* (11), 1069-1077.
4. Reid, D. H., *Q. REV. CHEM. SOC.* **1965,** *19* (3), 274-302.
5. Zoellner, J. M.; Zoellner, R. W., *Journal of Molecular Structure: THEOCHEM* **2008,** *863* (1), 50-54.
6. Tian, Y.-H.; Kertesz, M., *Chem. Commun.* **2010,** *46* (24), 4282-4284.
7. Ahmed, J.; P, S.; Vijaykumar, G.; Jose, A.; Raj, M.; Mandal, S. K., *Chem. Sci.* **2017,** *8* (11), 7798-7806.
8. Liao, P.; Itkis, M. E.; Oakley, R. T.; Tham, F. S.; Haddon, R. C., *J. Am. Chem. Soc.* **2004,** *126* (43), 14297-14302.
9. Uchida, K.; Mou, Z.; Kertesz, M.; Kubo, T., *J. Am. Chem. Soc.* **2016,** *138* (13), 4665-4672.
10. Itkis, M. E.; Chi, X.; Cordes, A. W.; Haddon, R. C., *Science* **2002,** *296* (5572), 1443.
11. Koutentis, P. A.; Chen, Y.; Cao, Y.; Best, T. P.; Itkis, M. E.; Beer, L.; Oakley, R. T.; Cordes, A. W.; Brock, C. P.; Haddon, R. C., *J. Am. Chem. Soc.* **2001,** *123* (17), 3864-3871.
12. Goto, K.; Kubo, T.; Yamamoto, K.; Nakasuji, K.; Sato, K.; Shiomi, D.; Takui, T.; Kubota, M.; Kobayashi, T.; Yakusi, K.; Ouyang, J., *J. Am. Chem. Soc.* **1999,** *121* (7), 1619-1620.
13. Liang, X.; Guo, Z.; Wei, H.; Liu, X.; Lv, H.; Xing, H., *Chem. Commun.* **2018,** *54* (92), 13002-13005.
14. Hicks, R. G., *Nat. Chem* **2011,** *3* (3), 189-191.
15. Morita, Y.; Suzuki, S.; Sato, K.; Takui, T., *Nat. Chem* **2011,** *3* (3), 197-204.
16. Morita, Y.; Suzuki, S.; Fukui, K.; Nakazawa, S.; Kitagawa, H.; Kishida, H.; Okamoto, H.; Naito, A.; Sekine, A.; Ohashi, Y.; Shiro, M.; Sasaki, K.; Shiomi, D.; Sato, K.; Takui, T.; Nakasuji, K., *Nat. Mater.* **2008,** *7* (1), 48-51.
17. Kubo, T.; Shimizu, A.; Sakamoto, M.; Uruichi, M.; Yakushi, K.; Nakano, M.; Shiomi, D.; Sato, K.; Takui, T.; Morita, Y.; Nakasuji, K., *Angew. Chem. Int. Ed.* **2005,** *44* (40), 6564-6568.
18. Nishida, S.; Morita, Y.; Fukui, K.; Sato, K.; Shiomi, D.; Takui, T.; Nakasuji, K., *Angew. Chem. Int. Ed.* **2005,** *44* (44), 7277-7280.
19. Chikamatsu, M.; Mikami, T.; Chisaka, J.; Yoshida, Y.; Azumi, R.; Yase, K.; Shimizu, A.; Kubo, T.; Morita, Y.; Nakasuji, K., *Appl. Phys. Lett.* **2007,** *91* (4), 043506.
20. Morita, Y.; Ohba, T.; Haneda, N.; Maki, S.; Kawai, J.; Hatanaka, K.; Sato, K.; Shiomi, D.; Takui, T.; Nakasuji, K., *J. Am. Chem. Soc.* **2000,** *122* (19), 4825-4826.
21. Morita, Y.; Aoki, T.; Fukui, K.; Nakazawa, S.; Tamaki, K.; Suzuki, S.; Fuyuhiro, A.; Yamamoto, K.; Sato, K.; Shiomi, D.; Naito, A.; Takui, T.; Nakasuji, K., *Angew. Chem. Int. Ed.* **2002,** *41* (10), 1793-1796.
22. Morita, Y.; Fukui, K.; Suzuki, S.; Aoki, T.; Nakazawa, S.; Tamaki, K.; Fuyuhiro, A.; Yamamoto, K.; Sato, K.; Shiomi, D.; Naito, A.; Takui, T.; Nakasuji, K., *Polyhedron* **2003,** *22* (14), 2199-2204.
23. Zheng, S.; Lan, J.; Khan, S. I.; Rubin, Y., *J. Am. Chem. Soc.* **2003,** *125* (19), 5786-5791.
24. Zheng, S.; Thompson, J. D.; Tontcheva, A.; Khan, S. I.; Rubin, Y., *Org. Lett.* **2005,** *7* (9), 1861-1863.

25. Suzuki, S.; Morita, Y.; Fukui, K.; Sato, K.; Shiomi, D.; Takui, T.; Nakasuji, K., *Inorg. Chem.* **2005,** *44* (23), 8197-8199.
26. Tomlin, C. D. S. The Synthesis and Properties of s-Hexaazaphenalene. Princton University, Chem. Abstr., 1965.
27. Suzuki, S.; Fukui, K.; Fuyuhiro, A.; Sato, K.; Takui, T.; Nakasuji, K.; Morita, Y., *Org. Lett.* **2010,** *12* (21), 5036-5039.
28. Yakiyama, Y.; Ueda, A.; Morita, Y.; Kawano, M., *Chem. Commun.* **2012,** *48* (86), 10651-10653.
29. Kojima, T.; Yamada, T.; Yakiyama, Y.; Ishikawa, E.; Morita, Y.; Ebihara, M.; Kawano, M., *CrystEngComm* **2014,** *16* (28), 6335-6344.
30. Yakiyama, Y.; Lee, G. R.; Kim, S. Y.; Matsushita, Y.; Morita, Y.; Park, M. J.; Kawano, M., *Chem. Commun.* **2015,** *51* (31), 6828-6831.
31. Lee, G. R.; Ohtsu, H.; Koo, J.; Yakiyama, Y.; Park, M. J.; Inoue, D.; Hashizume, D.; Kawano, M., *Chem. Commun.* **2016,** *52* (20), 3962-3965.
32. Nakanishi, K.; Ohtsu, H.; Fukuhara, G.; Kawano, M., *Chem. Eur. J.* **2019,** *25* (66), 15182-15188.
33. Primdahl, K. G.; Nolsøe, J. M. J.; Aursnes, M., *Org. Biomol. Chem.* **2020,** *18* (44), 9050-9059.
34. Mancini, I.; Sicurelli, A.; Guella, G.; Turk, T.; Maček, P.; Sepčić, K., *Org. Biomol. Chem.* **2004,** *2* (9), 1368-1375.
35. Temraz, T. A.; Houssen, W. E.; Jaspars, M.; Woolley, D. R.; Wease, K. N.; Davies, S. N.; Scott, R. H., *BMC Pharmacol* **2006,** *6* (1), 10.
36. Tucker, S. J.; McClelland, D.; Jaspars, M.; Sepčić, K.; MacEwan, D. J.; Scott, R. H., *Biochimica et Biophysica Acta (BBA) - Biomembranes* **2003,** *1614* (2), 171-181.
37. Ilies, M. A.; Seitz, W. A.; Johnson, B. H.; Ezell, E. L.; Miller, A. L.; Thompson, E. B.; Balaban, A. T., *J. Med. Chem.* **2006,** *49* (13), 3872-3887.
38. Ilies, M. A.; Seitz, W. A.; Ghiviriga, I.; Johnson, B. H.; Miller, A.; Thompson, E. B.; Balaban, A. T., *J. Med. Chem.* **2004,** *47* (15), 3744-3754.
39. Rössler, S. L.; Jelier, B. J.; Magnier, E.; Dagousset, G.; Carreira, E. M.; Togni, A., *Angew. Chem. Int. Ed.* **2020,** *59* (24), 9264-9280.
40. Ford, L.; Atefi, F.; Singer, R. D.; Scammells, P. J., *Eur. J. Org. Chem.* **2011,** *2011* (5), 942-950.
41. Snelders, D. J. M.; Dyson, P. J., *Org. Lett.* **2011,** *13* (15), 4048-4051.
42. Ohkubo, K.; Kobayashi, T.; Fukuzumi, S., *Angew. Chem. Int. Ed.* **2011,** *50* (37), 8652-8655.
43. Tan, F.-F.; He, X.-Y.; Tian, W.-F.; Li, Y., *Nat. Commun.* **2020,** *11* (1), 6126.
44. Gini, A.; Uygur, M.; Rigotti, T.; Alemán, J.; García Mancheño, O., *Chem. Eur. J.* **2018,** *24* (48), 12509-12514.
45. Wang, K.; Guo, D.-S.; Wang, X.; Liu, Y., *ACS Nano* **2011,** *5* (4), 2880-2894.
46. Xing, L.-B.; Yu, S.; Wang, X.-J.; Wang, G.-X.; Chen, B.; Zhang, L.-P.; Tung, C.-H.; Wu, L.-Z., *Chem. Commun.* **2012,** *48* (88), 10886-10888.
47. Li, F.; Huang, Z.-j.; Zhou, Q.-h.; Pan, M.-y.; Tang, Q.; Gong, C.-b., *J. Mater.Chem. C* **2020,** *8* (29), 10031-10038.
48. Samanta, S. K.; Bhattacharya, S., *J. Mater. Chem.* **2012,** *22* (48), 25277-25287.
49. Wang, G.; Fu, X.; He, L.; Miao, Q.; Peng, G., *Chem. Phys. Lett.* **2014,** *614*, 243-250.

50. Zhang, G.; Zhang, X.; Kong, L.; Wang, S.; Tian, Y.; Tao, X.; Yang, J., *Sci. Rep.* **2016,** *6* (1), 37609.
51. Lim, C.; Kim, S.-H.; Yoh, S.-D.; Fujio, M.; Tsuno, Y., *Tetrahedron Lett.* **1997,** *38* (18), 3243-3246.
52. Castejon, H.; Wiberg, K. B., *J. Am. Chem. Soc.* **1999,** *121* (10), 2139-2146.
53. Ikeyama, S.; Amao, Y., *Photochem. Photobiol. Sci.* **2018,** *17* (1), 60-68.
54. Liu, Y.; Li, Y.; Zuo, P.; Chen, Q.; Tang, G.; Sun, P.; Yang, Z.; Xu, T., *ChemSusChem* **2020,** *13* (9), 2245-2249.
55. Zincke Reaction. In *Comprehensive Organic Name Reactions and Reagents*, pp 3172-3177.
56. Kost, A. N.; Gromov, S. P.; Sagitullin, R. S., *Tetrahedron* **1981,** *37* (20), 3423-3454.
57. Sowmiah, S.; Esperança, J. M. S. S.; Rebelo, L. P. N.; Afonso, C. A. M., *Org. Chem. Front.* **2018,** *5* (3), 453-493.
58. Chen, G.; Huang, X.; Zhang, Y.; Sun, M.; Shen, J.; Huang, R.; Tong, M.; Long, Z.; Wang, X., *Chem. Commun.* **2018,** *54* (86), 12174-12177.
59. Alesanco, Y.; Viñuales, A.; Cabañero, G.; Rodriguez, J.; Tena-Zaera, R., *ACS Appl. Mater. Interfaces* **2016,** *8* (43), 29619-29627.
60. Cheng, C.; Cheng, T.; Xiao, H.; Krzyaniak, M. D.; Wang, Y.; McGonigal, P. R.; Frasconi, M.; Barnes, J. C.; Fahrenbach, A. C.; Wasielewski, M. R.; Goddard, W. A.; Stoddart, J. F., *J. Am. Chem. Soc.* **2016,** *138* (26), 8288-8300.
61. Kahlfuss, C.; Denis-Quanquin, S.; Calin, N.; Dumont, E.; Garavelli, M.; Royal, G.; Cobo, S.; Saint-Aman, E.; Bucher, C., *J. Am. Chem. Soc.* **2016,** *138* (46), 15234-15242.
62. Natali, M.; Luisa, A.; Iengo, E.; Scandola, F., *Chem. Commun.* **2014,** *50* (15), 1842-1844.
63. Hirakawa, K.; Takai, S.; Horiuchi, H.; Okazaki, S., *ACS Omega* **2020,** *5* (42), 27702-27708.
64. Prabphal, J.; Vilaivan, T.; Praneenararat, T., *ChemistrySelect* **2018,** *3* (3), 894-899.
65. Matson, B. D.; Carver, C. T.; Von Ruden, A.; Yang, J. Y.; Raugei, S.; Mayer, J. M., *Chem. Commun.* **2012,** *48* (90), 11100-11102.
66. Ramesh, J.; Sujatha, S.; Arunkumar, C., *RSC Adv.* **2016,** *6* (68), 63271-63285.
67. Bar, G.; Larina, N.; Grinis, L.; Lokshin, V.; Gvishi, R.; Kiryuschev, I.; Zaban, A.; Khodorkovsky, V., *Sol. Energy Mater. Sol. Cells* **2012,** *99*, 123-128.
68. Aloïse, S.; Pawlowska, Z.; Poizat, O.; Buntinx, G.; Perrier, A.; Maurel, F.; Ohkawa, K.; Kimoto, A.; Abe, J., *PCCP* **2014,** *16* (4), 1460-1468.
69. Yan, N.; Song, J.; Wang, F.; Kan, L.; Song, J.; Wang, W.; Ma, W.; Zhang, W.; He, G., *Chin. Chem. Lett.* **2019,** *30* (11), 1984-1988.
70. Luo, J.; Hu, B.; Debruler, C.; Liu, T. L., *Angew. Chem. Int. Ed.* **2018,** *57* (1), 231-235.
71. Yamaguchi, K.; Murai, T.; Tsuchiya, Y.; Miwa, Y.; Kutsumizu, S.; Sasamori, T.; Tokitoh, N., *RSC Adv.* **2017,** *7* (29), 18132-18135.
72. Li, Z.-X.; Xu, C.-H.; Sun, W.; Bai, Y.-C.; Zhang, C.; Fang, C.-J.; Yan, C.-H., *New J. Chem.* **2009,** *33* (4), 853-859.
73. Hagiwara, S.; Ishida, Y.; Masui, D.; Shimada, T.; Takagi, S., *Tetrahedron Lett.* **2012,** *53* (43), 5800-5802.
74. Abeywickrama, C. S.; Wijesinghe, K. J.; Plescia, C. B.; Fisher, L. S.; Goodson Iii, T.; Stahelin, R. V.; Pang, Y., *Photochem. Photobiol. Sci.* **2020,** *19* (9), 1152-1159.

75. Niko, Y.; Moritomo, H.; Sugihara, H.; Suzuki, Y.; Kawamata, J.; Konishi, G.-i., *J. Mater.Chem. B* **2015,** *3* (2), 184-190.
76. Ma, L.; Xiao, S.; Wu, N.; Zhao, S.; Xiao, D., *Dyes Pigm.* **2019,** *168*, 327-333.
77. Danjo, H.; Masuda, Y.; Kidena, Y.; Kawahata, M.; Ohara, K.; Yamaguchi, K., *Org. Biomol. Chem.* **2020,** *18* (19), 3717-3723.
78. Li, F.; Liang, Z.; Liu, J.; Sun, J.; Hu, X.; Zhao, M.; Liu, J.; Bai, R.; Kim, D.; Sun, X.; Hyeon, T.; Ling, D., *Nano Lett.* **2019,** *19* (7), 4213-4220.
79. Bureš, F.; Cvejn, D.; Melánová, K.; Beneš, L.; Svoboda, J.; Zima, V.; Pytela, O.; Mikysek, T.; Růžičková, Z.; Kityk, I. V.; Wojciechowski, A.; AlZayed, N., *J. Mater.Chem. C* **2016,** *4* (3), 468-478.
80. Melánová, K.; Cvejn, D.; Bureš, F.; Zima, V.; Svoboda, J.; Beneš, L.; Mikysek, T.; Pytela, O.; Knotek, P., *Dalton. Trans.* **2014,** *43* (27), 10462-10470.
81. Keskin, S.; van Heest, T. M.; Sholl, D. S., *ChemSusChem* **2010,** *3* (8), 879-891.
82. Li, J.-R.; Sculley, J.; Zhou, H.-C., *Chem. Rev.* **2012,** *112* (2), 869-932.
83. Higuchi, M.; Tanaka, D.; Horike, S.; Sakamoto, H.; Nakamura, K.; Takashima, Y.; Hijikata, Y.; Yanai, N.; Kim, J.; Kato, K.; Kubota, Y.; Takata, M.; Kitagawa, S., *J. Am. Chem. Soc.* **2009,** *131* (30), 10336-10337.
84. Yuan, Y.; Sun, F.; Li, L.; Cui, P.; Zhu, G., *Nat. Commun.* **2014,** *5* (1), 4260.
85. Seo, S.; Yoon, Y.; Lee, J.; Park, Y.; Lee, H., *ACS Nano* **2013,** *7* (4), 3607-3615.
86. Kim, J.; Ohtsu, H.; Den, T.; Deekamwong, K.; Muneta, I.; Kawano, M., *Chem. Sci.* **2019,** *10* (47), 10888-10893.
87. Kim, J.; Koo, J. Y.; Lee, Y. H.; Kojima, T.; Yakiyama, Y.; Ohtsu, H.; Oh, J. H.; Kawano, M., *Inorg. Chem.* **2017,** *56* (15), 8735-8738.
88. Moon, H. C.; Lodge, T. P.; Frisbie, C. D., *Chem. Mater.* **2015,** *27* (4), 1420-1425.
89. Li, M.; Wei, Y.; Zheng, J.; Zhu, D.; Xu, C., *Org. Electron.* **2014,** *15* (2), 428-434.
90. Wei, M.; Gao, Y.; Li, X.; Serpe, M. J., *Polym. Chem.* **2017,** *8* (1), 127-143.
91. Aristov, N.; Habekost, A., *World J. Chem. Educ.* **2015,** *3* (4), 82-86.
92. Kim, S.-h.; Shim, N.; Lee, H.; Moon, B., *J. Mater. Chem.* **2012,** *22* (27), 13558-13563.
93. Kim, M.; Kim, Y. M.; Moon, H. C., *RSC Adv.* **2020,** *10* (1), 394-401.
94. Palenzuela, J.; Viñuales, A.; Odriozola, I.; Cabañero, G.; Grande, H. J.; Ruiz, V., *ACS Appl. Mater. Interfaces* **2014,** *6* (16), 14562-14567.
95. Woodward, A. N.; Kolesar, J. M.; Hall, S. R.; Saleh, N.-A.; Jones, D. S.; Walter, M. G., *J. Am. Chem. Soc.* **2017,** *139* (25), 8467-8473.
96. Zhao, X.; Gu, Y.; Li, J.; Ding, H.; Shan, Y., *Catal. Commun.* **2008,** *9* (13), 2179-2182.
97. Ni, B.; Zhang, Q.; Headley, A. D., *Tetrahedron Lett.* **2008,** *49* (7), 1249-1252.
98. Li, X.; Eli, W., *J. Mol. Catal. A: Chem.* **2008,** *279* (2), 159-164.
99. Rueping, M.; Nikolaienko, P.; Lebedev, Y.; Adams, A., *Green Chem.* **2017,** *19* (11), 2571-2575.
100. Cumine, F.; Zhou, S.; Tuttle, T.; Murphy, J. A., *Org. Biomol. Chem.* **2017,** *15* (15), 3324-3336.
101. Li, M.; Berritt, S.; Matuszewski, L.; Deng, G.; Pascual-Escudero, A.; Panetti, G. B.; Poznik, M.; Yang, X.; Chruma, J. J.; Walsh, P. J., *J. Am. Chem. Soc.* **2017,** *139* (45), 16327-16333.

102. Munz, D.; Chu, J.; Melaimi, M.; Bertrand, G., *Angew. Chem. Int. Ed.* **2016,** *55* (41), 12886-12890.
103. Murphy, J. A.; Khan, T. A.; Zhou, S.-z.; Thomson, D. W.; Mahesh, M., *Angew. Chem. Int. Ed.* **2005,** *44* (9), 1356-1360.
104. Cumine, F.; Palumbo, F.; Murphy, J. A., *Tetrahedron* **2018,** *74* (38), 5539-5545.
105. Tintori, G.; Nabokoff, P.; Buhaibeh, R.; Bergé-Lefranc, D.; Redon, S.; Broggi, J.; Vanelle, P., *Angew. Chem. Int. Ed.* **2018,** *57* (12), 3148-3153.
106. Basch, C. H.; Liao, J.; Xu, J.; Piane, J. J.; Watson, M. P., *J. Am. Chem. Soc.* **2017,** *139* (15), 5313-5316.
107. Klauck, F. J. R.; James, M. J.; Glorius, F., *Angew. Chem. Int. Ed.* **2017,** *56* (40), 12336-12339.
108. Zhu, Z.-F.; Zhang, M.-M.; Liu, F., *Org. Biomol. Chem.* **2019,** *17* (6), 1531-1534.
109. Zhang, M.-M.; Liu, F., *Org. Chem. Front.* **2018,** *5* (23), 3443-3446.
110. Yue, H.; Zhu, C.; Shen, L.; Geng, Q.; Hock, K. J.; Yuan, T.; Cavallo, L.; Rueping, M., *Chem. Sci.* **2019,** *10* (16), 4430-4435.
111. Klauck, F. J. R.; Yoon, H.; James, M. J.; Lautens, M.; Glorius, F., *ACS Catal.* **2019,** *9* (1), 236-241.
112. Hu, J.; Wang, G.; Li, S.; Shi, Z., *Angew. Chem. Int. Ed.* **2018,** *57* (46), 15227-15231.
113. Adam, W.; Kazakov, D. V.; Kazakov, V. P., *Chem. Rev.* **2005,** *105* (9), 3371-3387.
114. Noimark, S.; Salvadori, E.; Gómez-Bombarelli, R.; MacRobert, A. J.; Parkin, I. P.; Kay, C. W. M., *Physical Chemistry Chemical Physics* **2016,** *18* (40), 28101-28109.
115. Yu, G.; Wang, Y.; Cao, H.; Zhao, H.; Xie, Y., *Environ. Sci. Technol.* **2020,** *54* (10), 5931-5946.
116. Dan-Hardi, M.; Serre, C.; Frot, T.; Rozes, L.; Maurin, G.; Sanchez, C.; Férey, G., *J. Am. Chem. Soc.* **2009,** *131* (31), 10857-10859.
117. Sun, D.; Ye, L.; Li, Z., *Appl. Catal. B* **2015,** *164*, 428-432.
118. Long, J.; Wang, S.; Ding, Z.; Wang, S.; Zhou, Y.; Huang, L.; Wang, X., *Chem. Commun.* **2012,** *48* (95), 11656-11658.
119. Pitre, S. P.; McTiernan, C. D.; Ismaili, H.; Scaiano, J. C., *J. Am. Chem. Soc.* **2013,** *135* (36), 13286-13289.
120. Zou, Y.-Q.; Chen, J.-R.; Liu, X.-P.; Lu, L.-Q.; Davis, R. L.; Jørgensen, K. A.; Xiao, W.-J., *Angew. Chem. Int. Ed.* **2012,** *51* (3), 784-788.
121. Yu, D.; To, W.-P.; Tong, G. S. M.; Wu, L.-L.; Chan, K.-T.; Du, L.; Phillips, D. L.; Liu, Y.; Che, C.-M., *Chem. Sci.* **2020,** *11* (25), 6370-6382.
122. De Bonfils, P.; Verron, E.; Sandoval-Altamirano, C.; Jaque, P.; Moreau, X.; Gunther, G.; Nun, P.; Coeffard, V., *J. Org. Chem.* **2020,** *85* (16), 10603-10616.
123. Jung, M.; Ham, J.; Song, J., *Org. Lett.* **2002,** *4* (16), 2763-2765.
124. Sawwan, N.; Greer, A., *Chem. Rev.* **2007,** *107* (7), 3247-3285.
125. Sagadevan, A.; Hwang, K. C.; Su, M.-D., *Nat. Commun.* **2017,** *8* (1), 1812.
126. Zhao, J.; Wu, W.; Sun, J.; Guo, S., *Chem. Soc. Rev.* **2013,** *42* (12), 5323-5351.
127. Li, J.; Chen, T., *Coord. Chem. Rev.* **2020,** *418*, 213355.
128. Zhou, X.; Liang, H.; Jiang, P.; Zhang, K. Y.; Liu, S.; Yang, T.; Zhao, Q.; Yang, L.; Lv, W.; Yu, Q.; Huang, W., *Adv. Sci.* **2016,** *3* (2), 1500155.

129. Li, L.-P.; Peng, H.-L.; Wei, L.-Q.; Ye, B.-H., *Inorg. Chem.* **2019,** *58* (1), 785-793.
130. Karges, J.; Kuang, S.; Maschietto, F.; Blacque, O.; Ciofini, I.; Chao, H.; Gasser, G., *Nat. Commun.* **2020,** *11* (1), 3262.
131. Turksoy, A.; Yildiz, D.; Akkaya, E. U., *Coord. Chem. Rev.* **2019,** *379*, 47-64.
132. Zhao, J.; Chen, K.; Hou, Y.; Che, Y.; Liu, L.; Jia, D., *Org. Biomol. Chem.* **2018,** *16* (20), 3692-3701.
133. Zhu, S.; Yao, S.; Wu, F.; Jiang, L.; Wong, K.-L.; Zhou, J.; Wang, K., *Org. Biomol. Chem.* **2017,** *15* (27), 5764-5771.
134. Uchoa, A. F.; de Oliveira, K. T.; Baptista, M. S.; Bortoluzzi, A. J.; Iamamoto, Y.; Serra, O. A., *J. Org. Chem.* **2011,** *76* (21), 8824-8832.
135. Ye, Y.; Bruning, H.; Yntema, D.; Mayer, M.; Rijnaarts, H., *Chem. Eng. J.* **2017,** *316*, 872-881.
136. Guo, S.; Wu, W.; Guo, H.; Zhao, J., *J. Org. Chem.* **2012,** *77* (8), 3933-3943.
137. Semeraro, P.; Syrgiannis, Z.; Bettini, S.; Giancane, G.; Guerra, F.; Fraix, A.; Bucci, C.; Sortino, S.; Prato, M.; Valli, L., *J. Colloid Interface Sci.* **2019,** *553*, 390-401.
138. Lei, J.; Akitoshi, T.; Katou, S.; Murakami, Y.; Yin, J.; Jiang, X., *Macromol. Chem. Phys.* **2019,** *220* (15), 1900152.
139. Wang, R.; Geng, Y.; Zhang, L.; Wu, W.; Fan, W.; Li, Z.; Wang, L.; Zhan, L.; Wu, X.; Wu, M., *Chin. J. Chem* . **2015,** *33* (11), 1251-1258.
140. Lorente, C.; Arzoumanian, E.; Castaño, C.; Oliveros, E.; Thomas, A. H., *RSC Adv.* **2014,** *4* (21), 10718-10727.
141. Nguyen, V.-N.; Yan, Y.; Zhao, J.; Yoon, J., *Acc. Chem. Res.* **2020**.
142. Ibhadon, A. O.; Fitzpatrick, P., *Catalysts* **2013,** *3* (1).
143. Chen, Y.; Hoang, T.; Ma, S., *Inorg. Chem.* **2012,** *51* (23), 12600-12602.
144. Xie, M.-H.; Yang, X.-L.; Wu, C.-D., *Chem. Commun.* **2011,** *47* (19), 5521-5523.
145. Zou, C.; Zhang, T.; Xie, M.-H.; Yan, L.; Kong, G.-Q.; Yang, X.-L.; Ma, A.; Wu, C.-D., *Inorg. Chem.* **2013,** *52* (7), 3620-3626.
146. Guo, Z.; Yan, D.; Wang, H.; Tesfagaber, D.; Li, X.; Chen, Y.; Huang, W.; Chen, B., *Inorg. Chem.* **2015,** *54* (1), 200-204.
147. Huh, S.; Kim, S.-J.; Kim, Y., *CrystEngComm* **2016,** *18* (3), 345-368.
148. Zhao, F.-J.; Zhang, G.; Ju, Z.; Tan, Y.-X.; Yuan, D., *Inorg. Chem.* **2020,** *59* (5), 3297-3303.
149. Li, X.; Chen, D.; Liu, Y.; Yu, Z.; Xia, Q.; Xing, H.; Sun, W., *CrystEngComm* **2016,** *18* (20), 3696-3702.
150. Guo, Z.; Zhao, H.; Liu, X.; Liang, X.; Wei, H.; Mei, Y.; Xing, H., *Appl. Organomet. Chem.* **2020,** *34* (4), e5487.
151. Zhang, Y.; Pang, J.; Li, J.; Yang, X.; Feng, M.; Cai, P.; Zhou, H.-C., *Chem. Sci.* **2019,** *10* (36), 8455-8460.
152. Liu, Y.; Buru, C. T.; Howarth, A. J.; Mahle, J. J.; Buchanan, J. H.; DeCoste, J. B.; Hupp, J. T.; Farha, O. K., *J. Mater. Chem. A* **2016,** *4* (36), 13809-13813.
153. Yamaguchi, M.; Tomizawa, M.; Takagaki, K.; Shimo, M.; Masui, D.; Yamagishi, T., *Catal. Today* **2006,** *117* (1), 206-209.
154. Wada, K.; Yoshida, K.; Watanabe, Y., *J. Chem. Soc., Faraday Trans.* **1995,** *91* (11), 1647-1654.
155. Yoshizawa, M.; Miyagi, S.; Kawano, M.; Ishiguro, K.; Fujita, M., *J. Am. Chem. Soc.* **2004,** *126* (30), 9172-9173.

156. Ohkubo, K.; Hirose, K.; Fukuzumi, S., *Chem. Asian. J.* **2016,** *11* (16), 2255-2259.
157. Zhao, X.; Zhang, Y.; Wen, P.; Xu, G.; Ma, D.; Qiu, P., *Mol. Catal.* **2018,** *452*, 175-183.
158. Shi, W.; Cao, L.; Zhang, H.; Zhou, X.; An, B.; Lin, Z.; Dai, R.; Li, J.; Wang, C.; Lin, W., *Angew. Chem. Int. Ed.* **2017,** *56* (33), 9704-9709.

Chapter 2

Photoactive Hexaazaphenalene Ligand-based Network as a Reactive Oxygen Species Generator

Abstract

A novel photosensitizer, tris(4-pyridyl) hexaazaphenalene (TPHAP), exhibited both energy and charge transfer processes to oxygen molecules under UV irradiation resulting in the production of reactive oxygen species (ROSs). The existence of ROSs was further confirmed by selective photooxidation, addition of scavenger reagents and spectroscopic characterization. In addition, a porous coordination network, **PCN 1**, consisting of TPHAP, cadmium ions and fumarate as a co-ligand, was synthesized and used as a heterogeneous support for the photoactive TPHAP molecule capable of ROSs generation. **PCN 1** was further applied for photooxidation of various saturated hydrocarbons, including cyclohexane, cyclooctane and *n*-octane, displaying superior activities and stability compared to other porous coordination networks.

2.1 Introduction

Photo-induced formation of reactive oxygen species (ROSs) is widely employed in several industrially important chemical transformations.[1-6] The ROSs are typically generated *in situ* by introducing suitable photosensitizers (PSs) into the system to be able to utilize the light as a driving force for the reactions. These molecules can be readily excited by light irradiation and subsequently undergo energy or charge transfer to other species present in the reaction mixture. If the excited states of PS molecules interact with molecular oxygen, two types of ROSs are commonly created, singlet oxygen ($^1O_2$) via energy transfer and various radical species, such as superoxide anion ($O_2^{\bullet-}$) and hydroxyl radical ($^{\bullet}OH$) by a direct electron transfer.[7] Numerous families of PSs have been developed and utilized for photocatalytic applications in the past, including methylene blue, porphyrins, and phthalocyanines, among others.[8-12] The development of these compounds has primarily focused on optimizing their energy levels, extending the excited states lifetimes, and enhancing the energy and charge transfer characteristics. However, their photosensitizing ability is still primarily utilized in a homogeneous state during photocatalytic reactions, which present problems for product separation, as well as PS photostability and recycling. Therefore, there is a considerable interest in immobilizing these PSs into various solid support matrices to create corresponding heterogeneous photosensitizers while retaining the beneficial properties of their molecular constituents.

Among various classes of materials, porous coordination networks (PCNs) are particularly promising for this purpose. These crystalline compounds, comprised of organic linkers and metal ions, can readily incorporate the desired molecular species into their backbone structure. Furthermore, the presence of accessible pore could enable a facile diffusion of oxygen towards the photoactive sites, thus enhancing the ROSs generation. In general, the most common strategy for creating photoactive PCNs is to substitute suitable photosensitizer molecules with coordinating groups and employ them as linkers in the network synthesis. Several families of such networks utilizing different PSs have been reported, porphyrin (PCN-222, UNLPE-10,

PCN-134), perylenediimide (FJI-Y10), anthracene (NNU-32, NNU-37) and pyrene (PCN-822, NU-1000).[13-20] However, there is still considerable room for further development of novel photoactive ligands for the construction of PCNs.

Previously, a molecule, tris(4-pyridyl) hexaazaphenalene (TPHAP), was developed by Kawano, which exhibited beneficial photophysical properties, and at the same time could be used to construct coordination networks.[21, 22] This anionic specie contains a phenalene-type fused tricyclic core. Related phenalene-based systems were demonstrated to generate singlet oxygen upon light irradiation[23, 24]. Herein, my aim was to investigate the ROSs generation ability of the TPHAP system by using spectroscopic analysis and photoinduced degradation of various compounds. In addition, TPHAP was incorporated into a new cadmium-based porous coordination network (**PCN 1**) and investigated as a heterogeneous catalyst for photooxidation of challenging saturated hydrocarbon substrates. Recyclability experiments and stability tests confirmed that the network retained its structural integrity and TPHAP did not leach out into the reaction mixture, thus confirming the heterogeneous nature of the photosensitizer.

2.2 Results and Discussion

2.2.1 Photosensitizer Characterization

Photophysical properties of [TBA][TPHAP] were assessed from its absorption and emission spectra in acetonitrile solution. The UV-Vis spectra exhibited an absorption band at 335 nm (ε = 11114 $M^{-1}.cm^{-1}$), which closely matched the previously reported spectra of K[TPHAP]. This band was assigned to an intramolecular charge transfer (ICT) transition from the HAP core to the three peripheral pyridyl groups. In addition, TPHAP compounds were shown to display photoluminescence at room temperature with emission lifetime about 1.5 ns (Table 2-6 and 2-7). As shown in Figure 2-1, the emission spectrum features broad peaks with maxima at 414 and 430 nm under nitrogen atmosphere. The intensity of emission immediately decreased when air was introduced into the solution but stabilized after 10 min. This

quenching behavior indicated that TPHAP was acting as a photosensitizer and its excited state was able to transfer energy to oxygen molecules to generate reactive oxygen species (ROSs). Since the activation energy was related to the charge transfer from HAP to the terminal groups, the photophysical properties could be manipulated by modification or replacement of the pyridyl groups.

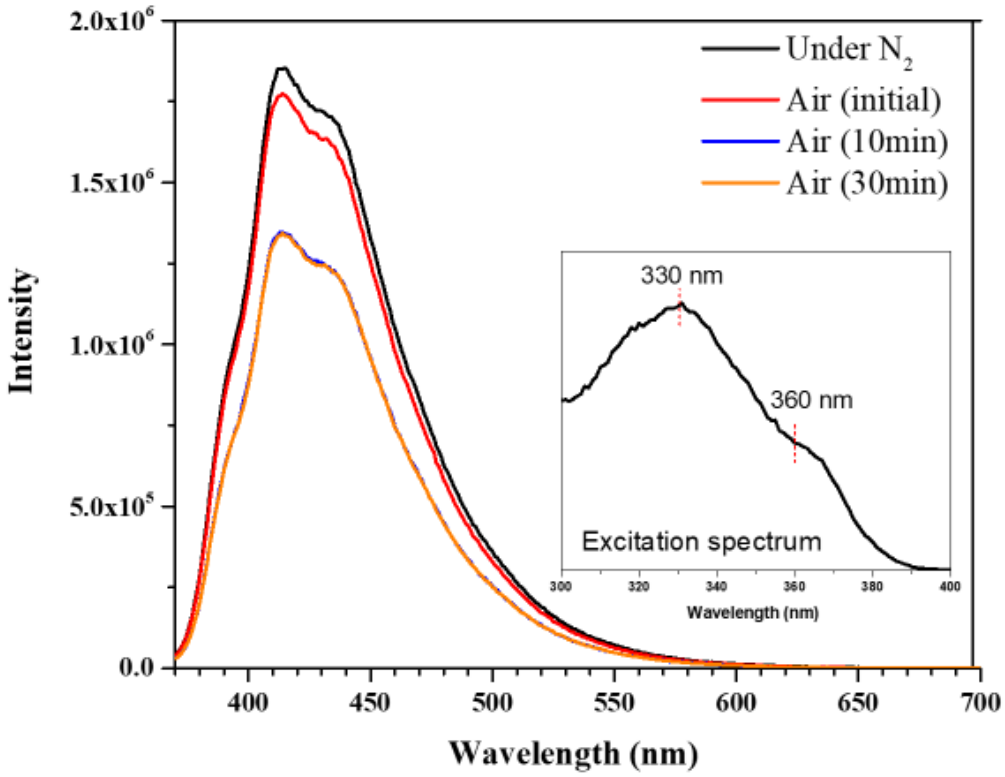

Figure 2-1 Emission spectra of [TBA][TPHAP] measured in acetonitrile (MeCN) under nitrogen and air conditions (λ_{ex} = 360 nm). Inset shows the excitation spectrum.

The possibility of singlet oxygen ($^1O_2$) formation via the energy transfer pathway was considered. The existence of $^1O_2$ was confirmed by photooxidation of 1,5-dihydroxynaphthalene (1,5-DHN), which is typically used as a selective trap.[25-27] The trapping reaction was performed in a homogeneous MeCN solution. The reaction progress was monitored by *ex situ* UV-Vis spectroscopy, where a decrease in the absorption of 1,5-DHN at 298 nm (ε = 7664 $M^{-1}.cm^{-1}$) and corresponding increase in the adsorption of juglone product

at 419 nm (ε = 3811 $M^{-1}.cm^{-1}$) were recorded. Additional control experiments with varying [TBA][TPHAP] loading, as well as the presence or absence of light were performed in order further elucidate the photoactivity of TPHAP. The 1,5-DHN conversion was negligible when either TPHAP or light source were absent, confirming that the process was chiefly driven by light excitation of the [TBA][TPHAP] as a photocatalyst. Consequently, when TPHAP was irradiated with light (365 nm) in the presence of 1,5-DHN, the UV-Vis absorption bands of the reaction mixture displayed a gradual change, indicating the formation of the juglone product, as shown in Figure 2-2.

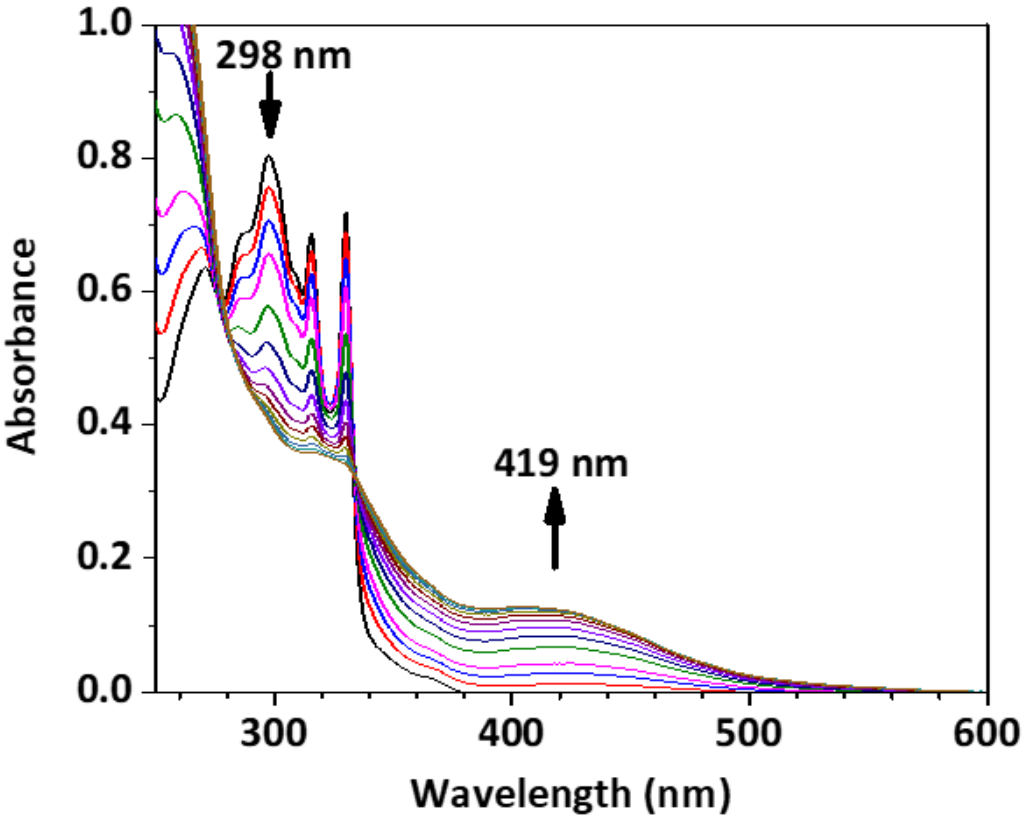

Figure 2-2 Time dependent absorption spectra of photooxidation of 1,5-DHN (1×10^{-4} M) using TPHAP as a photocatalyst.

The production rate increased at higher photocatalyst loadings (Figure 2-3a). The reaction rate (k_{obs}) and initial rate of 1,5-DHN consumption (v_i) were determined by fitting the time-

dependent spectroscopic data with the pseudo-first order reaction approximation, as described in equations 1 and 2.[28]

$$\ln (A_t / A_0) = -k_{obs} \times t \quad \text{Equation 1}$$

$$v_i = k_{obs} [DHN] \quad \text{Equation 2}$$

As shown in Figure 2-3b and Table 2-1, k_{obs} and v_i were calculated to be 11.3×10^{-2} min^{-1} and 1.13×10^{-5} $M.min^{-1}$, respectively, at 10 % photocatalyst loading. These rate constants increased with photocatalyst loading, providing further support for the ability of TPHAP to generate $^1O_2$. For example, several transition metal complexes could serve as efficient singlet oxygen generators due to the heavy metal induced triplet state excitation. Nevertheless, iridium, platinum, and ruthenium metal complexes at 10 % loading catalyzed 1,5-DHN oxidation in mixed solvent system of DCM/MeOH using xenon arc lamp (cut off filter > 390 nm) with the k_{obs} and v_i values only in the range of $0.26 - 3.59 \times 10^{-2}$. min^{-1} and $0.425 - 1.75 \times 10^{-5}$ $M.min^{-1}$, respectively.[25, 26, 28, 29]

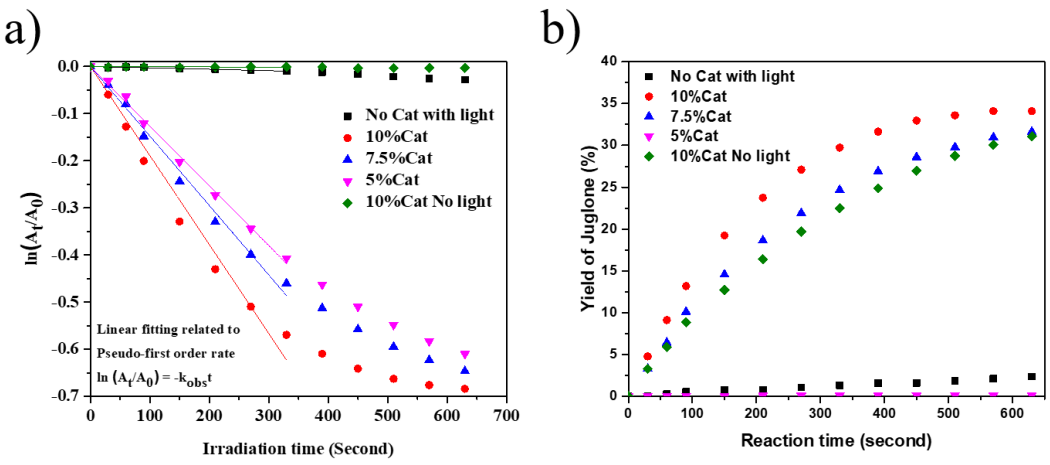

Figure 2-3 Plots of a) $\ln(A_t / A_0)$ and b) yield of juglone against irradiation time for photooxidation of 1,5-DHN using TPHAP as a photocatalyst

Table 2-1 Summary of pseudo-first order kinetics parameters for the photooxidation of 1,5-DHN under different conditions.

Condition	k_{obs} (10^{-2}. min^{-1})	v_i (10^{-5} $M.min^{-1}$)
No Cat with light	0.179	0.018
10% Cat	11.3	1.13
7.5% Cat	8.82	0.88
5% Cat	7.62	0.76
10% Cat No light	0.0279	0.0028

Another possible photoreaction mechanism involving charge transfer (electron or hydrogen) between the excited state of photosensitizer and molecular oxygen leading to other ROSs, such as superoxide radical anion ($O_2^{\bullet-}$) and hydroxyl radical was also considered. Photodecomposition studies of several known dyes were performed using the same experimental set up as that used for the 1,5-DHN photooxidation. As shown in Figure 2-4, the absorption bands of methylene blue (λ_{max} = 656 nm), crystal violet (λ_{max} = 588 nm) and indigo dye (λ_{max} = 596 nm) fully disappeared after light irradiation for 120, 120 and 10 mins, respectively.[30-32] It is important to note that the relatively short degradation time of indigo dye was due to its low solubility in acetonitrile and therefore low initial concentration. These results suggested that photoexcitation of TPHAP promoted the generation of oxygen radical species.

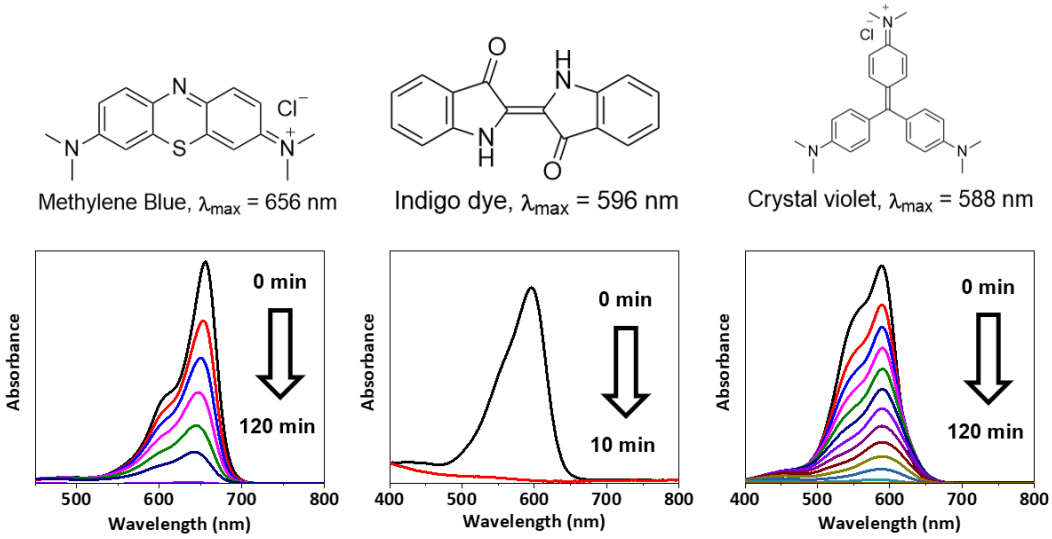

Figure 2-4 Time dependent absorption spectra of dyes measured during the degradation experiments using [TBA][TPHAP] as a photocatalyst. $[TPHAP]_{initial} = 1.4 \times 10^{-3}$ mM, $[Methylene\ blue]_{initial} = 2.7 \times 10^{-2}$ mM, $[Crystal\ violet]_{initial} = 2.7 \times 10^{-2}$ mM and $[Indigo\ dye]_{initial}$ = saturated solution.

Additional evidence for this process were obtained from the solid state ESR spectra collected at different irradiation time intervals (Figure 2-5). The results revealed that TPHAP displayed a radical signal (g = 2.0033) in the absence of oxygen (vacuum condition).[33] When air was introduced into the sample tube by opening the J-young ESR cap, ESR signal slowly decreased confirming the reactivity of the TPHAP radical towards atmospheric oxygen.

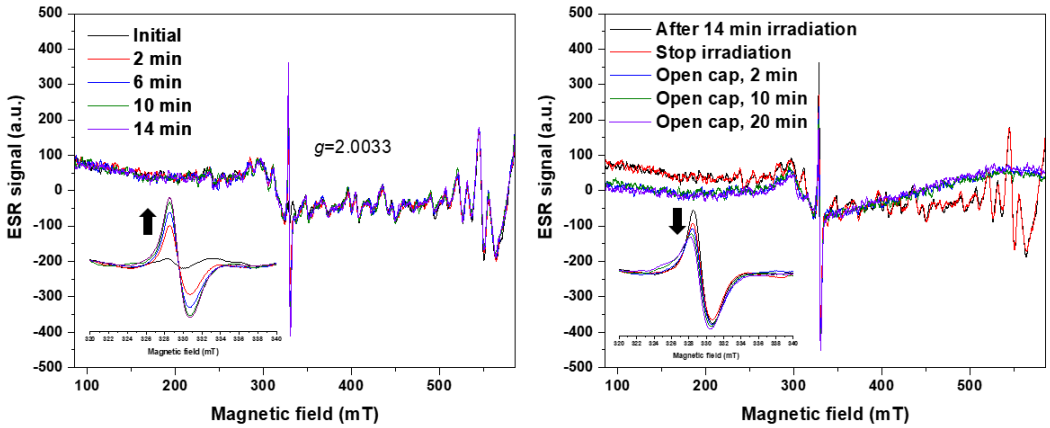

Figure 2-5 Solid state ESR spectra of TPHAP measured at -173 °C using a J-young ESR tube in the absence of oxygen while irradiating with UV light at different time intervals (0-14 min) (*left*) and the evolution of the ESR spectra after introduction of air by opening the cap (*right*).

Lastly, due to the ROSs generation ability of TPHAP, it was investigated as a photocatalyst for oxidation of various organic substrates, such as cyclohexane, 2-methyl-1-butene, isoprene, tetrahydrofuran, and furfural using *in situ* NMR techniques with reaction mixture swirling and UV irradiation. The preliminary results, shown in Table 2-2 and Figure 2-12, suggested that these substrates could be oxidized in the presence of TPHAP molecule, with cyclohexane oxidation being especially remarkable because of its relative inertness. Encouraged by these promising results, the photocatalytic activity of TPHAP towards alkane oxidation was investigated in greater detail for expanded series of substrates.

Table 2-2 Screening of substrates for photooxidation using in situ NMR techniques.

Entry	Substrate	Conversion (%) at (t) h
1	2-methyl-1-butene 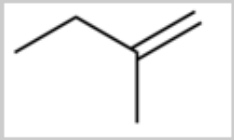	13.5 at 3h
2	Isoprene 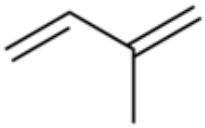	71.5 at 3h
3	Furfural 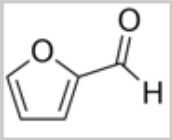	100 at 3h
4	THF 	60 at 3h
5	Cyclohexane 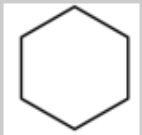	100 at 18 h

However, when a TPHAP solution in MeCN was irradiated with UV light, the observed absorption band changes were consistent with degradation of TPHAP (Figure 2-6). This behavior can be used to explain the slowing down of the reaction rates in the reaction kinetic plot (Figure 2-3a).

One strategy to overcome this limitation is to incorporate TPHAP into a coordination network scaffold as a connecting linker. This type of immobilization should minimize the number possible degradation pathways and therefore enhance its useful lifetime.

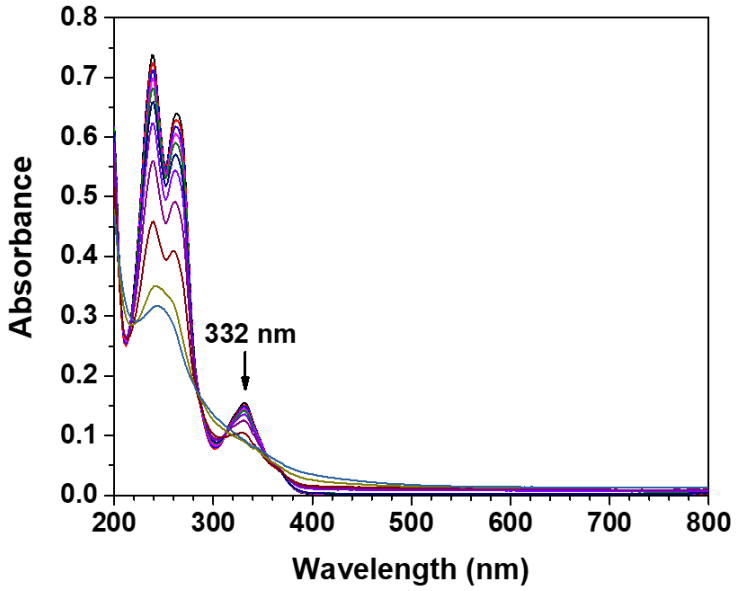

Figure 2-6 Time dependent absorption spectra change of [TBA][TPHAP] solution in MeCN during photoirradiation measured at 0, 10, 20, 30, 40, 50, 60, 80, 100, 120, and 180 min; [TPHAP] = 1.4×10^{-5} M

2.2.2 Synthesis and Characterization of PCN 1

There are several reports of TPHAP-based PCN synthesis and characterization. However, due to the labile nature of the pyridine-metal coordination bond, these structures were not suitable for further photocatalytic testing since they were susceptible structural rearrangements and collapse (Figure 2-14). Therefore, the use of carboxylic acids as co-ligands for the network formation was deemed to be the most suitable strategy to improve the structural stability.[34] Several commonly available multidentate carboxylic acids were used as co-ligand resulting to several porous coordination networks as shown in Table 2-8 and 2-9, Because of C_3 symmetry and multi-interaction of TPHAP anion combined with additional coordination mode from carboxylic acids, it was hardly to obtain a pure phase or purify from the synthesized mixture. However, the resultant network, denoted as **PCN 1**, was composed of fumarate, cadmium cations and anionic TPHAP ligands. It exhibited good structural stability and could be synthesized with a high product yield and phase purity.

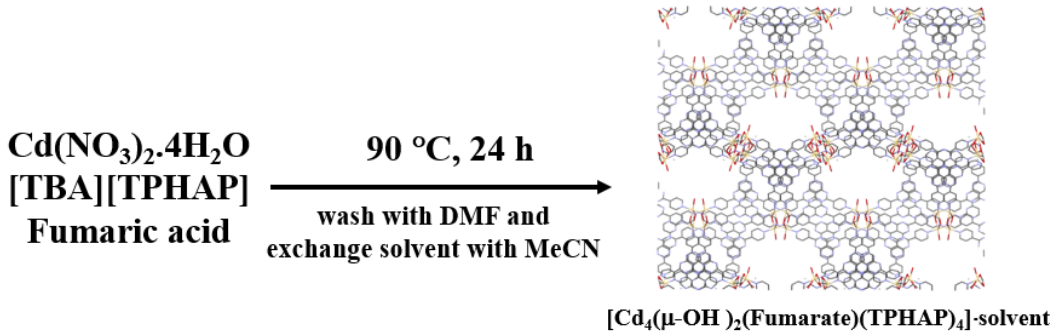

Scheme 2-1 Synthesis of **PCN 1**.

Crystals of **PCN 1** were obtained by solvothermal method where [TBA][TPHAP], fumaric acid and cadmium nitrate were reacted in a mixed solvent system of DMF/MeCN (1:1) at 90 °C for 2 days, as shown in Scheme 2-1. Single crystal X-ray analysis revealed that they had a molecular formula of $[Cd_4(\mu\text{-}OH)_2(Fumarate)(TPHAP)_4]$ with the structure consisting of a three-dimensional coordination network crystallized in a monoclinic $P2_1/c$ space group, as shown in Figure 2-7a. It contained two types of dinuclear Cd(II) clusters. One had metal centers bridged by two μ-OH groups and connected into an extended structure by four TPHAP and one fumarate ligands. Each Cd(II) center in the first hydroxy-bridged dinuclear cluster adopted a distorted trigonal-bipyramidal geometry with a Cd1 – Cd2 separation of 3.958 Å.[35, 36] Two pyridyl groups from the two neighboring TPHAP ligands (TPHAP1 and TPHAP2 dimer) were coordinated perpendicular to the Cd-hydroxide dimer plane, whereas the third pyridyl group from another ligand (TPHAP3) coordinated parallel (Figure 2-7b). The second dimeric Cd(II) cluster was doubly bridged by two fumarate co-ligands to another identical cluster where carboxylate groups from each fumarate adopted chelating and μ-*O,O*-η-*O,O´* coordination modes along the c-axis. The Cd3 – Cd4 separation was 3.864 Å.[37, 38] The pyridyl groups from two distinct TPHAP ligands (TPHAP3 and TPHAP4) coordinated to Cd(II) ions along the b-axis (Figure 2-7c).

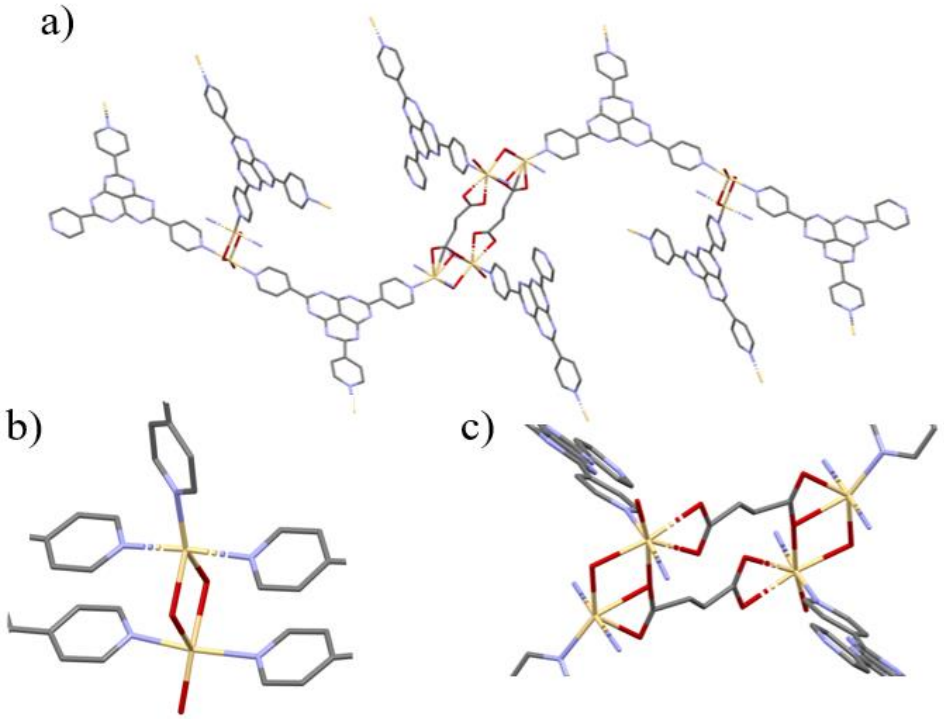

Figure 2-7 a) Crystal structure of **PCN 1**. b) Hydroxy-bridged dinuclear cluster where each Cd(II) center adopted a distorted trigonal-bipyramidal geometry. c) Dimeric Cd(II) clusters bridged by two fumarate co-ligands. All hydrogen atoms were omitted for clarity. C – grey, N – blue, O – red. Cd – yellow.

Overall, the network structure exhibited a 3D porosity with the largest pore window of 15 × 10 Å along the c-axis. The void volume of the structure was calculated to be 47 % (contact surface) using Mercury software (Figure 2-8).

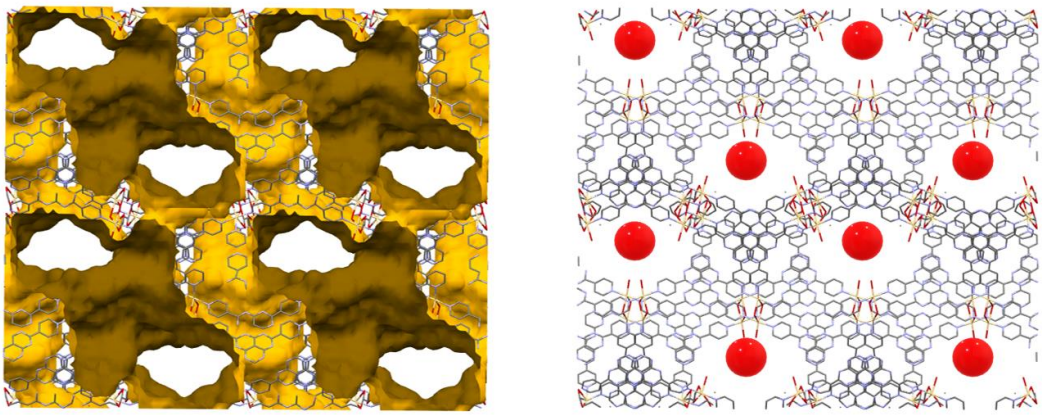

Figure 2-8 Packing structure of **PCN 1** displaying the available pore space.

2.2.3 Photooxidation of Saturated Hydrocarbons

The promising ability of TPHAP to generate various ROSs prompted us to investigate its photooxidation activity towards various C6 and C8 hydrocarbon substrates. These kinds of molecules are considered to be relatively unreactive and therefore the development of catalytic systems that are able to convert them to other useful chemicals is highly desirable. The photocatalytic reaction activities were evaluated from GC-FID and GC-MS measurements as described in scheme 2-2. First, the photooxidation was performed on cyclohexane as shown in Table 2-3. All catalytic reaction showed relatively low product yield compared to the initial cyclohexane and its consumption. Based on the current analysis of mixture product, there are still unidentified products which could be the mixture of polymerized compounds related to the resultant yellow liquid. Therefore, three detected major products consisted of cyclohexanone, cyclohexanol and cyclohexyl methyl ketone were used to consider the catalytic activity in this work. Cyclohexanone and cyclohexanol are produced via oxidation process from reactive oxygen species. Meanwhile, cyclohexyl methyl ketone is produced via cross-coupling reaction between cyclohexyl radical and acetonitrile radical and followed by oxidation reaction.[39] First, the cyclohexane consumption was 69 % when using heterogeneous **PCN 1** as a photocatalyst. In comparison, when the activity of TPHAP itself was tested in a homogeneous reaction mixture, the cyclohexane consumption was 3.4 %. However, when the results were normalized by the mole of TPHAP and reaction time, to get TOF, the sensitizing performance of TPHAP and its ability to generate ROSs were largely retained after incorporation into the network structure. Moreover, porosity of **PCN 1** affected to the product distribution defined by product selectivity where CMK was the major product unlike TPHAP itself.

Table 2-3 Photocatalytic oxidation of cyclohexane.[a]

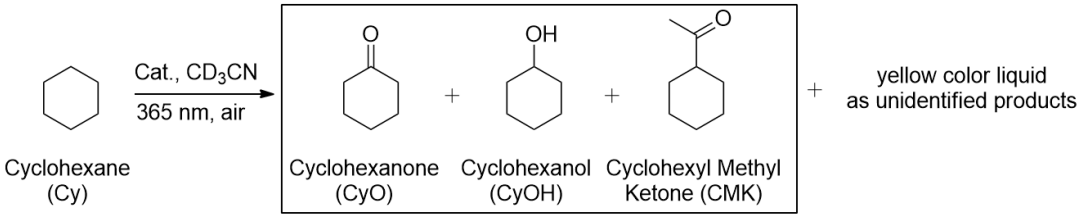

	Homogeneous TPHAP anion	Heterogeneous PCN 1
mole of TPHAP (μmol)	7.76	9.08
Reaction time	4	48
Substrate consumption (%, mmol)	3.4	69
Conversion (%)	0.16	2.04
Total product (μmol)	2.4	30.5
- Cyclohexanone selectivity (%)	31.4	11.4
- Cyclohexanol selectivity (%)	33.6	14.5
- Cyclohexyl Methyl Ketone selectivity (%)	35	74.1
TON (mol products/mol TPHAP)	0.31	3.36
TOF (h^{-1})	0.08	0.07

[a]General reaction conditions: 0.5 M of cyclohexane in 3 mL CD_3CN, sensitizer, air balloon connected to the reaction vessel, monochromatic LED light (365 nm).

From Table 2-4, to confirm that the **PCN 1** was indeed acting as a heterogeneous catalyst, a leaching test was performed by filtering the network powder after 12 h of reaction. Continuing the reaction for additional 12 h without **PCN 1** did not significantly change the cyclohexane consumption (entry 1a and 1b). When the concentration of substrate was increased, the catalytic activity also increased (entries 2-4). Finally, **PCN 1** was isolated from the reaction mixture by centrifugation, washed with acetonitrile and ethyl acetate and dried at room temperature to check its stability and carry out further reusability testing. The results clearly demonstrated that **PCN 1** retained its activity on the second catalytic run (entry 5). The PXRD patterns of the recycled network powder showed that it largely retained its diffraction peaks, both after the UV irradiation, and with and without cyclohexane in the acetonitrile

solution (Figure 2-9). FTIR spectroscopy was also performed to further confirm photostability of the heterogeneous photosensitizer. The spectra contained a peak at around 1604 and 1655 cm^{-1}, which were due to carboxylate stretching modes as shown in Figure 2-10. Minor shifts in the peak positions of both PXRD and FTIR could be attributed to the incorporation of different guest molecules into the pores of **PCN 1**. In addition to cyclohexane, heavier C8 hydrocarbons, namely *n*-octane and cyclooctane, were also investigated as substrates for photooxidation (entries 6 and 7). The achieved conversions were in the similar range of 32.9 % and 39.8 % for *n*-octane and cyclooctane, respectively. These values were lower compared to cyclohexane due to the higher molecular weight of the C8 substrates and their more inert nature.

Table 2-4 Photooxidation of saturated hydrocarbons under different conditions.[a]

Entry	Photocatalyst	Substrate	[Sub] M	Substrate consumption (%)
1a	10 mg **PCN 1**	Cyclohexane	0.05	20.8 (at 12 h)
1b	After removal of **PCN 1**			0 (additional 12 h)
2	10 mg **PCN 1**	Cyclohexane	0.5	50.9
3	10 mg **PCN 1**	Cyclohexane	0.1	44.7
4	10 mg **PCN 1**	Cyclohexane	0.01	40.4
5	10 mg **Reused PCN 1**	Cyclohexane	0.05	38.5
6	10 mg **PCN 1**	Cyclooctane	0.05	32.9
7	10 mg **PCN 1**	*n*-octane	0.05	39.8

[a]General reaction conditions: substrate concentration in 3 mL of CD_3CN, sensitizer, air balloon connected to the reaction vessel, monochromatic LED light (365 nm), the catalytic experiment was carried out for 24 h.

To compare the photooxidation performance with other reported networks, TOF values were used, which were recalculated based on cyclohexane consumption to adjust for the different reaction condition. The catalytic activity of **PCN 1** was found to be significantly greater than several other network-based sensitizers which did not rely on heavy elements,

such as UiO-66-NH_2(Zr)[40] and MIL-125-NH_2(Ti),[41] and was comparable to the two-dimensional [Hf(TPY)] (TPY = 4′-(4-benzoate)-(2,2′,2″-terpyridine)-5,5″-dicarboxylate) material (TOF = 4 h^{-1}).[42] Furthermore, **PCN 1** as a photocatalyst showed the production of CMK for the first time among them. This kind of direct comparison has some limitations since the photocatalytic experiments were performed under different conditions (light intensity, energy, power, and oxygen concentration). But nevertheless, it still provided useful assessment of different catalytic systems.

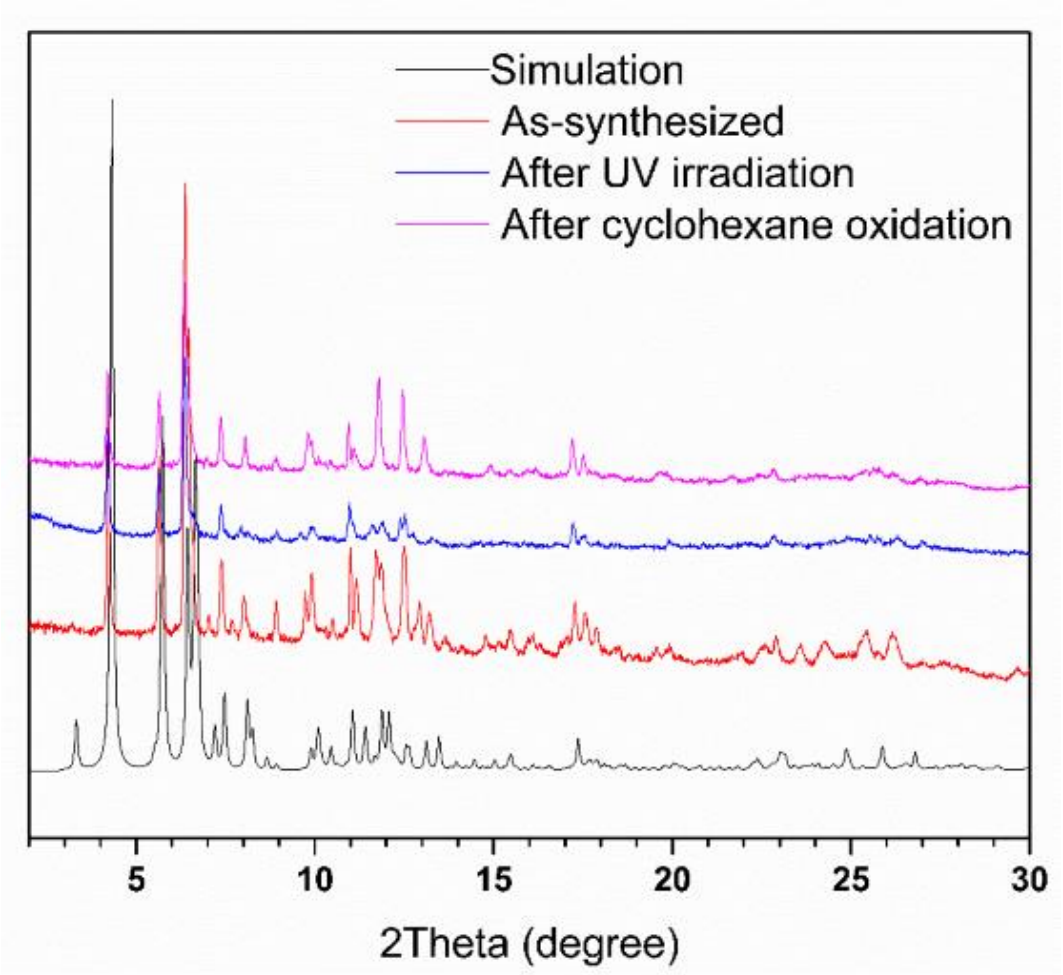

Figure 2-9 Powder X-ray diffraction (left) and FTIR (right) of **PCN 1** before and after the reaction.

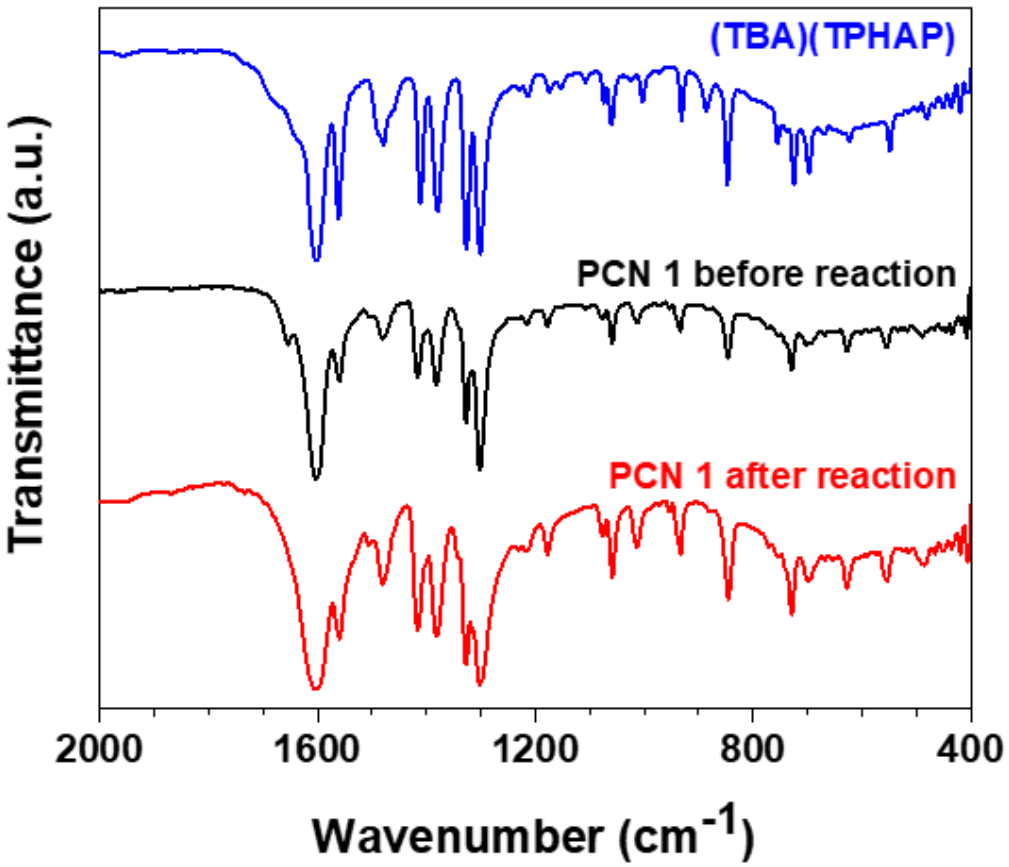

Figure 2-10 FTIR spectra of TBATPHAP**, PCN 1** before and after the reaction.

There are two possible photocatalytic pathways, one involving energy transfer to generate singlet oxygen and the other charge transfer to generate radical species. To probe which pathway played the dominant role in the photooxidation of alkanes with **PCN 1**, several control experiments were performed (Figure 2-11). There is no cyclohexane consumption in the absence of light and **PCN 1**. Under standard conditions, cyclohexane was converted with the consumption of 69 % with 30.5 μmol of total product. A convenient method to elucidate the nature of ROS that participates in the photooxidation is to employ trapping agents that can selectively capture a particular specie in the reaction mixture. Several such agents were tested, including *t*-butyl alcohol (*t*-BuOH), 2,2,6,6-tetramethylpiperidine (TEMP) and (2,2,6,6-tetramethylpiperidin-1-yl)oxyl (TEMPO), which were shown to selectively trap hydroxyl radicals, singlet oxygen and superoxide radical ions, respectively.[16, 43, 44] These three trapping

agents were difficult to convert cyclohexane itself in the absence/presence of UV light. When the photooxidation experiments were carried out in the presence of **PCN 1** with *t*-BuOH to trap hydroxyl radical, the catalytic activities were decreased to 32.2 % of cyclohexane consumption with 3.0 3μmol of total product with less product selectivity. When the photooxidation experiments were carried out in the presence of **PCN 1** with TEMP and TEMPO to singlet oxygen and superoxide radical ions, respectively, the cyclohexane consumption was dramatically decreased to 21.5 % and 14.7 %. without the existence of CMK product because competition of cross-coupling reaction between cyclohexane and TEMP or TEMPO. However, the substrate conversion did not fully cease in each case. This result is significant in that it provides compelling evidence for the involvement of both energy and charge transfer pathways in the photooxidation of alkanes.

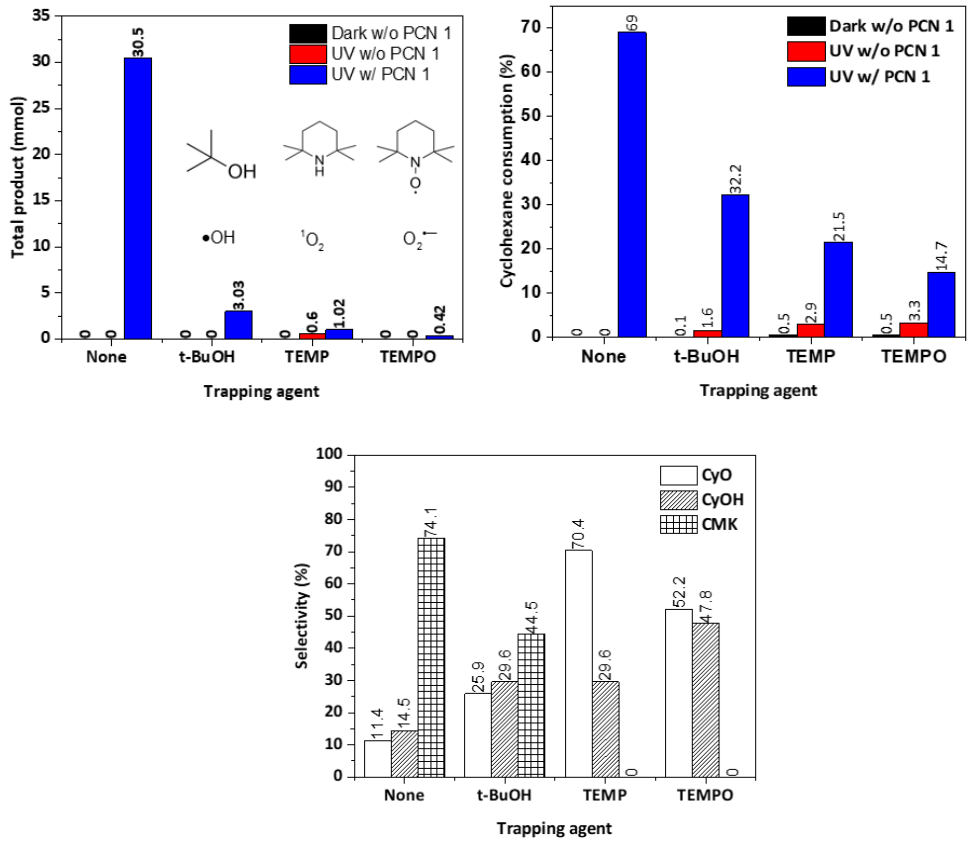

Figure 2-11 Total product, cyclohexane consumption and product selectivity under different trapping agent in the absence of light without PCN 1 (Black bar), in the presence of light without PCN 1(Red bar), and in the presence of light with PCN 1 (Blue bar); General

reaction conditions: 0.5 M of cyclohexane in 3 mL of CD_3CN, 10 mg of PCN 1 as a sensitizer, 1 eq of trapping agent, air balloon connected to the reaction vessel, monochromatic LED light (365 nm), the catalytic experiment was carried out for 24 h.

In case of charge transfer process, sacrificial electron donor such as triethylamine, triethanolamine, triphenyl phosphine etc. was needed for charge balance in the reaction condition. In fact, there is only residual water in CD_3CN solvent which could donate electron to the excited state photocatalyst in the beginning of reaction. There are some reports suggested that water can serve as sacrificial electron donor.[45, 46] Therefore, the effect of water content was investigated by removal residual water from solvent and additional water into the reaction condition. As shown in Table 2-5, When a dried solvent was used, there is a little cyclohexane consumption which probably derived by an incompletely removal of water. However, the additional 1 eq of water displayed the decrease of catalytic activity compared to the general condition. While water was donating electron for charge transfer process, water could be generated via oxidation reaction from energy transfer process that could partially inhibit the overall reaction. This result suggested that water was considered as sacrificial electron donor in this photocatalytic reaction.

Table 2-5 Effect of water content on the photocatalytic oxidation reaction of cyclohexane

	1	**2**	**3**
Solvent pretreatment	None	Dried with 3A molecular sieves	None
Additional water (μL)	None	None	27 (1 eq)
Substrate consumption (%, mmol)	69	1.2	20.7
Total product (μmol)	30.5	3.1	7.1
- Cyclohexanone selectivity (%)	11.4	14.0	10.5
- Cyclohexanol selectivity (%)	14.5	29.8	10.9
- Cyclohexyl Methyl Ketone selectivity (%)	74.1	46.2	78.6
TON (mol products/mol PCN 1)	13.5	1.37	3.13
TOF (h^{-1})	0.28	0.03	0.07

General reaction conditions: 0.5 M of cyclohexane in 3 mL of CD_3CN, 10 mg of **PCN 1** as a sensitizer, 1 eq of trapping agent, air balloon connected to the reaction vessel, monochromatic LED light (365 nm), the catalytic experiment was carried out for 24 h.

2.3 Conclusion

The ROSs generation ability of TPHAP was successfully demonstrated by interrogating its homogeneous photocatalytic activity and spectroscopic characterization. The emission spectra originating from the intramolecular charge-transfer transition could be affected by exposure to the atmospheric air, which was ascribed to the energy and charge transfer from the excited state of TPHAP to oxygen molecules, producing ROSs. The dual nature of this process, which results in the formation of both, radical and non-radical species, was additionally confirmed by the photocatalytic conversion of 1,5-DHN to juglone and degradation of several dye molecules. In particular, the kinetic parameters of 1,5-DHN photooxidation were determined from the time-dependent spectroscopic measurements. TPHAP was incorporated into a porous coordination network scaffold as a linker, in order to create a heterogeneous catalytic system and improve its utility for photocatalytic transformations. The resultant Cd(II) network, **PCN 1**, was successfully synthesized and was confirmed to retain the ROSs generation function of

TPHAP. The photocatalytic activity of **PCN 1** was tested for the alkane photooxidation reaction. The network catalyst displayed good photostability and catalytic efficiencies among pure coordination networks. Control experiments in the presence of several scavenger agents were performed, which revealed that the alkane photooxidation was facilitated by a number of ROSs, including $^{\bullet}OH$, $^1O_2$ and $O_2^{\bullet-}$ generated through both energy and charge transfer processes from the excited state of **PCN 1**.

2.4 Experimental Section

2.4.1 Materials and Methods

All reagents were purchased from commercial sources and used without further purification. ^1H NMR spectra were recorded in CD_3CN on a JEOL JNM-ECA 400 II spectrometer at 400 MHz and referenced with the residual peak at 1.94 ppm. Elemental analyses were performed on an Elementar vario MICRO cube. UV-Vis absorption and diffuse reflectance spectra were recorded on a JASCO V-770 spectrophotometer. Excitation and emission spectra were collected using a JASCO FP-8600 spectrofluorometer. Samples were dissolved in CH_3CN (anhydrous) and transferred to a fluorometer cell (F15-UV-10, GL sciences). Fluorescence lifetimes were determined by a Hamamatsu Quantaurus-Tau single-photon-counting apparatus fitted with an LED light source (excitation wavelength: 269 nm or 340 nm). ESR spectra were measured on a JES-FA 100 ESR spectrometer, JEOL. Powder X-ray diffraction was measured on a RIGAKU SmartLab diffractometer using a Cu Kα X-ray source.

2.4.2 Synthesis of [TBA][TPHAP]

The synthesis was modified from a reported procedure. 4-pyridylamidine hydrochloride (6 g, 38.2 mmol) and potassium tricyanomethanide (1.0 g, 7.75 mmol) were ground and placed in a 27 mL Teflon-lined stainless-steel autoclave, which was heated at 200 °C for 20 h. It is important to ensure that the starting reaction mixture is thoroughly dried and loaded into the

autoclave under low humidity condition. After cooling to room temperature, the solid mixture was re-dissolved in 2 M aqueous HCl, and then precipitated by addition of acetone. The resultant solid was isolated by vacuum filtration. The crude product was re-dissolved in water and adjusted to pH 8-9 with 5 M aqueous KOH. Excess amount of saturated aqueous tetra(*n*-butyl)ammonium bromide solution was added to the mixture and it was stirred for 2 h. The resultant precipitate was isolated by vacuum filtration, washed with cold water and dried to give yellow crystalline powder of [TBA][TPHAP] (the yield was typically in the range of 70-80% based on potassium tricyanomethanide); ^{1}H NMR (400 MHz, DMSO-d_6) δ8.77 (d, 6H, J = 6.05 Hz), δ8.40 (d, 6H, J = 6.60 Hz), δ3.15 (t, 8H), δ1.56 (pentet, 8H), δ1.29 (sextet, 8H), δ0.93 (t, 12H); Anal. Calcd for $C_{38}H_{61.98}N_{10}O_{6.99}$=(($C_{22}H_{12}N_9$)($C_{16}H_{36}N_4$)·($H_2O$)$_{6.9}$: C, 59.21; H, 8.10; N, 18.17. Found: C, 59.21; H, 8.05; N, 17.95.

2.4.3 Synthesis of PCN 1

[TBA][TPHAP] (64.4 mg, 0.1 mmol), $Cd(NO_3)_2 \cdot 4H_2O$ (30.9 mg, 0.1 mmol) and fumaric acid (11.6 mg, 0.125 mmol) were dissolved in 3 mL of DMF in a 9 mL vial and first heated at 90 °C for 10 min. Then, 3 mL of MeCN was added and the reaction solution was further heated for 2 days. After cooling down, solid sample was collected by centrifugation, and washed with DMF (3 ×5 mL), MeCN (3 × 5 mL) and acetone (3 × 5 mL). Finally, the yellow crystalline powder was dried at room temperature to give the desired **PCN 1** (32 mg, 50 % yield based on [TBA][TPHAP]). The phase purity of the product was confirmed by PXRD. Anal. Calcd for $Cd_4C_{92.75}H_{61.23}N_{37.25}O_{7.49}$=($Cd_4$($C_{22}H_{12}N_9$)$_4$($C_4H_2O_4$) $(OH)_2 \cdot (C_3H_7NO)_{0.25}$ $(H_2O)_{0.24}$: C, 50.04; H, 2.68; N, 22.63. Found: C, 49.94; H, 2.68; N, 22.63.

2.4.4 Photocatalytic Activity of TPHAP in a Homogeneous Mixture

Certain amounts of methylene blue, crystal violet, indigo dye, 1,5-dihydroxynaphthalene (1,5-DHN) and [TBA][TPHAP] (ε = 11114 $M^{-1}.cm^{-1}$) were dissolved in 3.5 mL of MeCN and

placed into a 3.5-mL quartz cuvette with a magnetic bar. The solution was stirred at 500 rpm while being irradiated by a 55W UV-LED (λ_{max} = 365 nm) (ZUV-C30H, Omron) under ambient condition. The UV-Vis spectra were recorded at different interval time.

2.4.5 Photooxidation of C6 and C8 Hydrocarbons by PCN 1

certain amount of photocatalyst, hydrocarbon substrates were added into 3 mL CD_3CN and placed into a 3.5-mL vial (borosilicate glass, CV-35 AS ONE) and sealed using a screw cap connected to an air balloon. The mixture was stirred at 500 rpm in the dark for 30 min. Then, the reaction mixture was irradiated using a 108W UV-LED (λ_{max} = 365 nm) (CL-1503, Asahi-spectra). At an interval time, a small sample was taken and mixed with internal standard. The reaction conversions were calculated from calibration curve of chromatogram using anisole as an internal standard, as shown in Scheme 2-2. In case of a total product and selectivity, ethyl acetate was used to extract all compound from the reaction mixture (3 mL × 3 times) and then evaluated by gas chromatography (8890 GC, Agilent) equipped with a mass spectrometer (5977B GC/MSD, Agilent) using a combined column, HP-5 MS + HP-1 (60 m × 0.25 mm × 0.25 μm).

$$\textbf{Substrate consumption (\%)} = \frac{(\text{mole of Cyclohexane})_{t\text{-}0}}{\text{mole of Cyclohexane}_0} \times 100$$

$$\textbf{Conversion (\%)} = \frac{(\text{moles of CyO, CyOH and CMK})}{\text{mole of Cyclohexane}_0} \times 100$$

$$\textbf{TON (mol/mol)} = \frac{(\text{moles of CyO, CyOH and CMK})}{\text{mole of PCN 1}}$$

$$\textbf{TOF } (h^{-1}) = \frac{\text{TON}}{\text{reaction time}}$$

$$\textbf{Selectivity (\%)} = \frac{(\text{moles of selected product})}{(\text{moles of CyO, CyOH and CMK})} \times 100$$

Scheme 2-2 Equations used for the calculation of substrate consumption, conversion, TON, TOF and selectivity.

2.4.6 Single Crystal Structure Determination

The diffraction data of **PCN 1** was recorded using Rigaku Varimax diffractometer with Saturn system equipped Rigaku GNNP low temperature device using graphite-monochromated Mo Kα radiation (wavelength = 0.71073 Å). All diffraction images were processed using CrysAlis Pro software. The structures were solved by the direct method (SHELXT-2018) and refined by full-matrix least squares calculations on F^2 (SHELXL-2018) using the SHELX-TL program package. All non-hydrogen atoms were refined with anisotropic displacement parameters. All hydrogen atoms were created with ideal geometry and refined using a riding model. $C_{92}Cd_4N_{36}O_9$, *M*r = 2202.88, Monoclinic, $P2_1/c$, a = 26.562(3) Å, b = 31.995(3) Å, c = 17.542(3) Å, β = 91.991(12)°, V = 14899(3) Å^3, T = −150 °C, Z = 4, ρ_{calcd} = 0.982 g cm^{-3}, μ = 0.611 cm^{-1}, 6051 unique reflections with I>2σ (*I*), 393 parameters, 5.092°< θ <55.12°, R_1= 0.1171, wR_2= 0.3066, GOF = 0.942.

2.4.7 Photooxidation Reactions of 2-methyl-1-butene, Isoprene, Furfural, and Tetrahydrofuran.

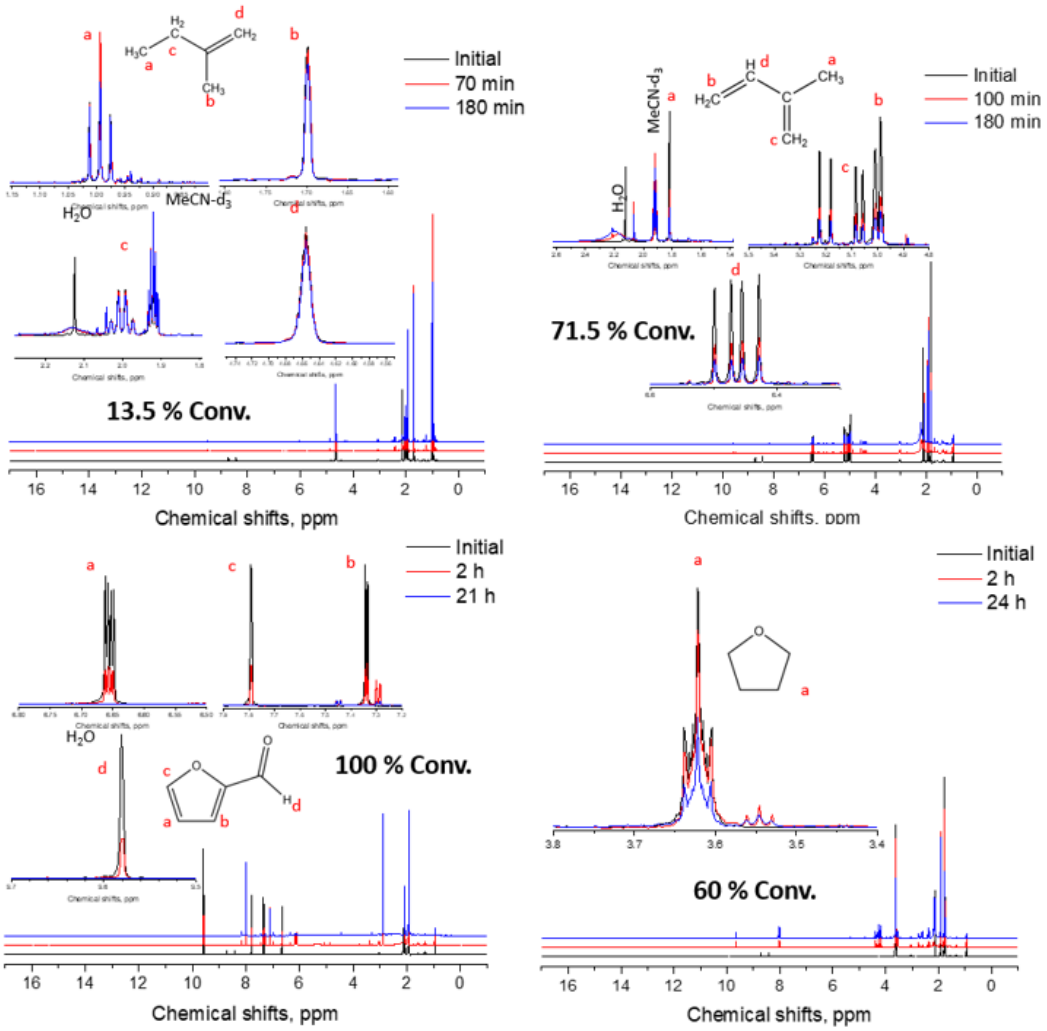

Figure 2-12 *In situ* ^{1}H NMR spectra showing the progression of the photooxidation reactions of 2-methyl-1-butene, isoprene, furfural, and tetrahydrofuran using TPHAP as a photocatalyst in CD_3CN solvent.

Figure 2-13 Experimental set up for the *in situ* ^{1}H NMR photoreactor.

Table 2-6 Fluorescence Lifetimes of TPHAP anion in MeCN with excitation at 340 nm in different temperature.

λ_{em}(nm)	333 K		298 K		243 K	
	χ^2	τ (ns)	χ^2	τ (ns)	χ^2	τ (ns)
420	1.12	0.928	1.18	1.094	1.09	1.512
480	0.98	1.583	1.34	1.204	1.18	1.024
540	1.32	1.697	1.09	1.308	1.15	1.164

Table 2-7 Fluorescence Lifetimes of TPHAP anion in MeCN with excitation at 269 nm in different temperature.

λ_{em}(nm)	298 K		233 K	
	χ^2	τ (ns)	χ^2	τ (ns)
400	1.02	1.354	1.23	1.762
420	1.18	1.353	1.16	1.820
440	1.18	1.382	1.18	1.826
480	1.19	1.425	1.18	1.842

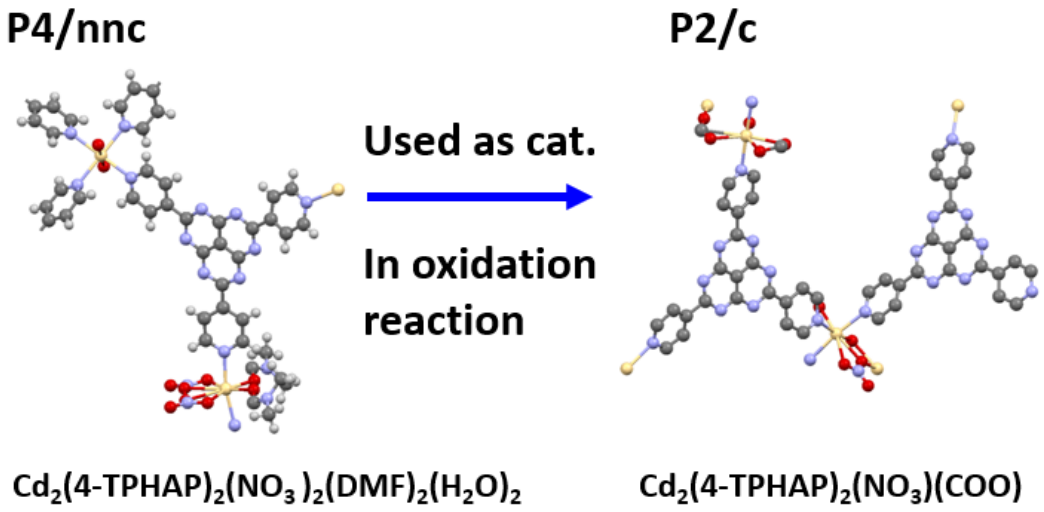

Figure 2-14 Example of TPHAP-based PCN network transformation after oxidation reaction.

Table 2-8 Screening of TPHAP-based PCNs

Networks	Metal precursor	Co-ligand	Structure	Crystallographic data
Cd-1 (Cd (TPHAP)(I_2) (DMF)(H_2O))	CdI_2	None	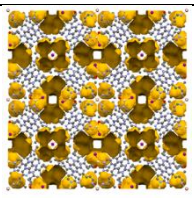	Tetragonal P_4/nnc *a*=*b*: 28.3348(1) Å *c*: 9.9417(1) Å Vol: 8034 Å^3
Cd-2 (Cd(TPHAP)(I)(H_2 O))	CdI_2	None	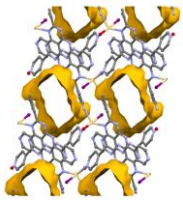	Triclinic P-1 *a*: 9.6530(3) Å *b*: 11.4205(4) Å *c*: 13.7668(4) Å α: 95.932(2)° β: 99.582(2)° γ: 105.113(3)° Vol: 1427 Å^3
Cd-3 (Cd_3(TPHAP)(BDC) $_{2.5}$(DMF))	$Cd(NO_3)_2$	Benzene dicarboxylic acid	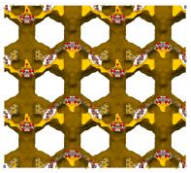	Monoclinic $P2_1/m$ *a*: 14.6280(5) Å *b*: 31.5513(7) Å *c*: 19.2486(8) Å β: 102.921(4)° Vol: 8658 Å^3
Cd-4 (Cd_2(TPHAP)(BDC) $_{1.5}$	$Cd(NO_3)_2$	Benzene dicarboxylic acid	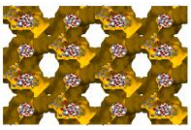	Monoclinic C2/c *a*: 31.018(2) Å *b*: 19.8549(10) Å *c*: 21.0409(18) Å β: 92.274(7)° Vol: 12948 Å^3
Cd-5 Cd_4(TPHAP)$_4$(NO_3) $_2$(tartarate)	$Cd(NO_3)_2$	Tartaric acid	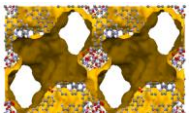	Monoclinic $P2_1/c$ *a*: 27.0556(12) Å *b*: 32.0177(7) Å *c*: 17.4802(11) Å β: 92.117(5)° Vol: 15097 Å^3
Co-1 (Co_2(TPHAP)(BDC) $_{1.5}$(DMF)	Co precursor	Benzene dicarboxylic acid	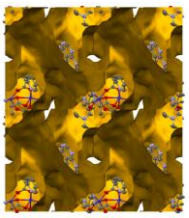	Monoclinic $P2_1/n$ *a*: 15.0123(4) Å *b*: 16.9888(4) Å *c*: 29.1417(6) Å β: 101.904(2)° Vol: 7272 Å^3

Co-2 (Co_2(TPHAP)(BDC)$_{1.5}$	Co precursor	Benzene dicarboxylic acid	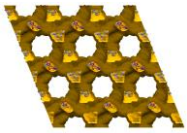	Monoclinic C2C *a*: 30.290(4) Å *b*: 20.521(3) Å *c*: 21.822(3) Å β: 90.609(14)° Vol: 13563 Å^3
Co-3 (Co_3(TPHAP)(BDC)$_2$(OH)	Co precursor	Benzene dicarboxylic acid	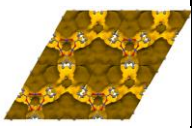	Hexagonal $P6_3/mmc$ *a*=*b*: 19.0495(6) Å *c*: 11.9997(8) Å γ: 120(4)° Vol: 3771 Å^3
Co-4 (Co_3(TPHAP)(BDC)$_{2.5}$(DMF))	Co precursor	Benzene dicarboxylic acid	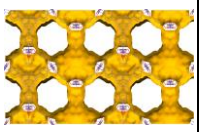	Monoclinic $P2_1/m$ *a*: 14.5920(17) Å *b*: 31.036(3) Å *c*: 18.702(2) Å β: 91.259(4)° Vol: 8467 Å^3

- A non-porous **Cd-1** was synthesized at room temperature for several day or by solvothermal in DMF at 90 °C for 1 days. A **Cd-2** was synthesized by solvothermal in the mixture of MeCN/DMF (1:1) at 90 °C for 1 days. These **Cd-1** and **Cd-2** were successfully produced with pure phase, but it is not stable against oxygen contained solvent (reagent).
- A **Cd-3** and **Cd-4** were synthesized by solvothermal in DMF at 90 °C for 2 days with an adjustment of ratio metal, TPHAP and BCD, carefully. However, these two networks were still generated together.
- Similar to above, a **Cd-5** was synthesized by solvothermal in DMF at 90 °C for 2 day. It is difficult to isolate this network.
- Since cobalt was used instead of cadmium, All Co-based networks were synthesized by solvothermal in DMF with an adjustment of ratio metal, TPHAP and BCD, temperature (80-150 °C), time (0.5-5 days), and cobalt precursor ($Co(NO_3)_2$, $CoBr_2$, $CoCl_2$, Co(acetate)$_2$), carefully. Note that Co-based networks do not contain the coordinated counter anion from cobalt precursor resulting in difficult to control the phase purity.

Table 2-9 Coordination mode of each TPHAP-based PCNs from the screening

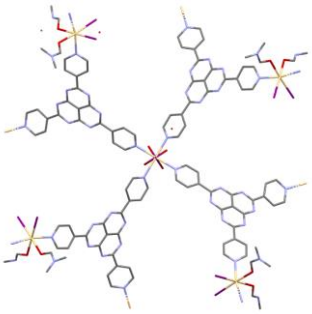	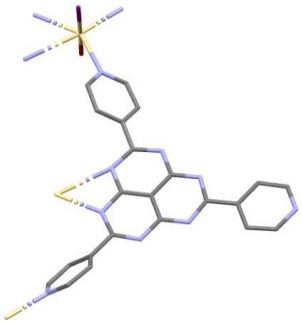	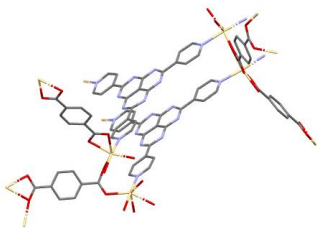
Cd-1	**Cd-2**	**Cd-3**
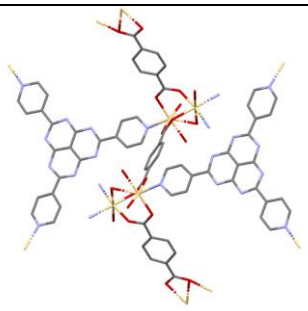	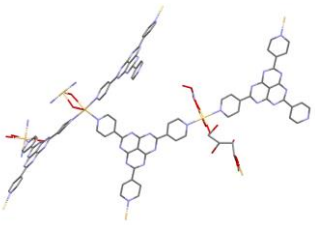	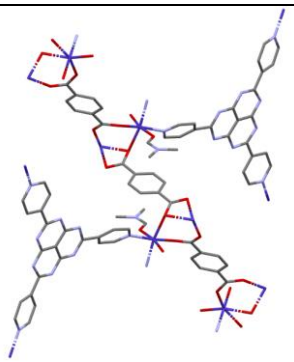
Cd-4	**Cd-5**	**Co-1**
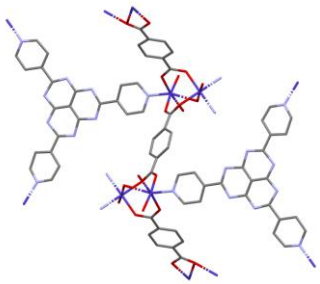	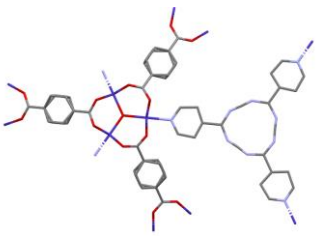	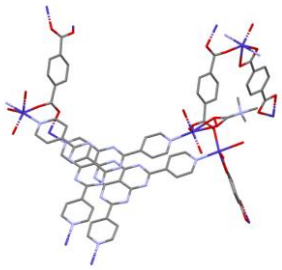
Co-2	**Co-3**	**Co-4**

2.5 References

1. Shi, Z.; Li, J.; Han, Q.; Shi, X.; Si, C.; Niu, G.; Ma, P.; Li, M., *Inorg. Chem.* **2019,** *58* (19), 12529-12533.
2. Higgins, R. F.; Fatur, S. M.; Shepard, S. G.; Stevenson, S. M.; Boston, D. J.; Ferreira, E. M.; Damrauer, N. H.; Rappé, A. K.; Shores, M. P., *J. Am. Chem. Soc.* **2016,** *138* (16), 5451-5464.
3. Le, T.; Galmiche, L.; Masson, G.; Allain, C.; Audebert, P., *Chem. Commun.* **2020,** *56* (73), 10742-10745.
4. Abedi, S.; Morsali, A., *ACS Catal.* **2014,** *4* (5), 1398-1403.
5. Wang, X.; Dong, M.-J.; Wu, C.-D., *Nanoscale* **2020,** *12* (30), 16136-16142.
6. Zhang, D.; Celaje, J. A.; Agua, A.; Doan, C.; Stewart, T.; Bau, R.; Selke, M., *Org. Lett.* **2010,** *12* (13), 3100-3103.
7. Noimark, S.; Salvadori, E.; Gómez-Bombarelli, R.; MacRobert, A. J.; Parkin, I. P.; Kay, C. W. M., *Physical Chemistry Chemical Physics* **2016,** *18* (40), 28101-28109.
8. Ide, Y.; Inami, N.; Hattori, H.; Saito, K.; Sohmiya, M.; Tsunoji, N.; Komaguchi, K.; Sano, T.; Bando, Y.; Golberg, D.; Sugahara, Y., *Angew. Chem. Int. Ed.* **2016,** *55* (11), 3600-3605.
9. Xiao, S.; Zhao, L.; Leng, X.; Lang, X.; Lian, J., *Appl. Surf. Sci.* **2014,** *299*, 97-104.
10. Zhao, J.; Chen, K.; Hou, Y.; Che, Y.; Liu, L.; Jia, D., *Org. Biomol. Chem.* **2018,** *16* (20), 3692-3701.
11. Chaudhri, N.; Grover, N.; Sankar, M., *Inorg. Chem.* **2017,** *56* (19), 11532-11545.
12. Zhang, X.; Peng, T.; Yu, L.; Li, R.; Li, Q.; Li, Z., *ACS Catal.* **2015,** *5* (2), 504-510.
13. Feng, D.; Gu, Z.-Y.; Li, J.-R.; Jiang, H.-L.; Wei, Z.; Zhou, H.-C., *Angew. Chem. Int. Ed.* **2012,** *51* (41), 10307-10310.
14. Johnson, J. A.; Zhang, X.; Reeson, T. C.; Chen, Y.-S.; Zhang, J., *J. Am. Chem. Soc.* **2014,** *136* (45), 15881-15884.
15. Gao, Y.; Xia, J.; Liu, D.; Kang, R.; Yu, G.; Deng, S., *Chem. Eng. J.* **2019,** *378*, 122118.
16. Zhao, F.-J.; Zhang, G.; Ju, Z.; Tan, Y.-X.; Yuan, D., *Inorg. Chem.* **2020,** *59* (5), 3297-3303.
17. Li, X.; Chen, D.; Liu, Y.; Yu, Z.; Xia, Q.; Xing, H.; Sun, W., *CrystEngComm* **2016,** *18* (20), 3696-3702.
18. Guo, Z.; Zhao, H.; Liu, X.; Liang, X.; Wei, H.; Mei, Y.; Xing, H., *Appl. Organomet. Chem.* **2020,** *34* (4), e5487.
19. Zhang, Y.; Pang, J.; Li, J.; Yang, X.; Feng, M.; Cai, P.; Zhou, H.-C., *Chem. Sci.* **2019,** *10* (36), 8455-8460.
20. Liu, Y.; Buru, C. T.; Howarth, A. J.; Mahle, J. J.; Buchanan, J. H.; DeCoste, J. B.; Hupp, J. T.; Farha, O. K., *J. Mater. Chem. A* **2016,** *4* (36), 13809-13813.
21. Kojima, T.; Yamada, T.; Yakiyama, Y.; Ishikawa, E.; Morita, Y.; Ebihara, M.; Kawano, M., *CrystEngComm* **2014,** *16* (28), 6335-6344.
22. Yakiyama, Y.; Ueda, A.; Morita, Y.; Kawano, M., *Chem. Commun.* **2012,** *48* (86), 10651-10653.
23. Godard, J.; Brégier, F.; Arnoux, P.; Myrzakhmetov, B.; Champavier, Y.; Frochot, C.; Sol, V., *ACS Omega* **2020,** *5* (43), 28264-28272.

24. De Bonfils, P.; Verron, E.; Sandoval-Altamirano, C.; Jaque, P.; Moreau, X.; Gunther, G.; Nun, P.; Coeffard, V., *J. Org. Chem.* **2020,** *85* (16), 10603-10616.
25. Takizawa, S.-y.; Aboshi, R.; Murata, S., *Photochem. Photobiol. Sci.* **2011,** *10* (6), 895-903.
26. Sun, J.; Zhao, J.; Guo, H.; Wu, W., *Chem. Commun.* **2012,** *48* (35), 4169-4171.
27. Wu, W.; Zhang, Q.; Wang, X.; Han, C.; Shao, X.; Wang, Y.; Liu, J.; Li, Z.; Lu, X.; Wu, M., *ACS Catal.* **2017,** *7* (10), 7267-7273.
28. Wu, W.; Yang, P.; Ma, L.; Lalevée, J.; Zhao, J., *Eur. J. Inorg. Chem.* **2013,** *2013* (2), 228-231.
29. Hallett, A. J.; White, N.; Wu, W.; Cui, X.; Horton, P. N.; Coles, S. J.; Zhao, J.; Pope, S. J. A., *Chem. Commun.* **2012,** *48* (88), 10838-10840.
30. Tanielian, C.; Schweitzer, C.; Seghrouchni, R.; Esch, M.; Mechin, R., *Photochem. Photobiol. Sci.* **2003,** *2* (3), 297-305.
31. Pawar, K. K.; Chaudhary, L. S.; Mali, S. S.; Bhat, T. S.; Sheikh, A. D.; Hong, C. K.; Patil, P. S., *J. Colloid Interface Sci.* **2020,** *561*, 287-297.
32. Gómez-Solís, C.; Juárez-Ramírez, I.; Moctezuma, E.; Torres-Martínez, L. M., *J. Hazard. Mater.* **2012,** *217-218*, 194-199.
33. Shi, Q.; Wu, S.-Y.; Qiu, X.-T.; Sun, Y.-Q.; Zheng, S.-T., *Dalton. Trans.* **2019,** *48* (3), 954-963.
34. Ding, M.; Cai, X.; Jiang, H.-L., *Chem. Sci.* **2019,** *10* (44), 10209-10230.
35. Allred, R. A.; Huefner, S. A.; Rudzka, K.; Arif, A. M.; Berreau, L. M., *Dalton. Trans.* **2007,** (3), 351-357.
36. Evans, O. R.; Lin, W., *Chem. Mater.* **2001,** *13* (8), 2705-2712.
37. Hokelek, T.; Akduran, N.; Ozen, A.; Ugurlu, G.; Necefoglu, H., *Acta Crystallogr E Crystallogr Commun* **2017,** *73* (Pt 3), 413-416.
38. Chisca, D.; Croitor, L.; Petuhov, O.; Kulikova, O. V.; Volodina, G. F.; Coropceanu, E. B.; Masunov, A. E.; Fonari, M. S., *CrystEngComm* **2018,** *20* (4), 432-447.
39. Wada, E.; Takeuchi, T.; Fujimura, Y.; Tyagi, A.; Kato, T.; Yoshida, H., *Catalysis Science & Technology* **2017,** *7* (12), 2457-2466.
40. Long, J.; Wang, S.; Ding, Z.; Wang, S.; Zhou, Y.; Huang, L.; Wang, X., *Chem. Commun.* **2012,** *48* (95), 11656-11658.
41. Zhao, X.; Zhang, Y.; Wen, P.; Xu, G.; Ma, D.; Qiu, P., *Mol. Catal.* **2018,** *452*, 175-183.
42. Shi, W.; Cao, L.; Zhang, H.; Zhou, X.; An, B.; Lin, Z.; Dai, R.; Li, J.; Wang, C.; Lin, W., *Angew. Chem. Int. Ed.* **2017,** *56* (33), 9704-9709.
43. Hong, B.; Aganda, K. C. C.; Lee, A., *Org. Lett.* **2020,** *22* (11), 4395-4399.
44. Liang, X.; Guo, Z.; Wei, H.; Liu, X.; Lv, H.; Xing, H., *Chem. Commun.* **2018,** *54* (92), 13002-13005.
45. Zhang, W.; Gacs, J.; Arends, I. W. C. E.; Hollmann, F., *ChemCatChem* **2017,** *9* (20), 3821-3826.
46. Mifsud, M.; Gargiulo, S.; Iborra, S.; Arends, I. W. C. E.; Hollmann, F.; Corma, A., *Nat. Commun.* **2014,** *5* (1), 3145.

Chapter 3

Pyridinium Modification of a Hexaazaphenalene Skeleton: Structure and Spectroelectrochemical Analysis

Abstract

N-alkylation of tris(4-pyridyl) hexaazaphenalene (TPHAP) anion afforded corresponding pyridinium derivatives. These compounds typically existed in their dicationic states and exhibited significantly enhanced π-π interactions within stacked dimers due to a change in charge distribution induced by pyridinium moieties. This behavior was attributed to the reduction in anion-anion repulsion between the HAP cores. In addition, the presence of substituted alkyl pyridinium groups and corresponding counter anions modified the molecular packing of these derivatives. Molecular orbital calculations of pyridinium analogues revealed close similarity of the shapes of their HOMO and LUMO to the unsubstituted TPHAP with significantly lowered energies. Solution-state electrochromism was investigated by *in situ* spectroelectrochemical analysis. The electrochemical reduction was accompanied by the appearance of new absorption bands in the visible and NIR ranges.

3.1 Introduction

Stimuli-responsive organic molecular materials have garnered a considerable attention for many potential applications, including energy storage, memory devices, sensors, conductors, and photo/electrochromic devices.[1] One of the key advantages of these materials is their lower costs of manufacturing and processing, easy scalability, and chemical tunability compared to the existing alternatives based on inorganic compounds. The physical and chemical properties of organic molecules can be precisely controlled and adjusted through application of external forces, such as light, pressure, electric current, heat, or chemical agents. This feature is the key to the development of multifunctional materials based on these molecules.[2]

Among numerous classes of organic compounds, methyl viologen and pyridinium derivatives are particularly promising candidates that are amenable to such external modulation.[3] These species contain positively charged nitrogen centers inside the pyridinium ring system, which dramatically lowers their orbital energy levels and increases their electron acceptor ability. As a result, donor-acceptor type energy transfer processes can be significantly enhanced in these compounds.[4] Because of this phenomenon, the pyridine-to-pyridinium conversion presents one of the most straightforward strategy for modification of electronic and chemical properties of existing molecules and introduction of new functionalities.

Another strategy for creating interesting functionalities is fusion of cyclic molecules to give various polycyclic structures. One notable example is phenalene, a highly symmetrical (D_{3h}) aromatic hydrocarbon.[5-7] This molecule has a unique electronic structure, which enables it to support a stable neutral π-radical.[8] However, phenalene-based systems have found limited uses in practical applications due to difficult synthesis, poor stability, and propensity of their radicals to dimerize.[9] Some of these drawbacks can be mitigated by changing substituents or replacing carbon atoms with heteroatoms, such as nitrogen, to create various azaphenalene analogues. Increasing the number of heteroatoms in the phenalene core leads to lowering of its orbital energy levels, making it less susceptible to oxidation.[10, 11] Furthermore, the nitrogen centers could act as Brønsted acid and base sites giving azaphenalene systems additional

hydrogen bonding abilities. The modification of phenalene can also lead to changes in the dimer packing structures, which are crucial for determining their physical properties.[12]

Previously, the functionalization of hexaazaphenalene (HAP) core with pyridyl groups creating a highly versatile molecule, 2,5,8-tri(4-pyridine-4-yl)-1,3,4,6,7,9-hexaazaphenalene (TPHAP) was reported by Kawano. It consists of a highly stabilized and delocalized negative charge, a large aromatic plane suitable for π-π stacking, as well as multiple interactive sites on its periphery that can participate in various intermolecular interactions.[13] In this work, I aimed to explore the effect of chemical modification of TPHAP on its structural properties and packing arrangement. More specifically, the terminal pyridines were substituted with different alkyl groups to obtain a family of cationic pyridinium species. The intermolecular interactions, such as π-π stacking and electrostatic ion-ion interactions, in the structures of these derivatives were evaluated and correlated with those in the parent TPHAP. Finally, these compounds were investigated for their electrochemical and spectroelectrochemical properties.

3.2 Results and Discussion

3.2.1 Synthesis and Characterization

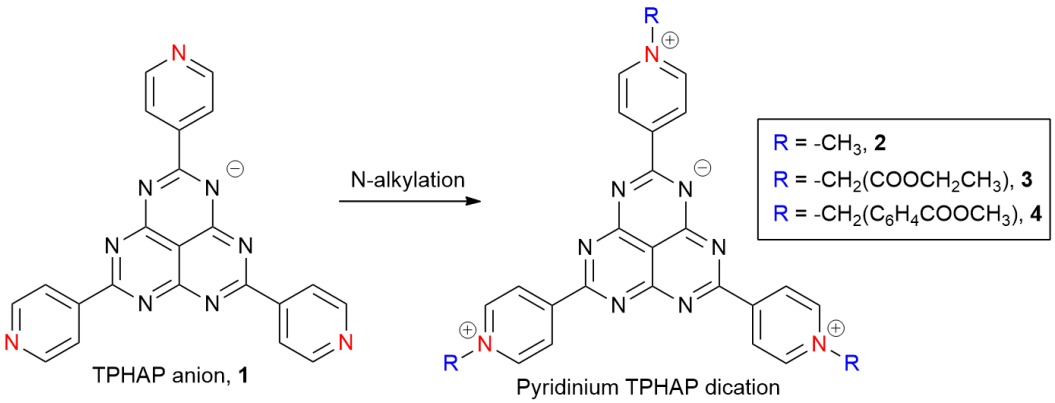

Scheme 3-1 Reactions of TPHAP with different N-alkylating agents and resultant pyridinium derivatives.

[TBA][TPHAP] was successfully prepared by cation-exchange from K[TPHAP], which afforded higher solubility in organic solvents, such as MeCN, DMF and dichloromethane. All

three new pyridinium-based TPHAP derivatives were synthesized via the standard N-alkylation reaction[14] using suitable alkylating agents, namely methyl iodide, ethyl bromoacetate and 4-(bromomethyl) benzoate resulting in Me_3TPHAP^{2+}, [(Ethyl acetate)$_3$TPHAP]$^{2+}$ and [(Methyl *p*-toluate)$_3$TPHAP]$^{2+}$ cations, respectively, as shown in Scheme 3-1. The substitution occurred only at the pyridine sites, with the HAP core remaining unchanged because of weak Lewis basicity of its nitrogen centers. These compounds were obtained as dication salts, where the three positive charges on terminal pyridiniums were coexisting with the negative charge delocalized on the HAP core. Suitable single crystals of all compounds for structure determination were obtained, with the crystal data summarized in Tables 3-4 and 3-5.

3.2.2 Crystal Structures

The crystals of **1**, [TBA][TPHAP], were grown by dissolving the compound in a small amount DMSO, followed by addition of water to get to 1:9 DMSO:H_2O ratio, and then keeping the mixture at 5 °C. The crystal structure is shown in Figure 3-1. It consisted of two pairs of TPHAP anions intercalated by TBA cations with 14 water molecules located around the TPHAP anion. This packing structure exhibited two types of interactions: the TPHAP anions formed two distinct slipped stacking dimers with the corresponding π-π distances of 3.434(2) and 3.445(3) Å (Figure 3-1c). Furthermore, there were two types of hydrogen bonding interactions: N(TPHAP)···H(H_2O) and O(H_2O)···O(H_2O) with the distances of 2.8 – 3.0 Å, indicating interactive nature of the HAP core (Figure 3-2). Overall, the molecular structure crystallized in a monoclinic space group, $P2_1/c$, and consisted of 2D-sheets of water···TPHAP dimer-like anion layers and TBA cation layers (Figure 3-1b). As mentioned earlier, the antiparallel dimers of HAP skeletons co-existed with small counter cations, which were able to interact with nitrogen atoms on the HAP, either through ionic bonds (for Na^+ and K^+) or hydrogen bonds (for NH_4^+). These additional HAP-cation interactions resulted in the

shortening of π-π distances to around 3.24 – 3.40 Å compared to the [TBA][TPHAP] structure.[11, 13, 15-17]

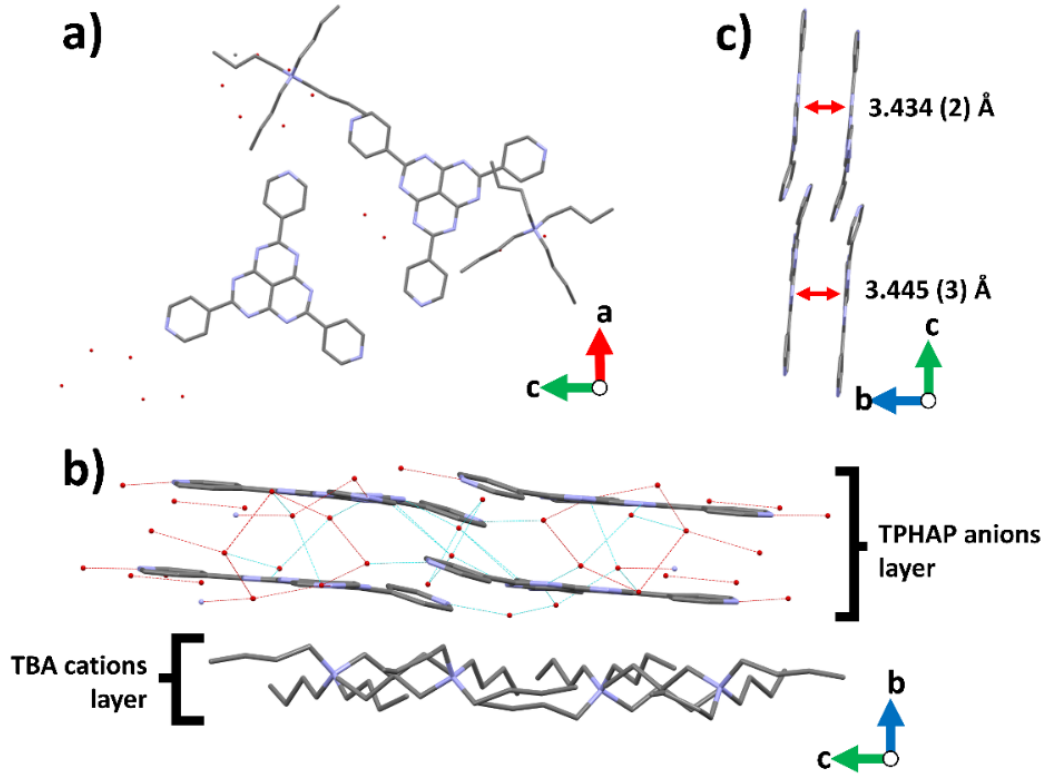

Figure 3-1 Crystal structure of **1**. a) Asymmetric unit view along the b-axis. b) Packing structure along the a-axis showing the hydrogen bonding interaction (dot lines) between TPHAP-water and water-water molecules. c) π-π stacked dimers of TPHAP. All hydrogen atoms were omitted for clarity. C – grey, N – blue, O – red.

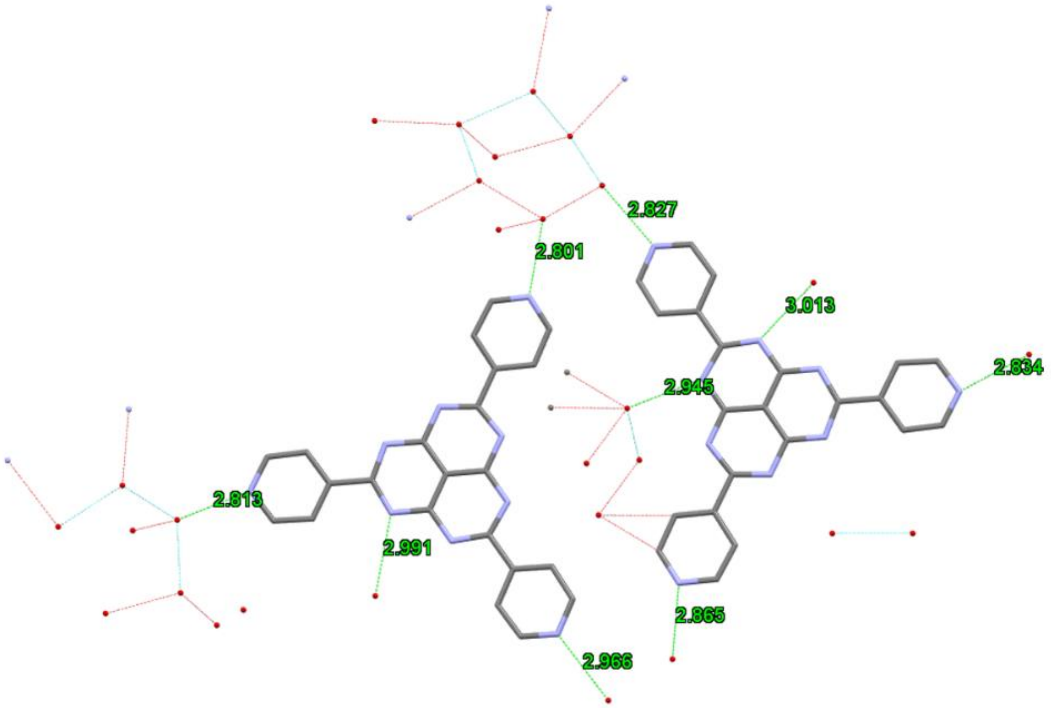

Figure 3-2 Crystal structure of **1** showing intermolecular interaction distances. Hydrogen atoms were omitted for clarity. C – grey, O – red, and N – blue.

The single crystal of **2**, the PF_6^- salt of $[Me_3TPHAP]^{2+}$, was obtained by vapor diffusion method from a MeCN/2-propanol solution of the sample and DME vapor at room temperature. The crystal structure (Figure 3-3) was solved in a high symmetry tetragonal space group, *I4/m*. It consisted of one di-cationic Me_3TPHAP unit with the total charge balanced by PF_6^- anions, disordered with a 2 total site occupancy (Figure 3-3a). Antiparallel dimeric stacking structure was constructed where one pyridinium side curved out-of-plane from the rest of the molecule. The π-π distance in the resultant dimer was found to be 3.282(9) Å between the HAP cores (Figure 3-3b). Unexpectedly, these bowl-shape fragments arranged in a concave-concave manner (Figures 3-3c and 3-4), probably due to low steric hindrance of methyl groups enabling stronger interactions between positive charges on pyridiniums and the negative charge on HAP. There are a limited number of reports detailing such biconcave stacking arrangement. One example is a corannulene dimer unit encapsulated in a Pd-cage. In that case, the restrictive

space of the cage enforces the stacking.[18-20] In addition, the di-cation dimer exhibited a π-sandwich herringbone motif connected via van der Waals forces of (PF_5^-)–F···π[21, 22] and weak hydrogen bonds (Table 3-1),[23] giving rise to an overall packing structure shown in Figure 3-3e. Nitrogen atoms on the HAP interacted with the hydrogen atom from methyl groups, whereas a pyridinium ring and a fluorine atom of PF_6^- interacted with another pyridinium ring (Figure 3-3d).

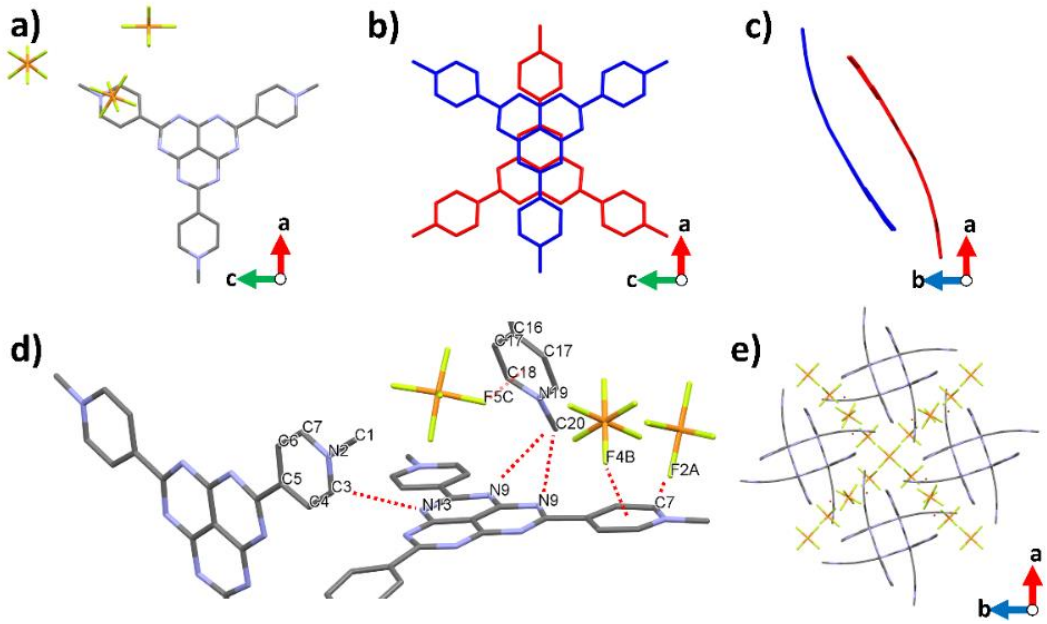

Figure 3-3 Crystal structure of **2**. a) Asymmetric unit view along the b-axis. View of π-sandwich herringbone motif along b) the b-axis and c) the c-axis. d) Intermolecular interactions shown in red dot lines. e) Packing structure along the c-axis. All hydrogen atoms were omitted for clarity. C – grey, N – blue, O – red, P – orange, and F – green.

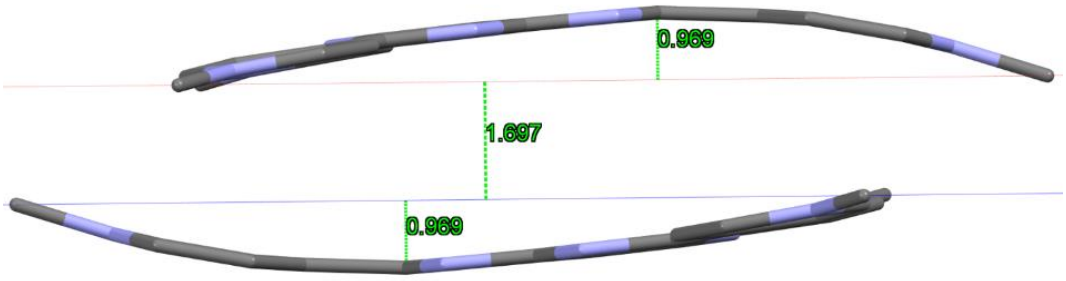

Figure 3-4 π-sandwich dimer motif in the structure of **2**. PF_6^- anions and hydrogen atoms were omitted for clarity. C – grey and N – blue.

In the case of compound **3**, PF_6^- salt of $[(\text{Ethyl acetate})_3\text{TPHAP}]^{2+}$ was crystallized using similar condition to the crystal **2**, with its structure shown in Figure 3-5. It arranged in a lower symmetry triclinic space group, *P-1*, due to additional flexibilities arising from ethyl acetate groups and the inclusion of DME solvent of crystallization (Figure 3-5). Antiparallel slipped stacking dimers of HAP skeletons were still present with the separation of 3.342(4) and 3.280(3) Å (Figures 3-5b and 5c).

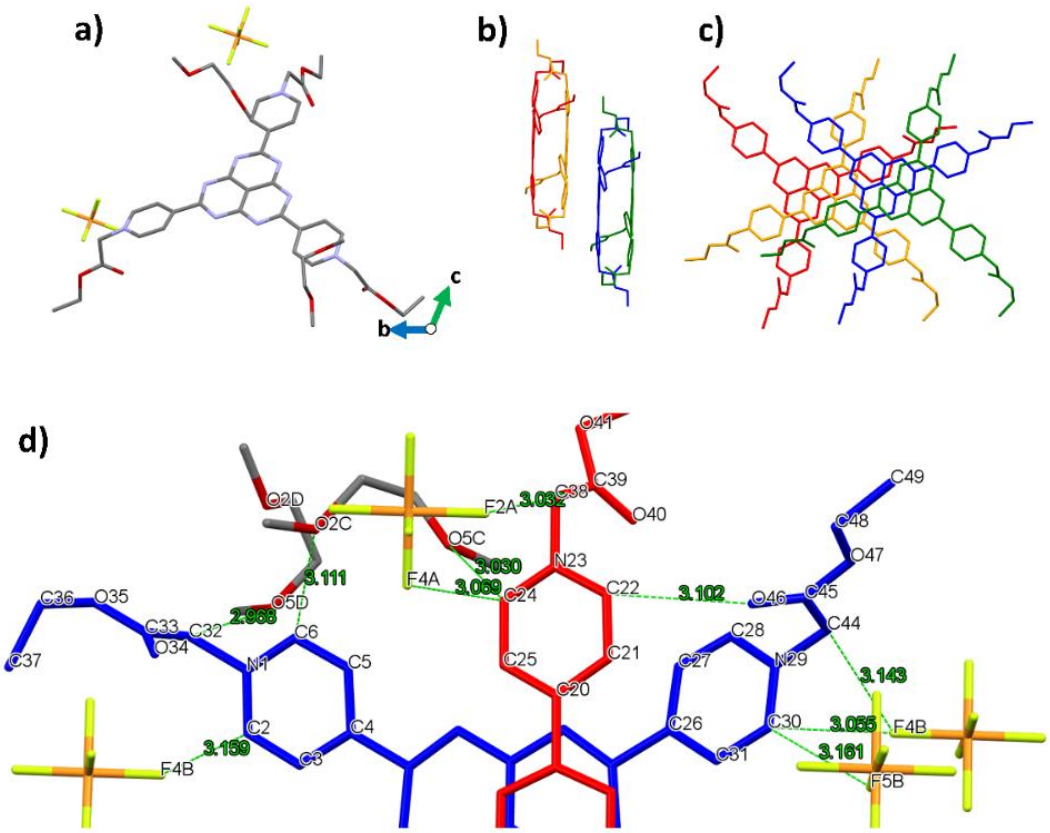

Figure 3-5 Crystal structure of **3**. a) Asymmetric unit view along the a-axis. b) π-π stacked dimers. c) Packing view perpendicular to the HAP plane. d) Intermolecular interactions shown in green dot lines. Individual molecules are shown in different colors. All hydrogen atoms were omitted for clarity. C – grey, N – blue, O – red, P – orange, and F – green.

The crystal of compound **4** was obtained in the form of a bromide salt from hot methanol recrystallisation (Figure 3-6). The presence of additional phenyl groups did not affect the π-π interaction between the HAP cores. Two types of slipped-stacking dimers with separation of 3.169(9) and 3.289(11) Å had arranged along the *a*-axis (Figure 3-7) where they were surrounded by bromide anions and water molecules. The phenyl groups showed π-π slipped stacking perpendicular to HAP dimers (Figure 3-6c).[24] Instead of Van der Waals interactions, which were predominant in the compound **2**, hydrogen bonding between N(TPHAP)···H(H_2O) and O(H_2O)···O(H_2O) and weak hydrogen bonding between C(sp^3)–H···N, C(sp^2)–H···F–(PF_5^-) were observed. Additional intermolecular C–H···O–(CO) weak hydrogen bonds had formed

from O(carbonyl) with H(pyridyl) and H(sp^3), as summarized in Table 3-1.[21, 22] Moreover, the structures of **3** and **4** did not display the bowl-shape π dimer motifs. This behavior was attributed to increased steric interference from the substituent alkyl groups, which decreased the inter-dimer interactions.

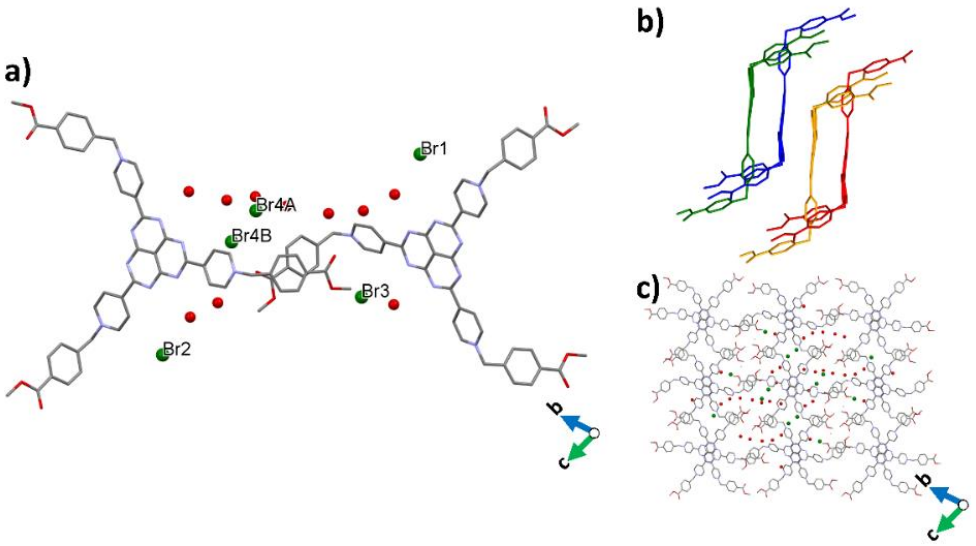

Figure 3-6 Crystal structure of **4**. a) asymmetric unit view along the a-axis. b) π-π stacked dimers. Individual molecules are shown in different colors. c) Packing view perpendicular to the HAP plane. All hydrogen atoms were omitted for clarity. C – grey, N – blue, O – red, and Br – dark green.

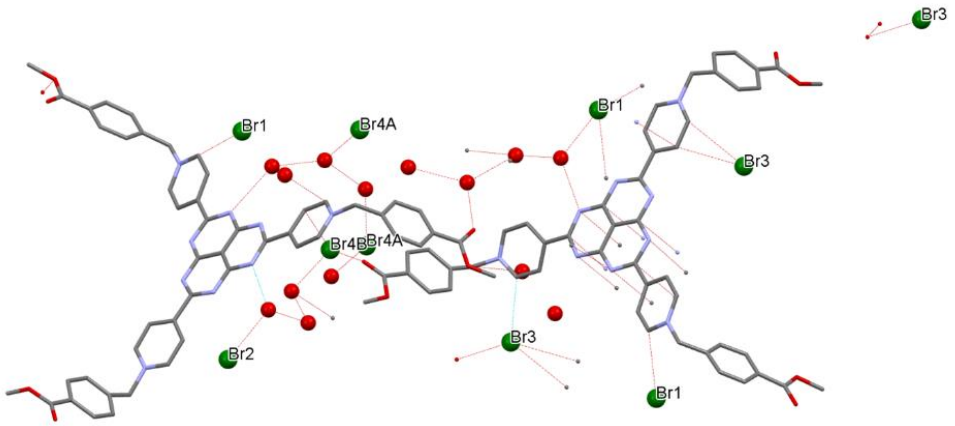

Figure 3-7 Crystal structure of **4** showing intermolecular interactions. All hydrogen atoms were omitted for clarity. C – grey, N – blue, O – red, and Br – dark green.

Table 3-1 Summary of weak hydrogen bond interactions defined by distance and angle where x < 2.7 Å, y < 3.7 Å and 120° < θ < 180°.

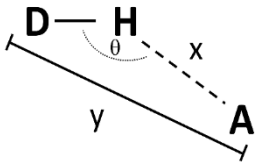

Structure	D–H···A	X (Å)	Y (Å)	θ (°)
2	N13–H3···C3	2.62	3.19	120.4
	N9–H20B···C20	2.30	3.22	160.5
	C7–H7···F2A	2.43	3.13	132.3
3	C6–H6···O2C	2.46	3.11	125.3
	C24–H24···O5C	2.31	3.03	132.4
	C22–H22···O46	2.44	3.10	126.8
	C2–H2···F7B	2.67	3.51	147.0
	C30–H30···F5B	2.22	3.16	171.6
	C44–H44A···F3B	2.60	3.14	114.4
4	C5–H5···O12	2.35	3.28	166.9
	C58–H58B···O4	2.29	3.23	156.7
	C73–H73···Br1	2.76	3.54	140.7
	C59–H59···Br3	2.86	3.53	127.9
	C64–H64C···O10	2.33	3.31	174.2
	C50–H50C···O6	2.61	3.52	156.1

3.2.3 DFT Calculation

All the compounds displayed a HOMO confined to the HAP skeleton and a LUMO delocalized across the entire molecules. N-alkylation modifications of the terminal pyridine groups of TPHAP did not significantly alter the orbital shapes and their symmetry. However, the energy levels of both HOMO and LUMO dramatically decreased compared to the parent TPHAP because of the change in the total charge state from mono-anion to di-cations. In addition, energy gaps of the alkylated analogues, **2**, **3** and **4**, decreased from 3.747 eV to 3.100, 3.107 and 3.131 eV, respectively (Figure 3-8).

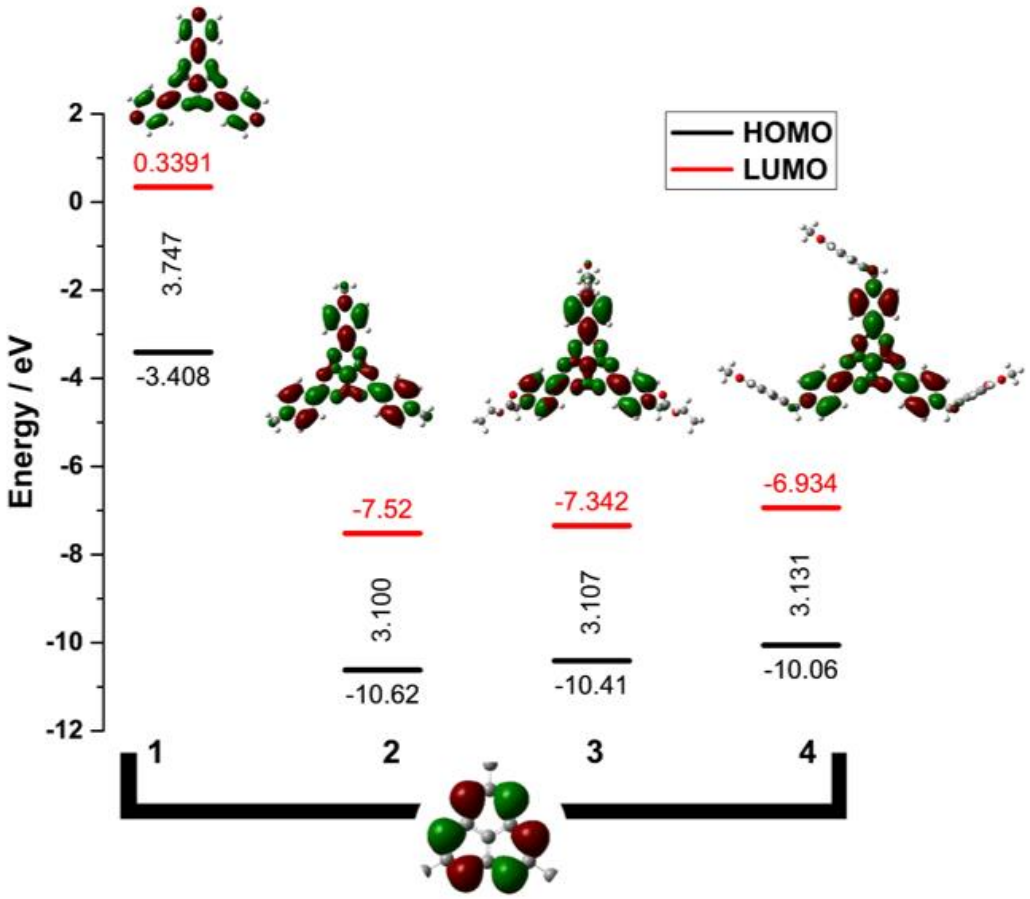

Figure 3-8 HOMO and LUMO energy levels calculated by DFT method with B3LYP/6-31G* level of theory.

3.2.4 Electrochemical Properties

The parent TPHAP and the three pyridinium derivatives were investigated by cyclic voltammetry, performed in $TBAPF_6$/DMF supporting electrolyte, as shown in Figure 3-9 and Table 3-2. TPHAP anion displayed a one-electron reversible reduction process at $E_{1/2}$ = -2.23 V vs $Fc^{0/+}$ attributed to the formation of di-anion radical ($TPHAP^{2-\bullet}$). Calculation of the singly occupied molecular orbital (SOMO) level for the one electron reduction product suggested that the radical was delocalized across the entire molecule. By comparison, the pyridinium di-cations exhibited three reversible one-electron reduction waves. The $E_{1/2}$ of the first redox couple occurred at -1.31, -1.18 and -1.20 V vs $Fc^{0/+}$ for **2**, **3** and **4**, respectively. This process was assigned to a reduction of di-cations to a cation-radical state. The unique charge

distribution of the anionic HAP core stabilizes the pyridinium cations pushing their reduction potentials to more negative values compared to other viologen derivatives.[25-27] The $E_{1/2}$ values for the second and third peaks are summarized in Table 3-2. These were attributed to further successive one-electron reductions. Scanning to more negative potentials resulted in the appearance of additional poorly defined processes, which were likely due to the decomposition of the compounds.

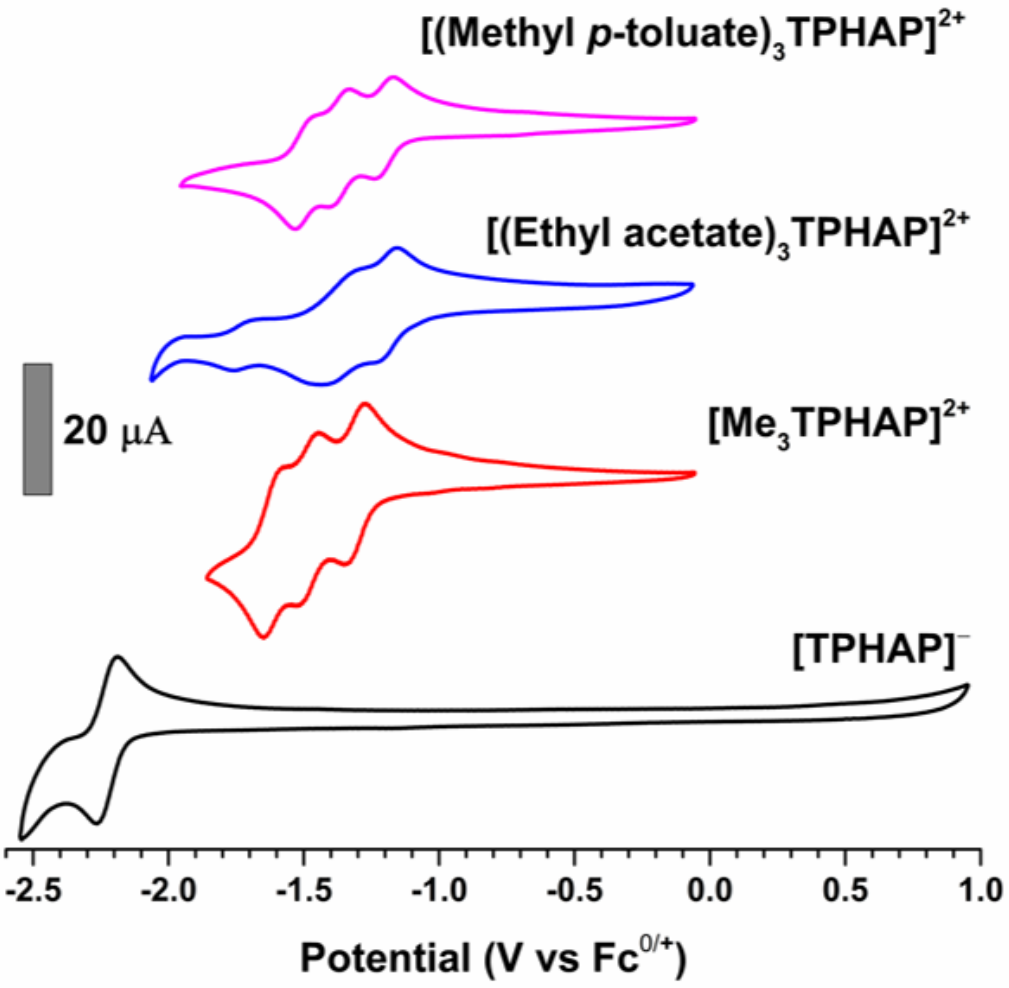

Figure 3-9 Cyclic voltammograms of compounds **1**-**4** measured in $TBAPF_6$/DMF supporting electrolyte and a scan rate of 500 mV/s.

Table 3-2 Summary of electrochemical and electronic properties.

Compound	$E_{1/2}$ (V)			HOMO (eV)	LUMO (eV)	Eg (eV)
	E^1	E^2	E^3			
TPHAP anion	-2.23			-3.408	0.3391	3.747
$[Me_3TPHAP]^{2+}$	-1.31	-1.48	-1.62	-10.62	-7.520	3.100
$[(Ethyl\ acetate)_3TPHAP]^{2+}$	-1.18	-1.34	-1.48	-10.41	-7.342	3.107
$[(Methyl\ p\text{-}toluate)_3TPHAP]^{2+}$	-1.20	-1.36	-1.49	-10.06	-6.934	3.131

3.2.5 Spectroelectrochemical Properties

The measurements were performed at room temperature under argon atmosphere in $TBAPF_6$/DMF supporting electrolyte. A thin optical cell (path length = 1 mm) equipped with Pt-gauze as a work electrode was used. The electrochemically induced changes in the electronic spectra of all compounds are shown in Figures 3-10 to 3-13. In the initial state, TPHAP anion showed an absorption band at 335 nm assigned to the intramolecular charge transfer (ICT) from the HAP core to terminal pyridyl groups.[17] In all pyridinium compounds, **2-4**, absorption spectra contained a band at 366 nm which can also be assigned to the ICT transition, similar to the TPHAP anion, because of the similar arrangement of HOMO and LUMO. In addition, the absorption energies underwent a bathochromic shift from 335 to 366 nm matching the decrease of the energy gap (Table 3-2). The spectral changes observed during spectroelectrochemical experiments are summarized in Table 3-3.

The compound **1** was reduced *in situ* by application of -2.25 V generating the radical-dianion state, $TPHAP^{2-\bullet}$. Its formation was accompanied by the appearance of new absorption bands at 596 and 750 nm, which agreed with the electronic structure calculated by TD-DFT. These bands were assigned to π-π* transitions from SOMO to higher orbitals: LUMOs delocalized over the entire molecule, and localized on pyridine groups, as shown in Figures 3-14 to 3-17.

Table 3-3 UV-Vis-NIR spectral changes observed during the spectroelectrochemical analysis.

Compound	Absorption band (nm)			
	Initial	Reduction processes		
		1	2	3
TPHAP anion	335	596		
[Me_3TPHAP]$^{2+}$	366	555	377	757, 950, 1301
[(Ethyl acetate)$_3$TPHAP]$^{2+}$	366	464, 493	370	535, 755
[(Methyl *p*-toluate)$_3$TPHAP]$^{2+}$	366	532	370	516

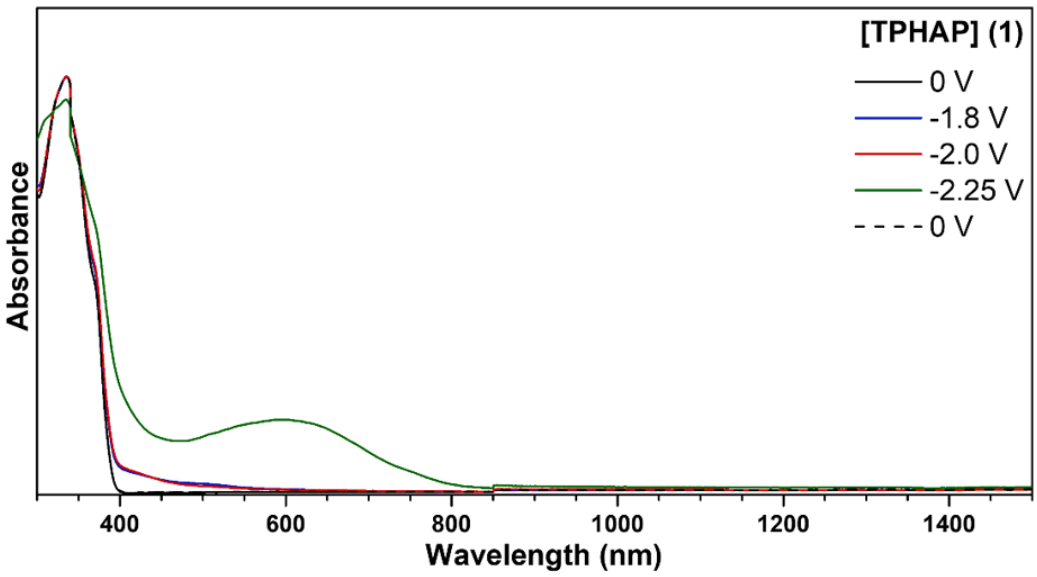

Figure 3-10 Spectroelectrochemical data for the reduction of TPHAP anion measured in $TBAPF_6$/DMF supporting electrolyte.

In the case of compounds **2-4**, since the potentials of the three reduction processes were very close to each other, the detection of spectra for each redox state in isolation was difficult to achieve. As a result, the measured spectra were likely composed of multiple species co-existing at a given potential. The reduction of the methyl analogue, **2**, at -1.45 V,

corresponding to the formation of radical cation state, resulted in an appearance of a new band at 555 nm assigned to π-π* transitions from SOMO to LUMOs, like the parent TPHAP. Application of more negative potentials gave rise to a broad feature at 800 nm, which tailed off into the NIR range. The species responsible for this change was likely the second reduction product. It was not possible to conclusively determine if it existed in a singlet or a triplet biradical states. However, this new band resembles intervalence charge transfer (IVCT) transitions typically observed in other viologen derivatives.[28] Therefore, this assignment is likely similar for the reduction product of **2**.

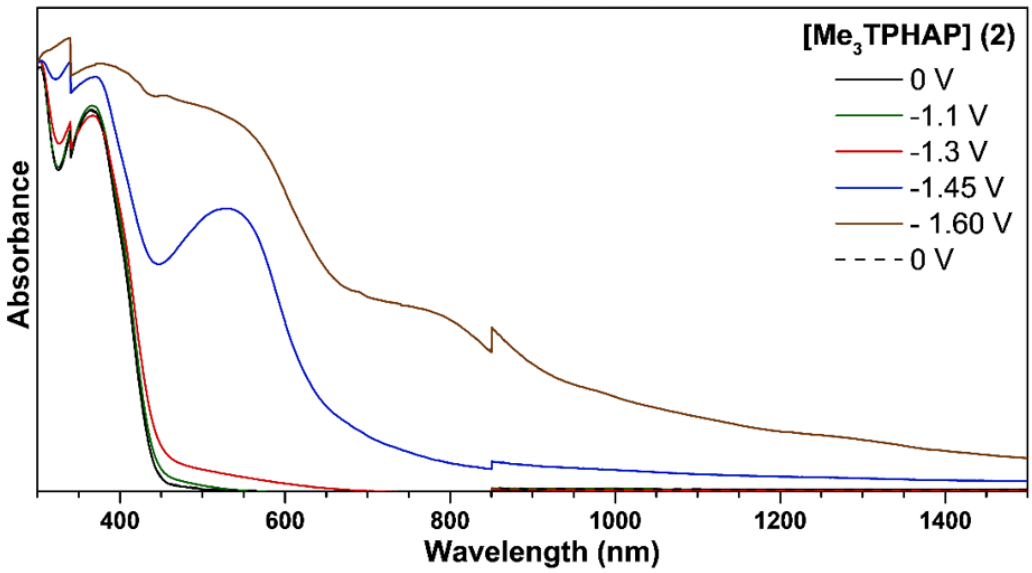

Figure 3-11 Spectroelectrochemical data for the reduction of $[Me_3TPHAP]^{2+}$ measured in $TBAPF_6$/DMF supporting electrolyte.

Spectroelectrochemical analysis of the ethyl acetate analogue, **3**, showed similar behavior to **2**. First, a band at 493 nm appeared at -1.1 V. In this case however, TD-DFT calculation showed that this transition was intramolecular in character with the electron density shifting from the pyridinium group to the HAP core. When potential was increased to -1.6 V, a similar broad band appeared at 800 nm, which was also assigned to the IVCT transition.

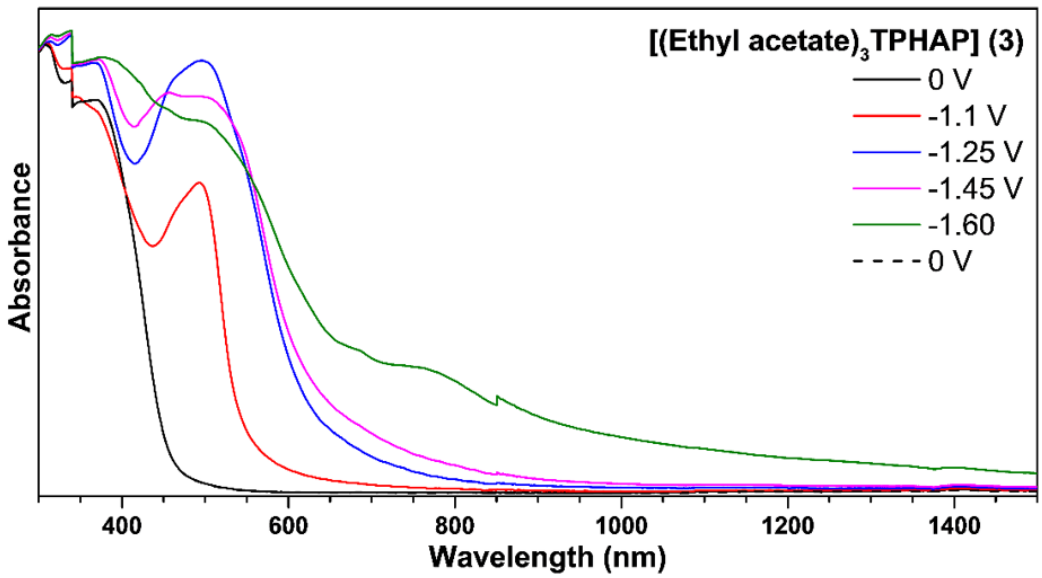

Figure 3-12 Spectroelectrochemical data for the reduction of $[(\text{Ethyl acetate})_3\text{TPHAP}]^{2+}$ measured in $TBAPF_6$/DMF supporting electrolyte.

Finally, the first reduction of methyl p-toluate analogue, **4**, exhibited similar trends to the others. The application of -1.35 V generated a band at 532 nm assigned to a π-π* transition of the radical cation state. Interestingly, the low energy bands could not be observed at more negative potential. This behavior could be due to lower stability of the neutral state of the *p*-toluate derivative on the timescale of the experiment. Overall, the tendency observed during the reduction of viologen compounds was as follows, initial di/mono-cation species absorbed in the high energy visible and UV ranges, while more reduced cation/neutral-radical species shifted their absorption to lower energy NIR range.[29, 30]

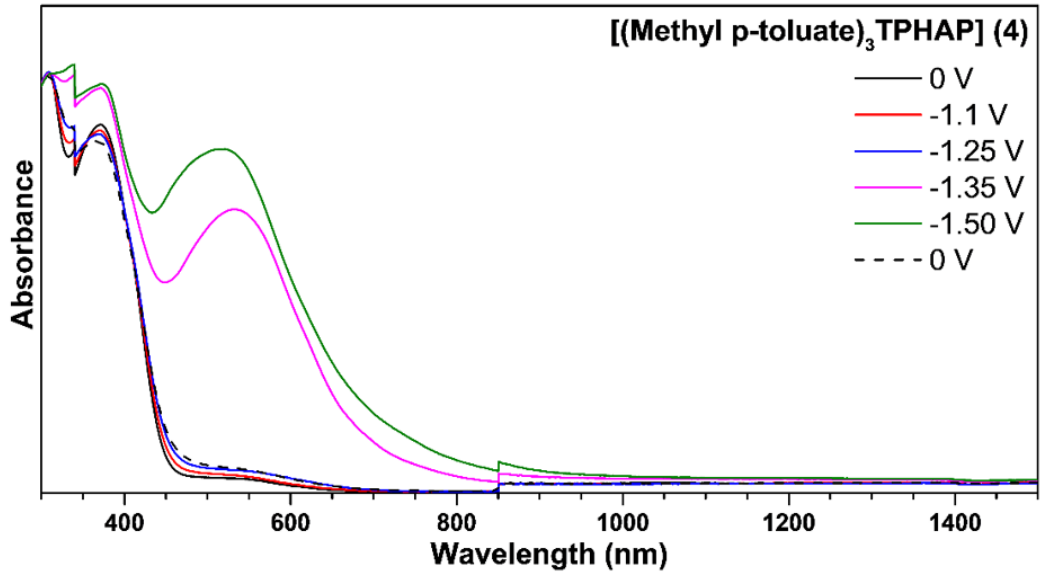

Figure 3-13 Spectroelectrochemical data for the reduction of [(Methyl *p*-toluate)$_3$TPHAP]$^{2+}$ measured in TBAPF$_6$/DMF supporting electrolyte.

3.3 Conclusion

Several pyridinium derivatives, namely methyl, ethyl acetate and methyl p-toluate were obtained by N-alkylation of TPHAP. This procedure resulted in the modification of the three terminal pyridine groups while the HAP core remained unreacted. The resultant molecules were isolated in their dicationic states. Structural analysis revealed the appearance of increased intermolecular interactivity between the neighboring molecules and counter-ions. In particular, the π-π interactions increased in strength due to N-alkylation, with π-π distances decreasing from 3.4 Å to around 3.2 Å because of the decrease in anion-anion repulsion of HAP cores. The presence of steric hindrance from alkyl groups, as well as additional weak interactions from Van der Waals forces and weak hydrogen bonding directly affected the overall structural arrangement. However, the HAP dimer motifs remained dominant in each structure. Electronic structure calculations showed that the pyridinium modification did not significantly affect the orbital geometry and distribution with HOMO localized on the HAP core and LUMO delocalized over the entire molecule. However, the orbital energy has decreased dramatically. As a result, the reduction of substituted analogues occurred at less cathodic

potentials. Furthermore, they exhibited three reversible one-electron reduction waves between -1.1 and -1.6 vs $Fc^{0/+}$. Because of lowering of HOMO-LUMO energy gaps, the ICT transition was shifted to lower energies. Spectroelectrochemistry was used to monitor the spectral changes associated with the electrochemical reduction. In general, pyridinium compounds exhibited lower energy transitions in the Vis-NIR range compared to the parent TPHAP, attributed to stronger intramolecular charge transfer interactions. These results demonstrated the utility of the pyridine-to-pyridinium modification in enhancing the functionality of TPHAP and increasing the interactivity in its molecular packing.

3.4 Experimental Section

3.4.1 Materials and Methods

All reagents were purchased from commercial sources and used without further purification. [TBA][TPHAP] (**1**) was synthesized according to Chapter 2. ^{1}H and ^{13}C (400 MHz) NMR spectra were measured on a JEOL JNM-ECA400 II instrument using deuterated DMSO-d_6 as a solvent. Cyclic voltammetry measurements were performed on a Metrohm Autolab PGSTAT101 potentiostat. 0.2 M [TBA][PF_6]/DMF was used as a supporting electrolyte. A standard three-electrode cell was employed: glassy carbon (diameter = 3 mm) was used as a working electrode, coiled Pt wire as a counter electrode and Ag/Ag^+ as a reference electrode. Ferrocene was added to the cell at the end of the experiment as an internal reference and all the voltammograms were converted to the $Fc^{0/+}$ scale. Spectroelectrochemical measurements were performed on a JASCO V-670 UV-Visible/NIR spectrometer using a 1 mm thin layer quartz glass spectroelectrochemical cell kit with platinum gauze as a working electrode, Pt wire as a counter electrode and Ag/Ag^+ as a reference electrode. The measurements were performed on 6.25 μM solutions of each compound. The potentials were applied to the cell using Metrohm Autolab PGSTAT101 potentiostat while collecting the spectra within 2.5 h. Absorption spectra were recorded in the range of 300-1500 nm while the potential was applied. Elemental analyses were performed on an Elementar vario MICRO cube.

3.4.2 Synthesis

2,5,8-tri(1-methylpyridinium)-1,3,4,6,7,9-hexaazaphenalene (2)

[TBA][TPHAP] (322 mg, 0.5 mmol) was dissolved in DMF (6.0 mL) in a 50 mL round bottom flask. Methyl iodide (124 μL, 2 mmol) was added to the solution and it was stirred at 60 °C. After 12 h, dichloromethane (20.0 mL) was added to the reaction mixture to obtain an orange slurry. The resultant precipitate was filtered and washed with dichloromethane (2 × 25 mL) and Et_2O (2 × 25 mL). The orange powder was ion-exchanged with saturated aqueous solution of NH_4PF_6 to obtain a yellow precipitate, which was isolated by vacuum filtration to give $[Me_3TPHAP](PF_6)_2$ (361 mg, 98 %); ^{1}H NMR (400 MHz, DMSO-*d*$_6$): δ9.148 (d, 6H, J = 7.15 Hz), δ8.973 (d, 6H, J = 6.60 Hz), δ4.454 (s, 9H); ^{13}C NMR (400 MHz, DMSO-*d6*): δ167.28, δ163.72, δ153.15, δ146.84, δ126.19, δ105.37, δ48.34; Anal. Calcd for $C_{25}H_{26.88}N_9O_{2.94}P_2F_{12}$ = $(C_{25}H_{21}N_9P_2F_{12})\cdot(H_2O)_{2.94}$: C, 37.99; H, 3.43; N, 15.95. Found: C, 37.99; H, 2.98; N, 15.86. *Caution: Methyl iodide is a highly toxic alkylating agent. The experimental procedure must be carried out inside a ventilated hood.*

2,5,8-tri(1-(2-ethoxy-2-oxoethyl)pyridinium)-1,3,4,6,7,9-hexaazaphenalene (3)

[TBA][TPHAP] (500 mg, 0.78 mmol) was dissolved in DMF (5.0 mL) in a 100 mL round bottom flask. Ethyl bromoacetate (0.5 mL, 4.52 mmol) was added to the solution and it was stirred at room temperature. After 12 h, Et_2O (50.0 mL) was added to the reaction mixture to obtain a yellow slurry. The resultant precipitate was filtered and washed with Et_2O (2 × 25 mL). The yellow powder was ion-exchanged with saturated aqueous solution of NH_4PF_6 to obtain a yellow precipitate, which was isolated by vacuum filtration to give $[(Ethyl\ acetate)_3TPHAP](PF_6)_2$, (691 mg, 93 %); ^{1}H NMR (400 MHz, DMSO-*d*$_6$): δ9.224 (d, 6H, J = 7.15 Hz), δ9.131 (d, 6H, J = 6.60 Hz), δ5.779 (s, 6H), δ4.287 (q, 6H), δ1.296 (t, 9H); ^{13}C NMR (400 MHz, DMSO-*d*$_6$): δ167.31, δ167.07, δ163.63, δ154.56, δ147.62, δ126.39, δ105.48, δ62.98, δ60.76, δ14.51; Anal. Calcd for $C_{34}H_{35.06}N_9O_{7.03}P_2F_{12}$ = $(C_{34}H_{33}N_9O_6P_2F_{12})\cdot(H_2O)_{1.03}$:

C, 42.01; H, 3.63; N, 12.97. Found: C, 42.01; H, 3.44; N, 13.09. *Caution: Ethyl bromoacetate is a lachrymator and a highly toxic alkylating agent. The experimental procedure must be carried out inside a ventilated hood.*

2,5,8-tri(1-(4-(methoxycarbonyl)benzyl)pyridinium)-1,3,4,6,7,9-hexaazaphenalene (4)

[TBA][TPHAP] (500 mg, 0.78 mmol) and methyl 4-(bromomethyl)benzoate (625 mg, 2.73 mmol) were dissolved in DMF (10.0 mL) in a 100 mL round bottom flask. The mixture was stirred at 90 °C for 12 h. After cooling down, Et_2O (50.0 mL) was added to the reaction mixture to obtain a brown slurry. The resultant precipitate was filtered and washed with Et_2O (2 × 25 mL). The yellow powder was ion-exchanged with saturated aqueous solution of NH_4PF_6 to obtain a yellow precipitate, which was isolated by vacuum filtration to give [(Methyl p-toluate)$_3$TPHAP](PF$_6$)$_2$ (870 mg, 98 %); ^{1}H NMR (400 MHz, DMSO-d_6): δ9.352 (d, 6H, J = 7.15 Hz), δ9.068 (d, 6H, J = 6.6 Hz), δ8.058 (d, 6H, J = 8.25 Hz), δ7.698 (d, 6H, J = 8.25 Hz), δ6.075 (s, 6H), δ3.865 (s, 9H); ^{13}C NMR (400 MHz, DMSO-d_6): δ167.33, δ166.24, δ163.70, δ154.05, δ146.43, δ139.72, δ130.89, δ130.51, δ129.68, δ127.10, δ63.05, δ52.93; Anal. Calcd for $C_{49}H_{41.28}N_9O_{7.14}P_2F_{12}$ = $(C_{49}H_{39}N_9O_6P_2F_{12})\cdot(H_2O)_{1.14}$: C, 50.72; H, 3.59; N, 10.86. Found: C, 50.72; H, 3.42; N, 11.06.

3.4.3 Single Crystal Structure Determination

The diffraction data of **1**, **3** and **4** were recorded using Rigaku Varimax diffractometer with Saturn system equipped Rigaku GNNP low temperature device using graphite-monochromated Mo Kα radiation (wavelength = 0.71073 Å). The diffraction data of **2** was recorded using Rigaku Synergy-R/DWTI APEX II diffractometer with a Hypix-6000HE detector in house equipped Rigaku GNNP low temperature device using PhotonJet-R X-ray source with MicroMax™-007 rotating anode Cu Kα radiation (wavelength = 1.54184 Å). All diffraction images were processed using CrysAlis Pro software. The structures were solved

by the direct method (SHELXT-2018) and refined by full-matrix least squares calculations on F^2 (SHELXL-2018) using the SHELX-TL program package. All non-hydrogen atoms were refined with anisotropic displacement parameters. All hydrogen atoms were created with ideal geometry and refined using a riding model. Restraints in bond lengths, angles and thermal displacement parameters were applied to the disordered fragment of butyl chain of TBA cation in **1**, and pyridinium rings in **4**. Constraints (EADP) were applied to two water molecules in **1** to avoid NPD of one of the oxygen atoms. The total occupancy factor of counter ions was defined by considering the charge balance, elemental analysis, and electrochemical analysis.

Table 3-4 Summary of crystal data of **1** and **2**.

	1	**2**
Empirical formula	$C_{76}H_{119.79}N_{20}O_{14}$	$C_{25}H_{21}F_{15}N_9P_2O_{0.5}$
Formula weight	1537.70	745.45
Temperature/K	123 (2)	123(2)
Wavelength/Å	0.71073	0.71073
Crystal system	Monoclinic	Tetragonal
Space group	$P2_1/c$	$I4/m$
a/Å	18.7617(8)	17.1313(6)
b/Å	21.4672(9)	17.1313(6)
c/Å	20.4528(8)	20.8643(6)
α/°	90	90
β/°	90.527(4)	90
γ/°	90	90
Volume/Å^3	8237.2(6)	6123.3(5)
Z	4	8
Reflection collected/unique	114625/18933	38785/3642
Final R indices [$I >$ 2sigma(I)]	R_1 = 0.0896, wR_2 = 0.1742	R_1 = 0.1137, wR_2 = 0.3326
R indices (all data)	R_1 = 0.2122, wR_2 = 0.2240	R_1 = 0.1690, wR_2 = 0.3747
$\Delta\rho_{max}$, $\Delta\rho_{min}$/e Å^{-3}	0.50/-0.42	1.07/-0.48
CCDC No.	1992245	2008279

Table 3-5 Summary of crystal data of **3** and **4**.

	3	**4**
Empirical formula	$C_{42}H_{53}F_{12}N_9O_{10}P_2$	$C_{49}H_{59}Br_2N_9O_{11.9}$
Formula weight	1133.87	1104.15
Temperature/K	123 (2)	123 (2)
Wavelength/Å	1.54184	0.71073
Crystal system	Triclinic	Triclinic
Space group	*P-1*	*P-1*
a/Å	8.6426(3)	7.8313(4)
b/Å	17.2337(6)	24.9650(13)
c/Å	18.5797(3)	26.4024(13)
α/°	109.028(3)	75.376(4)
β/°	99.333(2)	84.342(4)
γ/°	91.867(3)	88.1401(4)
Volume/Å^3	2570.64(14)	4970.2(4)
Z	2	4
Reflection collected/unique	23324/7882	68436/17624
Final *R* indices [*I* > 2sigma(*I*)]	R_1 = 0.0663, wR_2 = 0.1747	R_1 = 0.1177, wR_2 = 0.2609
R indices (all data)	R_1 = 0.1012, wR_2 = 0.2018	R_1 = 0.2463, wR_2 = 0.3372
$\Delta\rho_{max}$, $\Delta\rho_{min}$/e Å^{-3}	0.49/-0.30	1.21/-0.95
CCDC No.	1992372	2008208

3.4.4 TD-DFT Calculations

The calculations were performed using Gaussian 09 program. The structures were modeled from single crystal structures as initial models. HOMO and LUMO at the ground state were calculated using B3LYP function with 6-31+G (d,p) basis set. TD-DFT of radical cations was calculated by using MPW1PW91 function with 6-31+G (d,p) basis set. Solvent effects from DMF were approximated by a polarizable continuum model

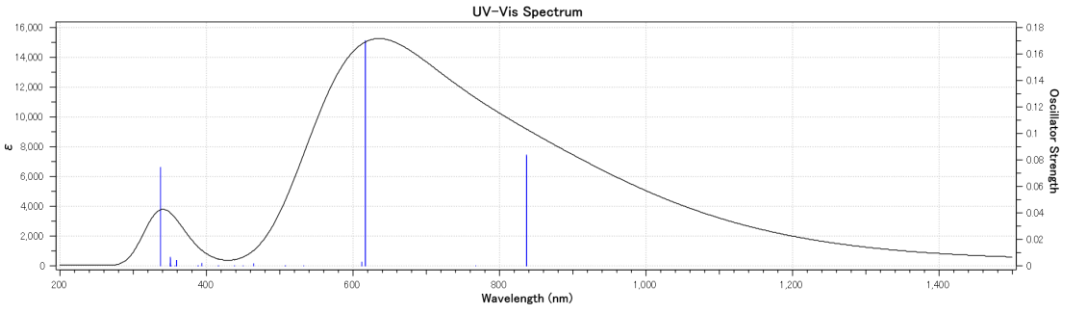

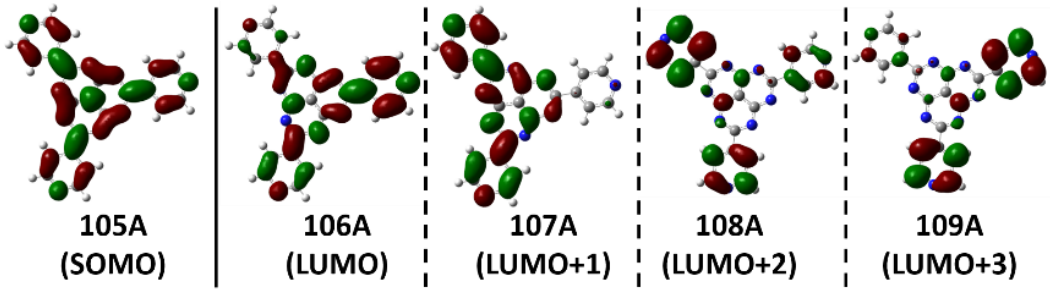

Excited State 3: 2.015-A 1.4815 eV 836.90 nm f=0.0827 <S2>=0.765**
105A ->107A 0.10498
105A ->108A 0.12687
105A ->109A 0.98091
Excited State 4: 2.015-A 1.4819 eV 836.69 nm f=0.0837 <S2>=0.765**
105A ->106A 0.10501
105A ->108A 0.98078
105A ->109A -0.12695

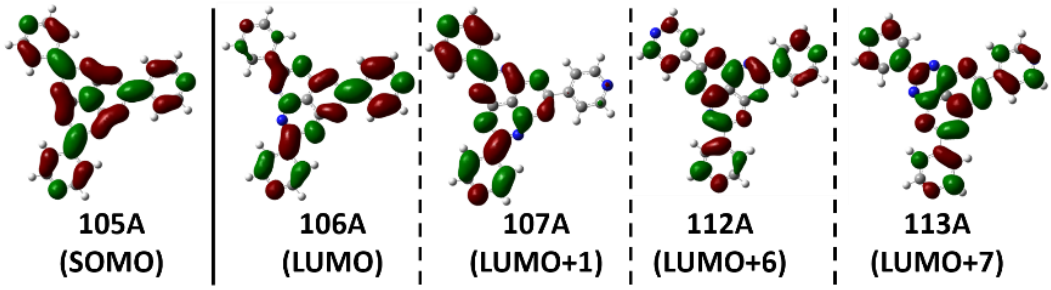

Excited State 6: 2.024-A 2.0099 eV 616.86 nm f=0.1685 <S2>=0.774**
105A ->107A 0.13030
105A ->112A 0.20149
105A ->113A 0.95799
Excited State 7: 2.024-A 2.0101 eV 616.80 nm f=0.1701 <S2>=0.774**
105A ->106A 0.13029
105A ->112A 0.95790
105A ->113A -0.20149

Figure 3-14 Simulated absorption spectrum, oscillator strength of $TPHAP^{2-\bullet}$ obtained by TD-DFT calculations and molecular orbitals, SOMO and LUMO, for the excited states 3, 4, 6, and 7.

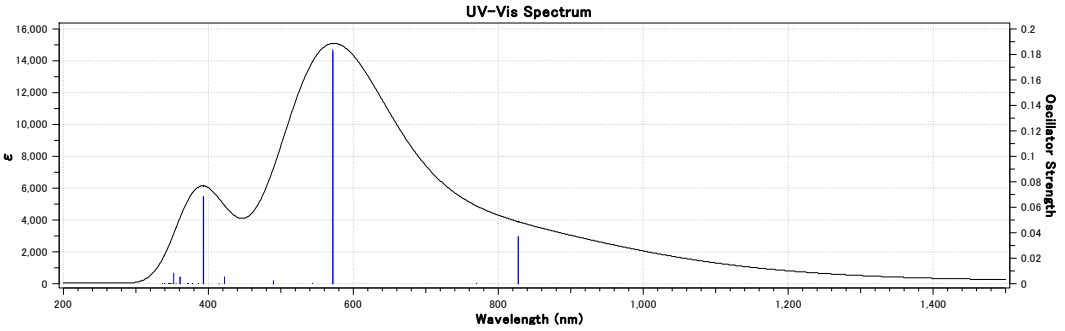

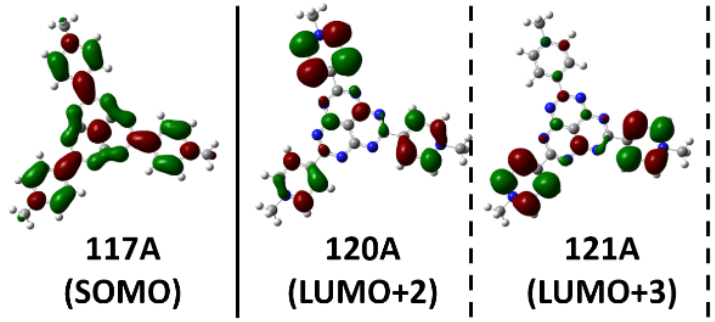

Excited State 3: 2.020-A 1.4980 eV 827.69 nm f=0.0365 <S**2>=0.770
117A ->120A 0.40184
117A ->121A 0.91004
Excited State 4: 2.020-A 1.4982 eV 827.58 nm f=0.0370 <S**2>=0.770
117A ->120A 0.90985
117A ->121A -0.40208

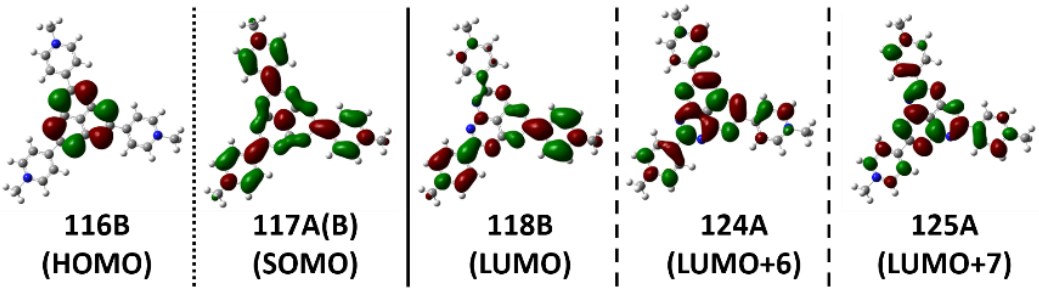

Excited State 6: 2.063-A 2.1684 eV 571.78 nm f=0.1817 <S**2>=0.814
117A ->124A -0.52381
117A ->125A 0.82719
116B ->118B 0.10438
Excited State 7: 2.064-A 2.1688 eV 571.67 nm f=0.1838 <S**2>=0.815
117A ->124A 0.82708
117A ->125A 0.52376
116B ->117B -0.10483

Figure 3-15 Simulated absorption spectrum, oscillator strength of $[Me_3TPHAP]^{+\bullet}$ obtained by TD-DFT calculations and molecular orbitals, SOMO and LUMO, for the excited states 3, 4, 6, and 7.

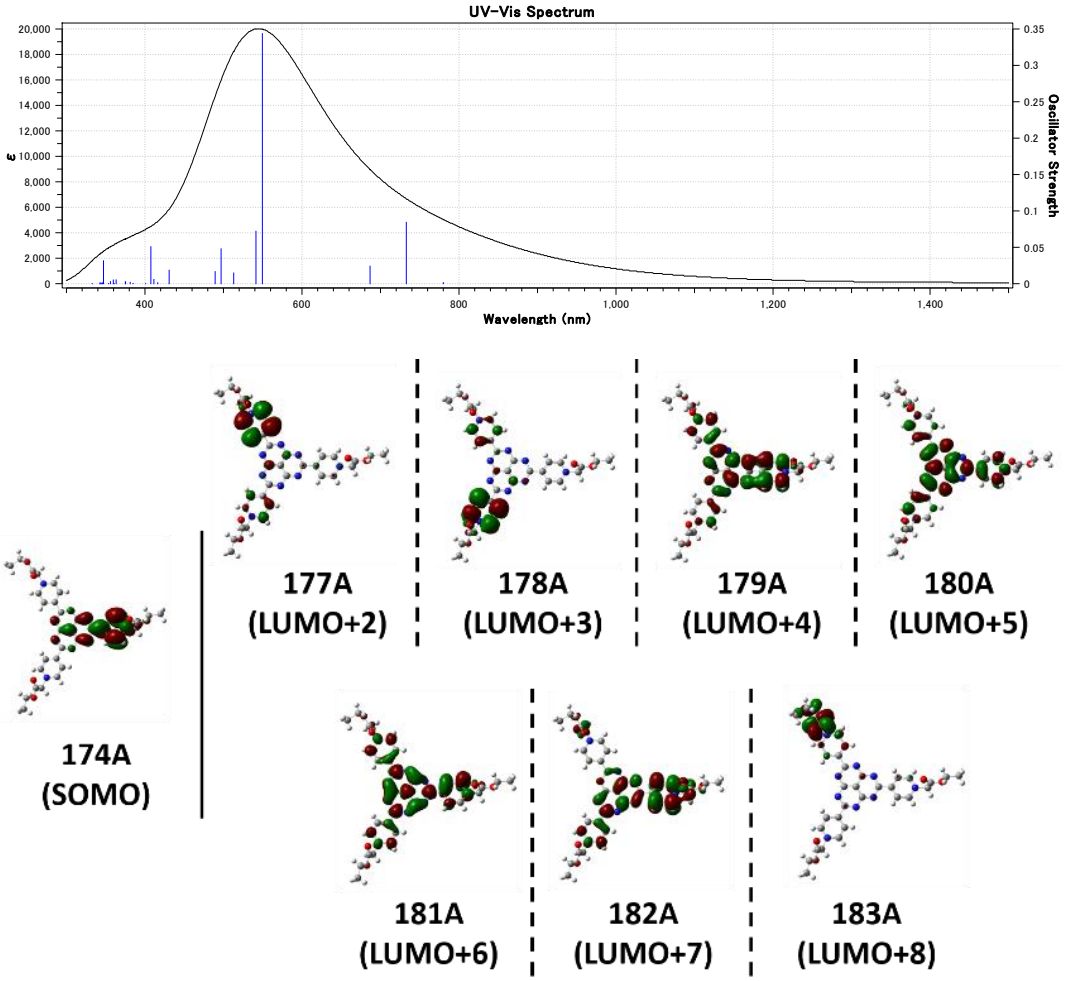

Excited State 4: 2.016-A 1.6918 eV 732.86 nm f=0.0843 <S**2>=0.766
174A ->177A 0.96054
174A ->178A 0.15454
174A ->179A -0.12170
174A ->180A 0.10629
174A ->182A -0.11493
Excited State 6: 2.074-A 2.2561 eV 549.55 nm f=0.3436 <S**2>=0.825
174A ->177A -0.12215
174A ->179A 0.33604
174A ->180A 0.72309
174A ->181A 0.48067
174A ->182A -0.23348
174A ->183A -0.10241

Figure 3-16 Simulated absorption spectrum, oscillator strength of [(Ethyl acetate)$_3$TPHAP]$^{+\bullet}$ obtained by TD-DFT calculations and molecular orbitals, SOMO and LUMO, for the excited states 4, and 6.

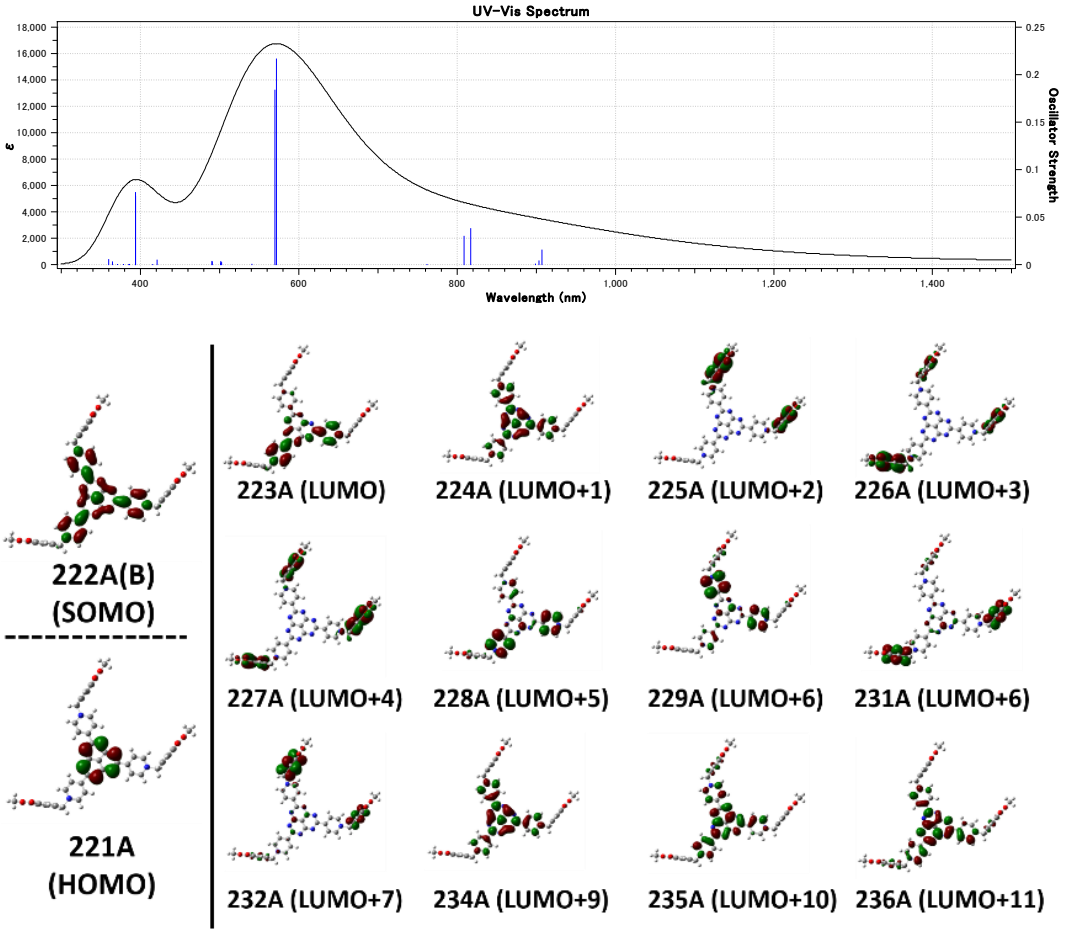

Excited State 3: 2.011-A 1.3669 eV 907.05 nm f=0.0153 <S**2>=0.761
222A -> 225A 0.86446 222A -> 229A 0.27944
222A -> 226A -0.41028
Excited State 6: 2.019-A 1.5175 eV 817.02 nm f=0.0378 <S**2>=0.769
222A -> 226A -0.13485 222A -> 228A 0.95581
222A -> 227A -0.22296
Excited State 7: 2.019-A 1.5331 eV 808.73 nm f=0.0298 <S**2>=0.769
222A -> 225A -0.27818
222A -> 229A 0.94916
Excited State 9: 2.065-A 2.1685 eV 571.75 nm f=0.2164 <S**2>=0.816
221A -> 224A 0.10271 222A -> 235A 0.91446
222A -> 232A -0.30619 221B -> 222B -0.10582
222A -> 234A 0.14797
Excited State 10: 2.066-A 2.1760 eV 569.78 nm f=0.1836 <S**2>=0.817
221A -> 223A 0.10517 222A -> 236A 0.88084
222A -> 231A -0.39578 221B -> 223B -0.10671
222A -> 234A 0.11849

Figure 3-17 Simulated absorption spectrum, oscillator strength of [(Methyl *p*-toluate)$_3$TPHAP]$^{+\bullet}$ obtained by TD-DFT calculations and molecular orbitals, SOMO and LUMO, for the excited states 3, 6, 7, 9, and 10.

3.5 References

1. Stuart, M. A. C.; Huck, W. T. S.; Genzer, J.; Müller, M.; Ober, C.; Stamm, M.; Sukhorukov, G. B.; Szleifer, I.; Tsukruk, V. V.; Urban, M.; Winnik, F.; Zauscher, S.; Luzinov, I.; Minko, S., *Nat. Mater.* **2010,** *9* (2), 101-113.
2. Mrinalini, M.; Prasanthkumar, S., *ChemPlusChem* **2019,** *84* (8), 1103-1121.
3. Ding, J.; Zheng, C.; Wang, L.; Lu, C.; Zhang, B.; Chen, Y.; Li, M.; Zhai, G.; Zhuang, X., *J. Mater. Chem. A* **2019,** *7* (41), 23337-23360.
4. Melánová, K.; Cvejn, D.; Bureš, F.; Zima, V.; Svoboda, J.; Beneš, L.; Mikysek, T.; Pytela, O.; Knotek, P., *Dalton. Trans.* **2014,** *43* (27), 10462-10470.
5. Sogo, P. B.; Nakazaki, M.; Calvin, M., *J. Chem. Phys.* **1957,** *26* (5), 1343-1345.
6. Reid, D. H., *Q. REV. CHEM. SOC.* **1965,** *19* (3), 274-302.
7. Uchida, K.; Kubo, T., *J. Synth. Org. Chem Jpn.* **2016,** *74* (11), 1069-1077.
8. Small, D.; Zaitsev, V.; Jung, Y.; Rosokha, S. V.; Head-Gordon, M.; Kochi, J. K., *J. Am. Chem. Soc.* **2004,** *126* (42), 13850-13858.
9. Goto, K.; Kubo, T.; Yamamoto, K.; Nakasuji, K.; Sato, K.; Shiomi, D.; Takui, T.; Kubota, M.; Kobayashi, T.; Yakusi, K.; Ouyang, J., *J. Am. Chem. Soc.* **1999,** *121* (7), 1619-1620.
10. Morita, Y.; Aoki, T.; Fukui, K.; Nakazawa, S.; Tamaki, K.; Suzuki, S.; Fuyuhiro, A.; Yamamoto, K.; Sato, K.; Shiomi, D.; Naito, A.; Takui, T.; Nakasuji, K., *Angew. Chem. Int. Ed.* **2002,** *41* (10), 1793-1796.
11. Suzuki, S.; Fukui, K.; Fuyuhiro, A.; Sato, K.; Takui, T.; Nakasuji, K.; Morita, Y., *Org. Lett.* **2010,** *12* (21), 5036-5039.
12. Tsuyoshi, M.; Yasushi, M.; Kozo, F.; Koichi, T.; Hideki, Y.; Gunzi, S.; Kazuhiro, N., *Bull. Chem. Soc. Jpn.* **2006,** *79* (6), 894-913.
13. Yakiyama, Y.; Ueda, A.; Morita, Y.; Kawano, M., *Chem. Commun.* **2012,** *48* (86), 10651-10653.
14. Geraskina, M. R.; Dutton, A. S.; Juetten, M. J.; Wood, S. A.; Winter, A. H., *Angew. Chem. Int. Ed.* **2017,** *56* (32), 9435-9439.
15. Yakiyama, Y.; Lee, G. R.; Kim, S. Y.; Matsushita, Y.; Morita, Y.; Park, M. J.; Kawano, M., *Chem. Commun.* **2015,** *51* (31), 6828-6831.
16. Lee, G. R.; Ohtsu, H.; Koo, J.; Yakiyama, Y.; Park, M. J.; Inoue, D.; Hashizume, D.; Kawano, M., *Chem. Commun.* **2016,** *52* (20), 3962-3965.
17. Nakanishi, K.; Ohtsu, H.; Fukuhara, G.; Kawano, M., *Chem. Eur. J.* **2019,** *25* (66), 15182-15188.
18. Geng, R.; Hou, X.; Sun, Y.; Yan, C.; Wu, Y.; Zhang, H.-L.; Shao, X., *Mater. Chem. Front.* **2018,** *2* (8), 1456-1461.
19. Saito, M.; Shinokubo, H.; Sakurai, H., *Mater. Chem. Front.* **2018,** *2* (4), 635-661.
20. Kishi, N.; Li, Z.; Sei, Y.; Akita, M.; Yoza, K.; Siegel, J. S.; Yoshizawa, M., *Chem. Eur. J.* **2013,** *19* (20), 6313-6320.
21. Panja, S. K.; Srivastava, N.; Srivastava, J.; Prasad, N. E.; Noothalapati, H.; Shigeto, S.; Saha, S., *SSA* **2018,** *194*, 117-125.
22. Shivakumar, K.; Vidyasagar, A.; Naidu, A.; Gonnade, R. G.; Sureshan, K. M., *CrystEngComm* **2012,** *14* (2), 519-524.
23. Horowitz, S.; Trievel, R. C., *J. Biol. Chem.* **2012,** *287* (50), 41576-41582.

24. Dou, J.-H.; Zheng, Y.-Q.; Yao, Z.-F.; Yu, Z.-A.; Lei, T.; Shen, X.; Luo, X.-Y.; Sun, J.; Zhang, S.-D.; Ding, Y.-F.; Han, G.; Yi, Y.; Wang, J.-Y.; Pei, J., *J. Am. Chem. Soc.* **2015,** *137* (50), 15947-15956.
25. Durben, S.; Baumgartner, T., *Angew. Chem. Int. Ed.* **2011,** *50* (34), 7948-7952.
26. Zhan, T.-G.; Zhou, T.-Y.; Lin, F.; Zhang, L.; Zhou, C.; Qi, Q.-Y.; Li, Z.-T.; Zhao, X., *Org. Chem. Front.* **2016,** *3* (12), 1635-1645.
27. Berville, M.; Richard, J.; Stolar, M.; Choua, S.; Le Breton, N.; Gourlaouen, C.; Boudon, C.; Ruhlmann, L.; Baumgartner, T.; Wytko, J. A.; Weiss, J., *Org. Lett.* **2018,** *20* (24), 8004-8008.
28. Gosztola, D.; Niemczyk, M. P.; Svec, W.; Lukas, A. S.; Wasielewski, M. R., *J. Phys. Chem. A* **2000,** *104* (28), 6545-6551.
29. Reus, C.; Stolar, M.; Vanderkley, J.; Nebauer, J.; Baumgartner, T., *J. Am. Chem. Soc.* **2015,** *137* (36), 11710-11717.
30. Benniston, A. C.; Harriman, A.; Li, P.; Rostron, J. P.; Harrington, R. W.; Clegg, W., *Chem. Eur. J.* **2007,** *13* (28), 7838-7851.

Chapter 4

Hexaazaphenalene-based Pyridinium Ligands and their Photocatalytic Activity

Abstract

Carboxyl-pyridinium TPHAP analogues were prepared by a hydrolysis of the corresponding esters reported in Chapter 3 or direct N-alkylation of the pyridine groups. Crystal structures of the resultant pyridinium TPHAP-based ligands exhibited either a di-cationic or a zwitterionic states depending on the recrystallization method. The ligands displayed antiparallel slipped stacking arrangements similar to their ester counterparts. A coordination network, **Cu-NL 1**, composed of copper cations and **NL 1** was synthesized and structurally characterized. It was used as a photocatalyst for 1,5-dihydroxynaphthalene oxidation to explore the catalytic activity enhancement in the pyridinium-based TPHAP, expected due to the lowering of activation energy for the intramolecular charge transfer process.

4.1 Introduction

In Chapter 2, the ROSs generation ability of TPHAP and its Cd(II) network were investigated. The ground state of TPHAP can absorb UV light to promote the intramolecular charge transfer (ICT) transition, according to the DFT calculations. The resultant excited state could then further interact with oxygen molecules. The nature of ICT electronic transition involves a transfer of electron density from the HAP core to the three peripheral pyridyl groups. Its energy was decreased from 335 to 366 nm after N- alkylation of terminal pyridine groups (Figure 4-1), which altered their charge state from neutral to cationic. Therefore, the redshift of the ICT transition in the pyridinium-TPHAP system has a potential to enhance the efficiency of ROSs generation because of the increase in the molar absorption coefficient in the desired wavelength range. In this Chapter, the pyridinium modification featuring free carboxylates was implemented in TPHAP, to prepare a series of analogues. One of the derivatives, **NL 1**, was incorporated into a new copper-based coordination network (**Cu-NL 1**), which was investigated for its photocatalytic activity for the 1,5-DHN oxidation.

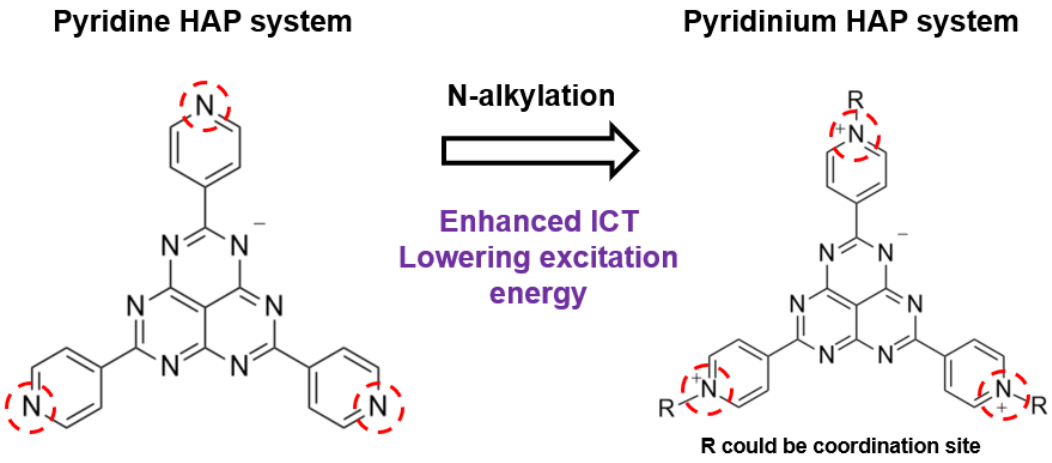

Figure 4-1 Pyridinium modification of TPHAP by N-alkylation reaction, resulting in the lowering of the ICT transition energy.

4.2 Results and Discussion

4.2.1 Synthesis of Pyridinium HAP-based Ligands and their Crystal Structures

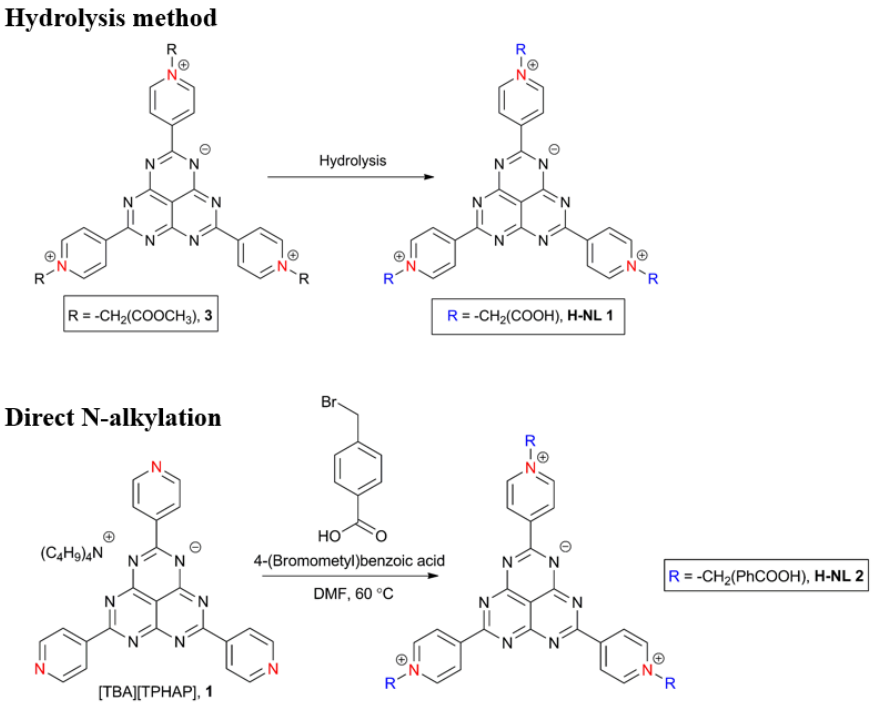

Scheme 4-1 Synthesis of pyridinium HAP-based ligands by hydrolysis method for **H-NL 1** (*top*) and direct N-alkylation for **H-NL 2** (*bottom*).

2,5,8-tris(1-(carboxylatomethyl)pyridine-l-ium)-1,3,4,6,7,9-hexaazaphenalene (**H-NL 1**) was successfully prepared by a base-catalyzed hydrolysis of the ester, [(Ethyl acetate)$_3$TPHAP]$^{2+}$ salt with LiOH. The final carboxylic acid product was precipitated by neutralization with 0.1 M HCl.[1, 2] In contrast, for 2,5,8-tris(1-(4-carboxybenzyl)pyridine-1-ium-4-yl)-1,3,4,6,7,9-hexaazaphenalene (**H-NL-2**), a direct N-alkylation of TPHAP salt by 4-(bromomethyl)benzoic acid was employed under mild heating in DMF solvent. It was found that a similar hydrolysis method starting from the ester, [(Methyl *p*-toluate)$_3$TPHAP]$^{2+}$ salt was unsuitable. It resulted in the formation of a dark brown solid composed of unidentifiable mixture of compounds, which could not be easily separated. The resultant **H-NL 1** and **H-NL**

2 compounds were crystallized, in order to determine their structures by X-ray diffraction analysis.

The single crystal of **H-NL 1**, chloride salt of [$(CH_2COOH)_3$TPHAP], was obtained by slow evaporation of hot aqueous solution. The crystal structure is shown in Figure 4-2. It composed of a di-cationic molecule surrounded by counter anions and included water of crystallization. Out of the three substituted carboxylate groups, two existed in a protonated carboxylic acid state, whereas the third one was deprotonated and carried a negative charge. When combined with the three cationic pyridinium units, total charge of the TPHAP molecule was +2, and was balanced out by two Cl^- anions in the structure.[3] The crystal structure packed in a monoclinic space group, $P2_1/c$ and contained slipped stacking dimers of pyridinium-TPHAP molecules. Two types of π-π distances were measures, as well as several hydrogen bonding interactions between carboxylic acids and water molecules.

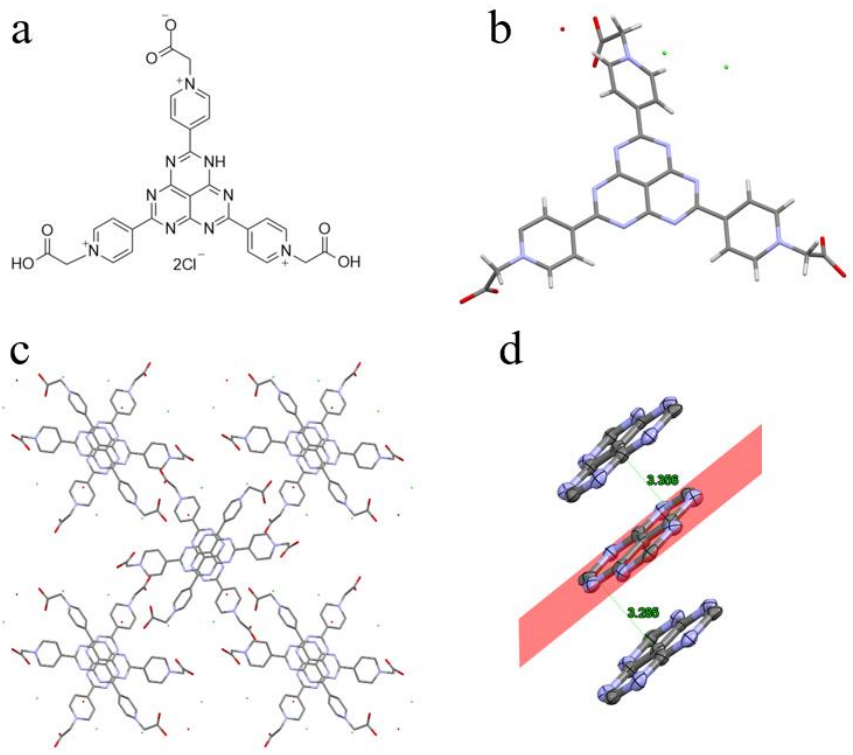

Figure 4-2 Crystal structure of **H-NL 1**. a) Chemical structure. b) Asymmetric unit. c) Packing arrangement of pyridinium-TPHAP d) π-π stacked dimers of the HAP cores. C – grey, H – white, N – blue, O – red, and Cl – green.

In addition, **H-NL 1** was converted to a neutral form, **Na-NL 1**, [$(CH_2COO)_2(CH_2COOH)$TPHAP], by neutralization with NaOH solution to improve its solubility. The crystal of the resultant compound was obtained by a layer diffusion in EtOH. The crystal structure is shown in Figure 4-3. In the crystal, pyridinium-TPHAP unit existed in a neutral zwitterionic state and did not require any counter ions for charge balance.[4, 5] In contrast to the chloride structure, two out of the three terminal groups were deprotonated carboxylates, and one was carboxylic acid. They coexisted with the three cationic pyridinium groups, and deprotonated HAP anion to give a total charge of zero. The crystal structure arranged in a lower symmetry triclinic space group, *P-1*, containing a slipped stacking dimer of pyridinium-TPHAP, similar to the structure of **H-NL 1**.

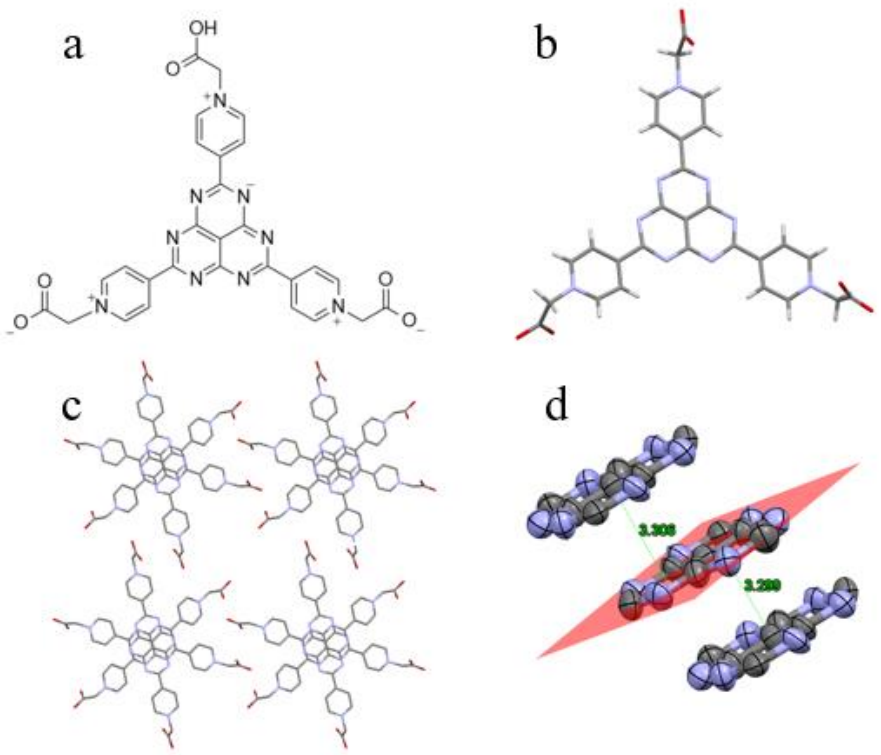

Figure 4-3 Crystal structure of **Na-NL 1**. a) Chemical structure. b) Asymmetric unit. c) Packing arrangement of pyridinium-TPHAP d) π-π stacked dimers of the HAP cores. C – grey, H – white, N – blue, and O – red.

The single crystal of the second carboxylate-pyridinium derivative, **H-NL 2**, was grown by a hydrothermal method at 130 °C (Figure 4-4). The molecule in the structure appeared in its zwitterionic state, in a similar fashion to **Na-NL 1**. It consisted of two individual zwitterionic pyridinium-TPHAP molecules surrounded by water molecules. The crystal structure packed in a monoclinic space group, $P2_1/c$ and featured antiparallel slipped stacking dimers with strong interdimer π-π interactions, as well as several hydrogen bonding interactions with the neighboring water molecules. Overall, this packing structure and the types of intermolecular interactions strongly resembled its ester analogue, [(Methyl *p*-toluate)$_3$TPHAP]$^{2+}$ salt. This molecule exhibited a strong tendency to dimerize, which caused it to precipitate out of solutions overtime, and therefore hindered its use in the network formation. Suitable reaction condition that would prevent this undesirable process and enable incorporation of this molecule into a network structure have not been discovered as of yet.

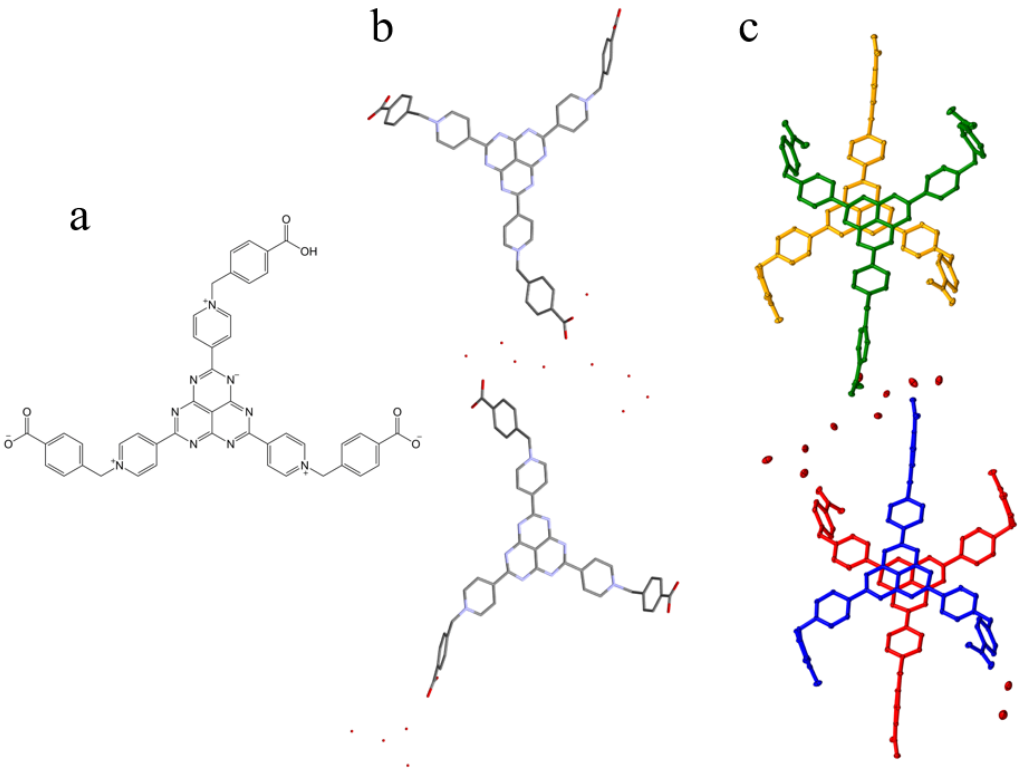

Figure 4-4 Crystal structure of **H-NL 2**. a) Chemical structure. b) Asymmetric unit view along the a-axis. c) π-π stacked dimers. Individual molecules are shown in different colors. All hydrogen atoms were omitted for clarity. C – grey, N – blue, and O – red.

4.2.2 Synthesis and Characterization of a Pyridinium HAP-based Coordination Network

Efforts to obtain a porous coordination network (PCN) using pyridinium-carboxylate TPHAP system were first focused on the **H-NL 1** ligand. For this purpose, several metal precursors were tested using hydrothermal synthetic conditions, which were necessary to increase the ligand solubility. The mixtures of transition metal halide salts (Zn(II), Ni(II) and Co(II)) and **H-NL 1** in DMF solvent were heated at 90 °C for one day. In each case, a crystalline solid was obtained, however, it was found to contain decarboxylation products of **H-NL 1**, methyl derivatives, Me_3TPHAP^{2+} salts, as shown in Figure 4-5. The single crystal of each compound had a general formula of $[Me_3TPHAP][MCl_4]$ (M = Zn, Ni or Co). Their structures were solved in a high symmetry rhombohedral space group, *R-3*. Each structure consisted of Me_3TPHAP^{2+} cation, with the charge balanced by a tetrahedral metal halide dianion[6, 7] located above the center of the HAP skeleton. It was previously reported by Kirchhecker *et. al.* that decarboxylation of zwitterionic pyridinium species could occur in acidic conditions at high temperature and pressure.[8] It was however unexpected that **H-NL 1** ligand was also susceptible to this process given that the network synthesis was carried out at milder conditions.

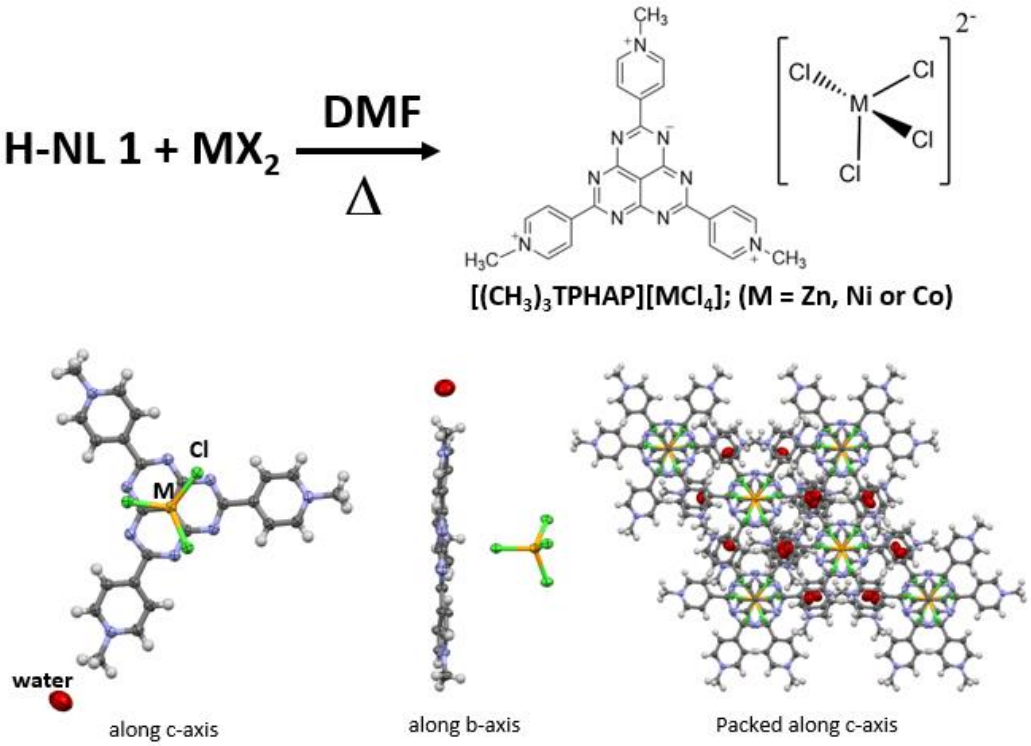

Figure 4-5 Decarboxylation of **H-NL 1** during network formation resulting in the isostructural series $[Me_3TPHAP][MCl_4]$ (M = Zn, Ni or Co).

To avoid ligand decarboxylation, it was necessary to use even milder network crystallization conditions and lower reaction temperatures. To achieve this, a more soluble form of the pyridinium-TPHAP, **Na-NL 1**, was employed. This molecule exhibits superior solubility in water and methanol relative to the chloride salt and has lower tendency to dimerize and precipitate out of the reaction mixture. Using this ligand, a new Cu(II)-based PCN, **Cu-NL 1**, [Cu(**NL 1**)2$(H_2O)_2$]·nH_2O was synthesized by a layer diffusion of **Na-NL 1** solution in water and $CuCl_2$ solution in methanol for two day. Single crystal X-ray analysis revealed that Cu(II) centers coordinated to three carboxylate groups from the two individual **NL 1** ligands and two water molecules to afford a distorted square pyramidal coordination sphere.[9] The square base of the pyramid was occupied by four oxygen atoms from two water molecules and two individual carboxylate groups of **NL 1** in a trans orientation. The Cu – O bond distances were measured to be 1.899(6) Å and 2.004(8) Å for the water molecules, and

1.930(6) Å and 2.025(6) Å for the carboxylates. The remaining carboxylate group was coordinated on the axial position with the elongated Cu – O bond distance of 2.331(9) Å, which was consistent with the expected Jahn-Teller distortion of the Cu(II) ion. Overall, **Cu-NL 1** crystallized in a triclinic space group, *P-1*, with 1D chain packing structure of pyridinium-TPHAP ligands intersected by narrow pore channels filled by water molecules. The bulk synthesis of **Cu-NL 1** was carried out by quick mixing of methanol solutions of **Na-NL 1** and $CuCl_2$, which produced a microcrystalline powder.

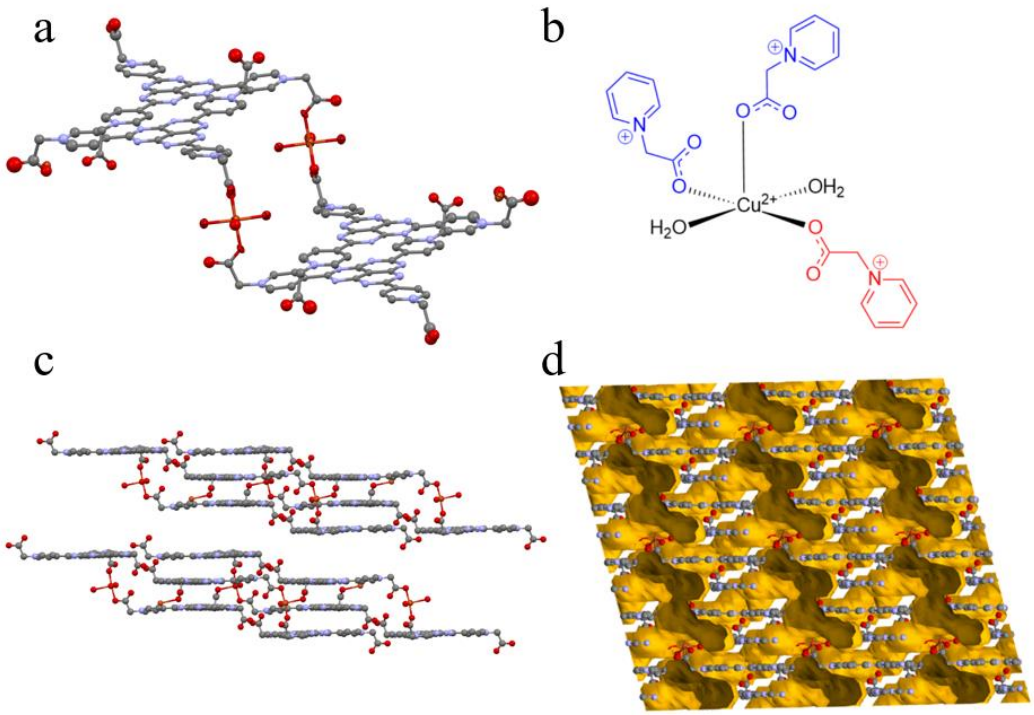

Figure 4-6 Crystal structure of **Cu NL 1**. a) Asymmetric unit structure. b) A distorted square pyramidal coordination environment of Cu(II). Individual molecules are shown in different colors. c) Packing structure. d) Porosity. All hydrogen atoms were omitted for clarity. C – grey, N – blue, O – red, and Cu – orange. Pore solvent molecules were omitted.

Solid state UV-Vis spectrum of **Cu-NL 1** was collected, as shown in Figure 4-7. The absorption of **Cu-NL 1** exhibited a broad band at around 360 nm, which was assigned to the intramolecular charge transfer transition arising from its pyridinium-TPHAP component, with the detailed discussion provided in Chapter 3. The shoulder absorption band at around 480 nm

resembled the absorption features of related Cu(II) compounds and was due to the ligand-to-metal charge transfer (LMCT).[10] In addition, the broad low energy absorption band above 600 nm was attributed to the d-d transition of Cu(II) centers.[11, 12]

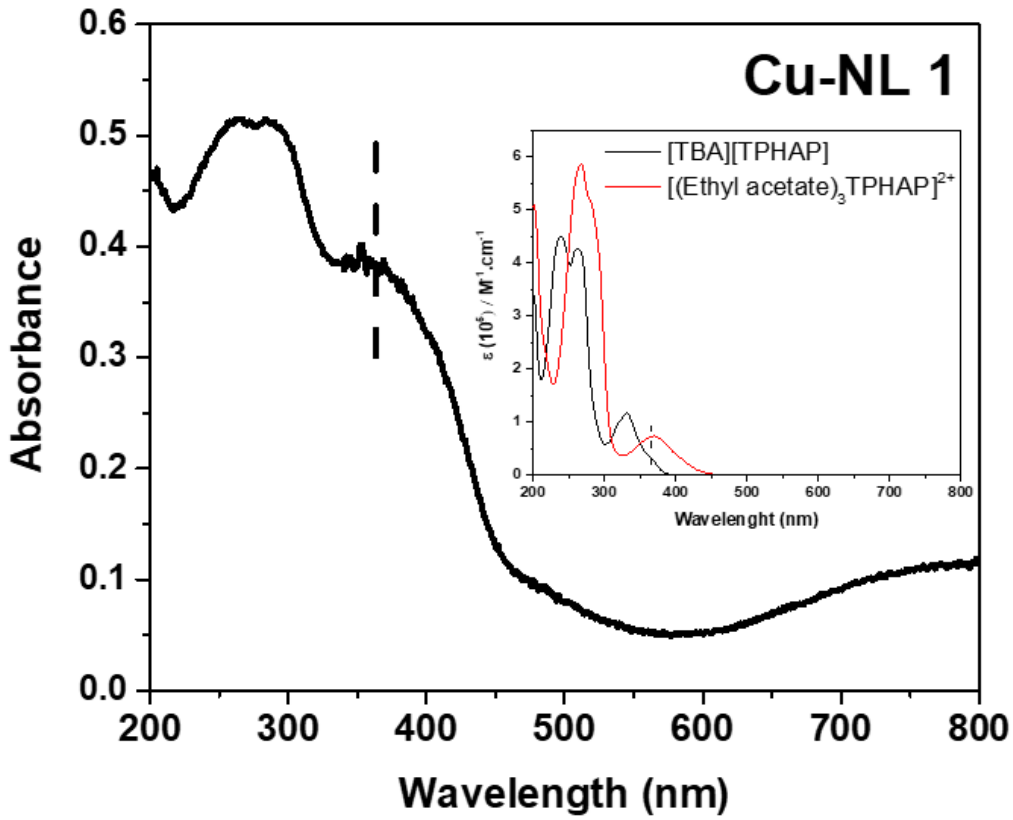

Figure 4-7 Solid state absorption spectrum of **Cu-NL 1**. Inset shows the absorption spectra of [TBA][TPHAP] and the ethyl ester analogue of **H-NL 1**, measured in MeCN solution.

4.2.3 Photocatalytic Activity towards 1,5-DHN Oxidation

The precursor to the **NL 1** ligand, the ester $[(\text{Ethyl acetate})_3\text{TPHAP}]^{2+}$ salt and **Cu-NL 1** were investigated for their photocatalytic activity towards 1,5-DHN oxidation using similar experimental conditions as described in Chapter 2. First, the catalytic performance of the ester compound was compared to the undecorated TPHAP compound in the homogeneous system. It was more convenient to use this analogue, rather than **H-NL 1** or **Na-NL 1**, due to its higher solubility in the MeCN reaction solvent. The juglone production was increased (inset of Figure

4-8) compared to TPHAP because the excitation energy of the UV light source (monochromatic light at 360 nm) better overlapped with the ICT absorption band, as shown in Figure 4-7 (inset). These results indicated that lowering of the ICT transition energy due to the pyridinium modification was a successful strategy for the enhancement of photocatalytic reaction rates. However, the pyridinium compound showed a change in its absorption spectrum after continuous UV irradiation, suggesting that a photodegradation was occurring (Figure 4-9). Similar to other pyridinium derivatives, it was postulated that the photosensitizer was promoting free radical homolytic or heterolytic C-N bond dissociation pathways under light irradiation.[13, 14] However, it appeared that the overall photostability of the [(Ethyl acetate)$_3$TPHAP]$^{2+}$ salt was comparable with that of the unmodified TPHAP, even though the nature of decomposition pathways might have differed between the two compounds.

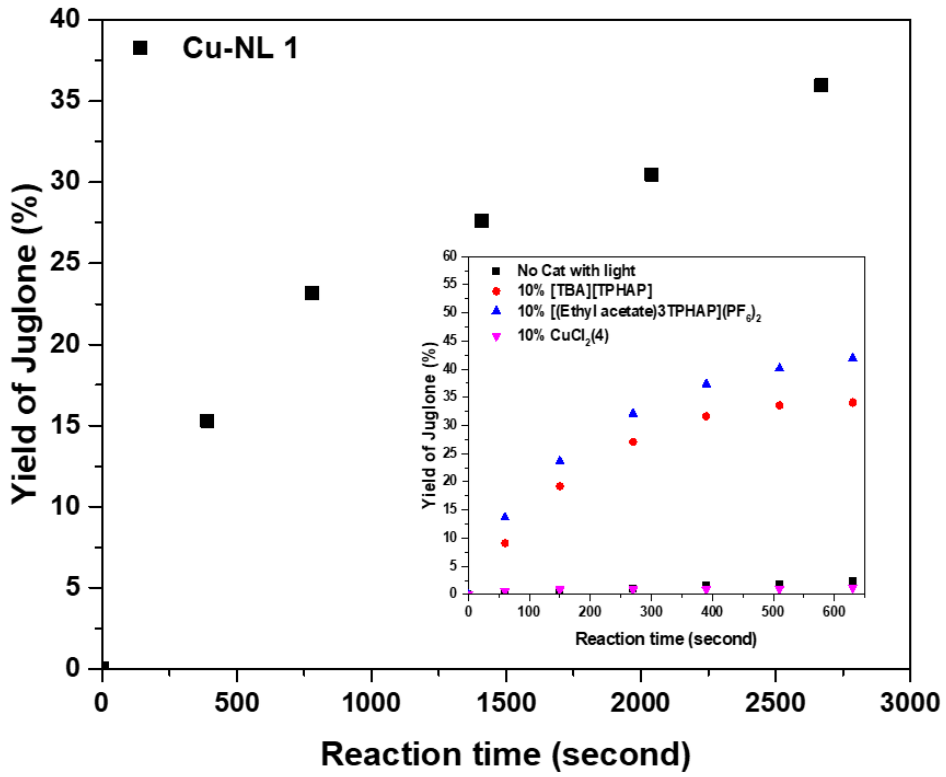

Figure 4-8 Yield of juglone plotted against irradiation time for the photooxidation of 1,5-DHN using **Cu-NL 1** as a photocatalyst. Inset shows the juglone production catalyzed by other compounds.

After the pyridinium-TPHAP ligand was incorporated into the **Cu-NL 1** network scaffold, it was tested as a heterogeneous photocatalyst for the 1,5-DHN oxidation. The catalytic performance is shown in Figure 4-8, and the data suggested that the singlet oxygen generation ability and photocatalytic activity were largely maintained inside the network structure. However, longer reaction time was necessary to achieve the same juglone production yield. This behavior was attributed to the lack of accessible pore space in the **Cu-NL 1**, which likely limited the activity to the photosensitizer centers on the surface of the network particles.

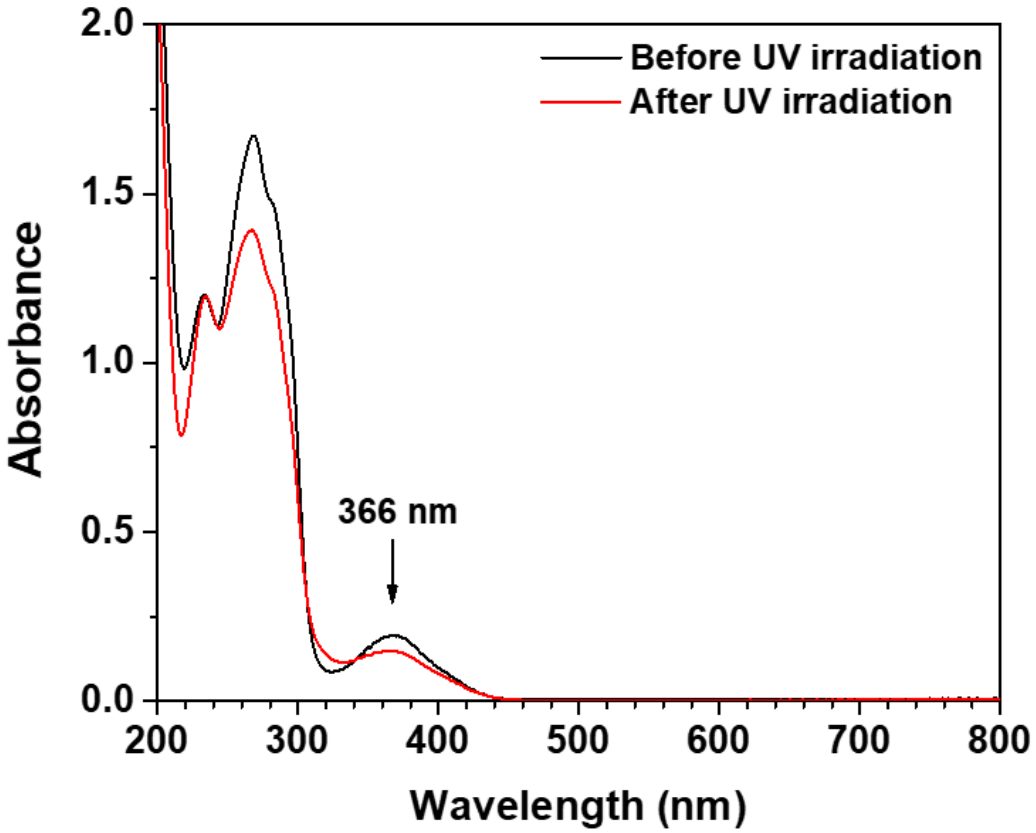

Figure 4-9 Absorption spectra change of $[(\text{Ethyl acetate})_3\text{TPHAP}]^{2+}$ salt solution in MeCN upon photoirradiation measured at 0 and 5 min.

The PXRD patterns of **Cu-NL 1**, before and after the reaction, confirmed that the network structure was mostly retained, as evident from the most intense diffraction peaks (Figure 4-10). The broadening of the diffraction peaks was tentatively attributed to the disruption of the hydrogen bonded water network in the photocatalytic reaction mixture, which could have led

to the distortions of the coordinated network itself. FTIR spectroscopy was also performed to further confirm photostability of the heterogeneous photosensitizer. The spectra contained a peak at around 1192 cm^{-1}, attributed to the exocyclic C-N bond and peaks at around 1602 and 1644 cm^{-1}, which were due to carboxylate stretching modes. These spectroscopic features were largely retained after the photocatalytic reaction,[15, 16] These results suggested that both, the structure of the **Cu-NL** network and the pyridinium-TPHAP ligands inside it were stable under the 1,5-DHN photooxidation reaction conditions.

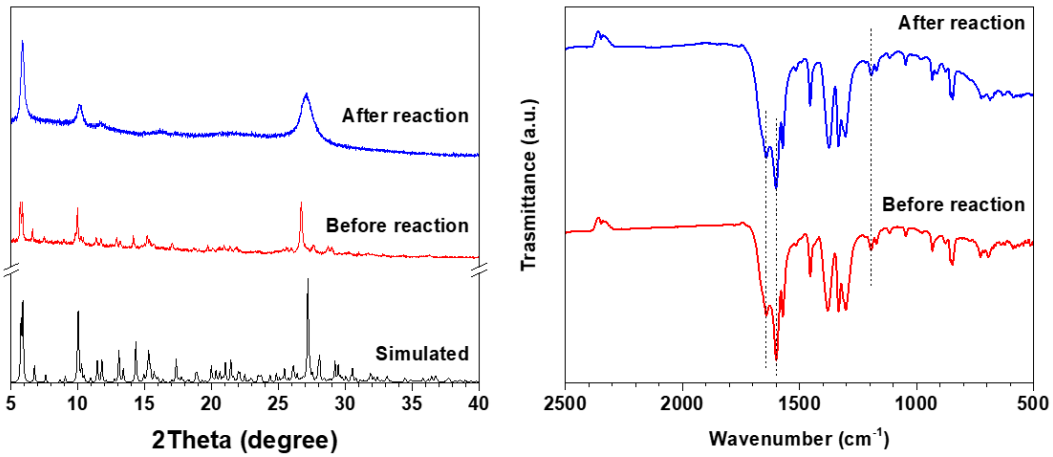

Figure 4-10 Powder X-ray diffraction patterns (*left*) and FTIR spectra (*right*) of **PCN 1** before and after photocatalytic 1,5-DHN oxidation reaction.

4.3 Conclusion

Two new carboxylic acid substituted pyridinium-TPHAP analogues were successfully synthesized and their crystal structures elucidated. The resultant compounds exhibited di-cationic and zwitterionic charge states depending on crystallization method. Carboxylic acid/carboxylate derivatives obtained from the corresponding ester substituted pyridinium-TPHAP retained similar intermolecular interactions, such as π-π stacking and hydrogen bonding from the HAP skeleton, in their crystal structures. The synthesis of **Cu-NL 1** was achieved using neutral **Na-NL 1** form under mild conditions. On the other hand, when the network formation was attempted using **H-NL 1** and **H-NL 2** under hydrothermal conditions, decarboxylation of the ligand was observed instead. The resultant methyl pyridinium anions

crystallized with tetrahedral transition metal halide cations. The lowering of the ICT transition energy in pyridinium motifs led to the enhancement of the juglone production. The absorption band of the $[(\text{Ethyl acetate})_3\text{TPHAP}]^{2+}$ salt closely aligned with the UV light source, thus enabling more efficient light harvesting. Although **Cu-NL 1** network displayed a slower rate for the conversion of 1,5-DHN into juglone, it nevertheless was able to achieve similar yields compared to the homogeneous TPHAP derivatives, thus retaining its single oxygen generation ability. Furthermore, the structural stability of the network was confirmed, showing that it was more robust towards prolonged UV irradiation than the free ligands.

4.4 Experimental Section

4.4.1 Materials and Methods

All reagents were purchased from commercial sources and used without further purification. $[(\text{Ethyl acetate})_3\text{TPHAP}]^{2+}$ and $[(\text{Methyl p-toluate})_3\text{TPHAP}]^{2+}$ salts were synthesized as described in the Chapter 3. ^{1}H NMR spectra were recorded in deuterated DMSO-d_6 as a solvent on a JEOL JNM-ECA400 II spectrometer at 400 MHz and referenced with the residual peak at 2.48 ppm. Elemental analyses were performed on an Elementar vario MICRO cube. UV-Vis absorption and diffuse reflectance spectra were recorded on JASCO V-770 and JASCO V-670 spectrophotometers. Powder X-ray diffraction was measured on a RIGAKU SmartLab diffractometer using a Cu Kα X-ray source. FT-IR spectra were collected using a FT/IR-610 JASCO spectrometer.

4.4.2 Synthesis

4.4.2.1 Synthesis of 2,5,8-tris(1-(carboxylatomethyl)pyridine-l-ium)-HAP (H-NL 1)

$[(\text{Ethyl acetate})_3\text{TPHAP}]\text{Br}_2$ (600 mg, 0.73 mmol) was dissolved in 80 % EtOH (40.0 mL) in a 250-mL round bottom flask. 1.0 M lithium hydroxide solution (2.5 mL) was added to the solution and the mixture was stirred at room temperature for 2 h. Then, 0.1 M hydrochloric acid solution was added to adjust pH to 2. The resulting precipitate was filtered, washed with

cold water (2 × 10 mL) and dried under vacuum at 80 °C to give **H-NL 1** (440 mg, 93 %); ^{1}H NMR (400 MHz, DMSO-d_6): δ9.215 (d, 6H, J = 6.41 Hz), δ9.088 (d, 6H, J = 6.87 Hz), δ5.679 (s, 6H).

4.4.2.2 Synthesis of 2,5,8-tris(1-(4-carboxybenzyl)pyridine-l-ium)-HAP (H-NL 2)

[TBA][TPHAP] (322 mg, 0.5 mmol) and methyl 4-(bromomethyl)benzoic acid (367 mg, 1.75 mmol) were dissolved in DMF (8.0 mL) in a 50 mL round bottom flask. The mixture was stirred at 60 °C for overnight. After cooling down, Et_2O (20.0 mL) was added to the reaction mixture to obtain a bright yellow slurry. The resultant precipitate was filtered and washed with dichloromethane (2 × 25 mL) and Et_2O (2 × 25 mL). The yellow powder was dried in ambient condition to give **H-NL 2** (420 mg, 84 %); ^{1}H NMR (400 MHz, DMSO-d_6): δ13.162 (br, 2H) δ9.366 (d, 6H, J = 6.60 Hz), δ9.031 (d, 6H, J = 7.15 Hz), δ8.008 (d, 6H, J = 8.25 Hz), δ7.672 (d, 6H, J = 8.25 Hz), δ6.071 (s, 6H).

4.4.2.3 Synthesis of Cu-NL 1

The single crystals were grown by a layer diffusion method. where a 0.5 mL aqueous solution of **Na-NL 1** (5 mg, 0.0086 mmol) was a bottom layer, 0.3 mL of mixed 1:1 MeOH/water was a middle layer, and 0.5 mL MeOH solution of $CuCl_2$ (20 mg, 0.15 mmol) was a top layer at room temperature. After 2 days, pale green crystals were obtained. The bulk synthesis was carried out by stirring 2 mL MeOH solution of **Na-NL 1** (6.2 mg, 0.01 mmol) and 1 mL MeOH solution of $CuCl_2$ (6.7 mg, 0.05 mmol) at room temperature for 30 min. The resultant suspension was filtered and washed with water and MeOH. The pale green crystalline powder was dried in ambient condition to give **Cu-NL 1**. The phase purity of the product was confirmed by PXRD. Anal. Calcd for $CuC_{56}H_{86.54}N_{18}O_{37.27}$=$((C_{28}H_{18}N_9O_6)_2(Cu)(H_2O)_2)\cdot 23.27(H_2O)_2$: C, 40.23; H, 5.22; N, 15.08. Found: C, 40.23; H, 5.10; N, 15.08.

4.4.3 Photooxidation of 1,5-DHN

Homogeneous conditions: 1,5-DHN (1×10^{-4} M) and 10 % of the catalyst were dissolved in 3.5 mL of MeCN and placed into a 3.5-mL quartz cuvette with a magnetic bar. The solution was stirred at 500 rpm while being irradiated by a 55W UV-LED (λ_{max} = 365 nm) (ZUV-C30H, Omron) under ambient condition. The UV-Vis spectra were recorded at interval times from 0 to 630 seconds.

Heterogeneous conditions: 1,5-DHN (1×10^{-4} M) in 3.5 mL of MeCN and 10 mg of **Cu-NL 1** were placed into a 3.5-mL quartz cuvette with a magnetic bar. The suspension was stirred at 500 rpm while being irradiated by a 55W UV-LED (λ_{max} = 365 nm) (ZUV-C30H, Omron) under ambient condition. The UV-Vis spectra were recorded at interval time.

4.4.4 Single Crystal Structure Determination

The diffraction data of **H-NL 1** and **H-NL 2** were recorded using Rigaku Varimax diffractometer with Saturn system equipped Rigaku GNNP low temperature device using graphite-monochromated Mo Kα radiation (wavelength = 0.71073 Å). All diffraction images were processed using CrysAlis Pro software. The structures were solved by the direct method (SHELXT-2018) and refined by full-matrix least squares calculations on F^2 (SHELXL-2018) using the SHELX-TL program package. All non-hydrogen atoms were refined with anisotropic displacement parameters. All hydrogen atoms were created with ideal geometry and refined using a riding model.

H-NL 1 crystal: $C_{28}H_{17}N_9O_6Cl_2$, *M*r = 749.89, Monoclinic, *P2₁/c*, *a* =7.5678(7) Å, *b* = 20.8716(16) Å, *c* = 21.2988(19) Å, β = 94.303(8)°, *V* = 3354.7(5) Å^3, T = −150 °C, Z = 4, ρ_{calcd} = 1.485 g cm^{-3}, μ = 0.272 cm^{-1}, 7745 unique reflections with I>2σ (*I*), 367 parameters, 3.836°< θ <55.12°, R_1= 0.1209, wR_2= 0.3022, GOF = 0.968.

H-NL 2 crystal: $C_{92}H_{86}N_{18}O_{25}$, *M*r = 1843.78, Monoclinic, *P2₁/c*, *a* = 16.3020(5) Å, *b* = 26.8462(9) Å, *c* = 19.9136(7) Å, β = 90.872(3)°, *V* = 8714.1(5) Å^3, T = −150 °C, Z = 4, ρ_{calcd}

= 1.405 g cm^{-3}, μ = 0.105 cm^{-1}, 20122 unique reflections with I>2σ (*I*), 1250 parameters, 3.546°< θ < 55.118°, R_1= 0.0796, wR_2= 0.1841, GOF = 1.027.

The diffraction data of the **Na-NL 1** crystal was recorded on a ADSC Quantum 210 CCD diffractometer using synchrotron radiation (λ = 0.7000 Å) at 2D SMC beamline at the Pohang Accelerator Laboratory (PAL). The diffraction images were processed using HKL3000. The structures were solved by direct methods (SHELXS-97) and refined by full-matrix least squares calculations on F^2 (SHELXL-2014) using the SHELX-TL program package.

Na-NL 1 crystal: $C_{28}H_{26}N_9O_{18}$, *M*r = 776.58, Triclinic, *P-1*, *a* = 7.1260(14) Å, *b* = 17.259(3) Å, *c* = 17.902(4) Å, α = 93.17(3)°, β = 95.15(3)°, γ = 93.04(3)°, *V* = 2185.8(8) $Å^3$, T = −150 °C, Z = 2, ρ_{calcd} = 1.180 g cm^{-3}, μ = 0.097 cm^{-1}, 7215 unique reflections with I>2σ (*I*), 388 parameters, 2.254°< θ <59.15°, R_1= 0.1441, wR_2= 0.4120, GOF = 1.139.

The diffraction data of **Cu-NL 1** was collected on a Rigaku Synergy-R/DWTI APEX II instrument with a Hypix-6000HE detector in house. The structure was solved by direct/Patterson mixed methods (SHELXT-2018) and refined by full-matrix least squares calculations on F^2 (SHELXL-2018) using the SHELX-TL program package.

Cu-NL 1 crystal: $C_{56}HCuN_{18}O_{39.5}$, *M*r = 1620.28, Triclinic, *P-1*, *a* = 13.7350(5) Å, *b* = 17.687(2) Å, *c* = 17.993(2) Å, α = 119.416(12)°, β = 101.242(6)°, γ = 93.04(3)°, *V* = 96.182(7) $Å^3$, T = −150 °C, Z = 2, ρ_{calcd} = 1.484 g cm^{-3}, μ = 0.141 cm^{-1}, 14406 unique reflections with I>2σ (*I*), 1105 parameters, 6.756°< θ < 151.848°, R_1= 0.1243, wR_2= 0.3218, GOF = 1.080.

4.5 References

1. Konieczna, D. D.; Biller, H.; Witte, M.; Schmidt, W. G.; Neuba, A.; Wilhelm, R., *Tetrahedron* **2018,** *74* (1), 142-149.
2. Cheng, M.; Yang, X.; Zhang, F.; Zhao, J.; Sun, L., *The Journal of Physical Chemistry C* **2013,** *117* (18), 9076-9083.
3. Lin, J.; Pozharski, E.; Wilson, M. A., *Biochemistry* **2017,** *56* (2), 391-402.
4. Zhang, K.; Qi, X.; Yuan, B., *IUCrData* **2016,** *1* (10), x161641.
5. Alfonso, M.; Wang, Y.; Stoeckli-Evans, H., *Acta Crystallographica Section C* **2001,** *57* (10), 1184-1188.
6. Prout, C. K.; Murray-Rust, P., *J. Chem. Soc. A. Inorg. phys. theor.* **1969,** (0), 1520-1525.
7. Zhang, J.; Ye, L.; Wu, L., *J. Mol. Struct.* **2006,** *791* (1), 172-179.
8. Kirchhecker, S.; Tröger-Müller, S.; Bake, S.; Antonietti, M.; Taubert, A.; Esposito, D., *Green Chem.* **2015,** *17* (8), 4151-4156.
9. Wang, M.-S.; Cai, L.-Z.; Zhou, G.-W.; Guo, G.-C.; Huang, J.-S., *Inorg. Chem. Commun.* **2003,** *6* (7), 855-858.
10. Kim, H. K.; Yun, W. S.; Kim, M.-B.; Kim, J. Y.; Bae, Y.-S.; Lee, J.; Jeong, N. C., *J. Am. Chem. Soc.* **2015,** *137* (31), 10009-10015.
11. Cui, C.; Shi, D.; Nie, Z.; Song, L.; Ren, A.; Liu, C., *J. Cluster Sci.* **2020,** *31* (5), 983-988.
12. Fritzsche, J.; Ettlinger, R.; Grzywa, M.; Jantz, S. G.; Kalytta-Mewes, A.; Bunzen, H.; Höppe, H. A.; Volkmer, D., *Dalton. Trans.* **2019,** *48* (40), 15236-15246.
13. Taskin, O. S.; Erel-Goktepe, I.; Khan, M. A. A.; Pispas, S.; Yagci, Y., *J. Photochem. Photobiol. A* **2014,** *285*, 30-36.
14. Dadashi-Silab, S.; Doran, S.; Yagci, Y., *Chem. Rev.* **2016,** *116* (17), 10212-10275.
15. Hester, R. E.; Suzuki, S., *J. Phys. Chem.* **1982,** *86* (23), 4626-4630.
16. Lv, X.; Liu, C.; Song, S.; Qiao, Y.; Hu, Y.; Li, P.; Li, Z.; Sun, S., *RSC Adv.* **2018,** *8* (6), 2941-2949.

Chapter 5

Conclusions

5.1 Summary of Thesis

Porous coordination networks (PCNs) incorporating photosensitizers as one of their components have received considerable attention for their ability to induce ROSs generation upon light irradiation combined with the presence of accessible pores and other functionalities. However, the most commonly used ligands for the PCN construction do not possess the required light harvesting capabilities, which limits their utilization in photocatalytic transformations. In this doctoral thesis, I presented a series of materials based on the polycyclic hexaazaphenalene (HAP) anion, including pyridyl substituted analogue, TPHAP, pyridinium-TPHAP, as well as PCNs incorporating these molecules. The chief motivation for this study was the development of novel photocatalytic systems. The ROSs generation abilities and photostability of TPHAP derivatives were confirmed by spectroscopic analysis, selective oxidation reactions and X-ray diffraction analysis. Finally, the ability of these materials to oxidize a variety of substrates, including the inert hydrocarbons, through light irradiation was demonstrated.

In **Chapter 2**, the investigation of photophysical properties of TPHAP revealed that two distinct photochemical processes were occurring during light irradiation, namely charge transfer and energy transfer. The excitation was arising from the intramolecular charge transfer (ICT) of the TPHAP molecule. This excited state could then interact with oxygen molecules to promote the ROSs production. These ROSs were able to oxidize several hydrocarbon substrates, including alkanes. The photodegradation of TPHAP was minimized by immobilizing it inside a network structure, giving rise to the **PCN 1**. The heterogeneous photooxidation reactions of cyclohexane, cyclooctane and *n*-octane catalyzed by **PCN 1** displayed one of the highest catalytic among network catalysts. The photostability of this **PCN 1** was additionally confirmed by PXRD measurements and leaching tests. The deeper insights into the mechanism of alkane photooxidation were elucidated by using cyclohexane as a model substrate. It was found that the oxidation reaction was facilitated through both energy transfer and charge transfer processes.

In **Chapter 3**, Pyridinium-TPHAP derivatives were obtained by N-alkylation reactions of TPHAP. The electronic structures of these compounds indicated the increase in intermolecular interactions was due to the changes in molecular charges, electronic states, and redox properties. Pyridinium modification was limited to the three terminal pyridine groups while the HAP core remained unreacted. The resultant molecules were isolated in their di-cationic states. In crystal structures, the presence of three cationic pyridinium groups and the anionic HAP core led to shortened π-π distances within the stacked HAP dimers. This effect was attributed to the decrease in anion-anion repulsion between the HAP cores. The steric hindrance from alkyl groups, as well as appearance of additional weak interactions from Van der Waals forces and weak hydrogen bonding directly affected the overall structural arrangement. In solution state, the characteristic absorption bands of pyridinium analogues shifted to lower energy, whereas their reduction potentials occurred at less cathodic values. Moreover, the changes in the absorption spectra associated with the electrochemical reduction suggested that these compounds exhibited useful electrochromic properties. These results demonstrated the utility of the pyridine-to-pyridinium modification in enhancing the functionality of TPHAP and increasing the interactivity in its molecular packing.

In **Chapter 4**, the effect of the changes on electronic properties of the pyridinium-TPHAP system was tested by performing the 1,5-DHN photooxidation reaction. A series of carboxylate containing pyridinium-TPHAP derivatives was prepared and characterized by single crystal X-ray diffraction. The **Cu-NL 1** network was successfully synthesized from the **Na-NL 1** ligand. The lowering of ICT transition energy in the pyridinium-TPHAP systems was beneficial for their ability to generate ROSs and enhanced the catalytic activity of heterogenous photooxidation of 1,5-DHN. Furthermore, after incorporation into the network structure, the photostability of the ligand was improved. At the same time, **Cu-NL 1** was shown to retain its structural integrity even after prolonged light irradiation.

5.2 Outlook and Future Work

In this doctoral thesis, the use of TPHAP-based molecules as novel photosensitizer systems was reported for the first time. Their excellent photocatalytic performance was demonstrated by oxidation of inert alkane substrates. Mechanistic studies revealed the involvement of multiple ROSs in this reaction. These properties could be further improved through a pyridine-to-pyridinium modification of TPHAP molecule, which lowered the energy of the excitation band. Despite this progress, there is considerable room for further improvement of these photocatalytic systems.

Due to the remaining unidentified product mixture from cyclohexane oxidation, there is one way to avoid such over oxidation reaction from the current batch type reactor to flow type reactor due to the decrease of contacting time between target products and continued generated reaction oxygen species and other intermediate. The excitation of TPHAP primarily relied on the ICT transition between HAP core and the substituent groups. The energy of this transition, which is related to the HOMO-LUMO gap, could be further decreased to shift it to more practical visible light range. To achieve this, a series of systematic experimental and theoretical studies will need to be undertaken. The energy gap could be most straightforwardly modified by adjusting the energies of HOMO and LUMO. Thus, first, the HOMO energy level could be altered by replacing carbon on the phenalene core with other the elements (C, N, B). Second, the LUMO energy level could be affected by the judicious selection of substituent groups on the molecule periphery. In general, it is expected that the modification of LUMO level would be easier to achieve because the procedure for the synthesis of HAP derivatives with different functional group is already well-established. Attachment of different electron withdrawing groups, such as -COR, -NO_2, -CN, -CX_3, or -SO_3H, or electron donating groups, such as -NR_2, -OH, or -phenyl to the HAP core would result in a diverse family of compounds with systematically adjusted LUMO energy levels. In addition, several specific functional groups can also be incorporated using this method, which would add new unique properties and selective interactions with substrates or products. Moreover, substituents that can

participate in coordination to metal ions, such as carboxylic acid and pyrazole would also be highly desirable since they enable the construction porous coordination networks, which can be used to immobilize HAP-based photosensitizers inside robust solid-state scaffolds. Another drawback of the current TPHAP molecule is its relatively low molar extinction coefficient in the visible range, which leads to low quantum yields. Therefore, an increase in this parameter could significantly boost the photocatalytic performance. Herein, I propose to use theoretical methods to design the necessary modification of the HAP core by comparing the oscillator strengths from the TD-DFT calculations. The large oscillator strength typically affords high molar extinction coefficient.

To further understand the nature of photochemical processes of HAP analogues and phenalenyl systems in general, more sophisticated techniques could be employed for the in-depth evaluation, such as electron paramagnetic spectroscopy and emission spectroscopy for singlet oxygen detection, in addition to photoelectrochemical method, and transient absorption spectroscopy. Lastly, the design of photosensitizers based on the HAP system from better understanding of its photochemical processes could lead to the development of exceptionally efficient light harvesting molecules that can be applied to the photocatalytic transformations of many organic molecules.

Pyridine-to-pyridinium modification strategy used on TPHAP was effective in decreasing the excitation energy. However, the presently reported pyridinium-TPHAP molecules exhibited high conformational flexibility, arising from the presence of methylene bridges. This structural feature made these ligands poorly suitable for the construction of coordination networks. Decarboxylation reaction that occurred under solvothermal conditions limited the scope of possible network formation parameters. Moreover, while one network structure was obtained with Cu(II), it could not be activated without the collapse, thus limiting the availability of its internal pore space. Therefore, to improve the ligand properties it is necessary to change the synthetic strategy. Zincke reaction allows direct substitution of allyl groups, in what is known as N-allylation. This reaction permits modification of pyridine with

linear rigid substituents resulting in ligands with better defined coordination geometries and being able to structurally support large pores. Furthermore, the other photoactive molecules featuring excitations arising from similar ICT transitions, from HOMO located on the functional core to LUMO located on terminal pyridine groups, could also be suitable candidates for N-alkylation and N-allylation reactions as a way to enhance their light absorption properties and catalytic activities.

Acknowledgements

This is my first far from home odyssey. On the way, I had to face situations like tough time, tired, physically or mentally weak but there were still many people or the things always supporting me. I would like to thank people who supported me during my PhD journey in Tokyo Tech, Japan.

First of all, I would like to appreciate Professor Masaki Kawano, my supervisor for warmly welcoming me as a visiting student in POSTECH, Korea, 6 years ago and now as his PhD student in Tokyo Tech for more than 3 years. Under his guidance, I could learn several things not only research but also life that push me to succeed in this day.

Next, I would like to thank Dr. Jatuporn Wittayakun and Dr. Sirinuch Loiha, my former advisors from Thailand that always said to me that “Nick, you can do PhD in abroad” even I never think about it before and give me an opportunity to meet Professor Masaki Kawano for the first time in POSTECH. Dr. Hiroyoshi Ohtsu, an assistant professor in Kawano’s group, who supported me with several analysis techniques, research discussion and living in Japan for my research. Dr. Pavel M Usov, a researcher in Kawano’s group, my international friend, who help me a lot for electrochemistry, research idea, English skill, life’s discussion and lastly hang outs. Odagawa-san, Den-san, Wada-san, Okiyama-san, and Yamada-san who helped me to settle down in the early days and also prepare documents in Japanese language. Dr. Jooyeon Ha, Dr. Wanuk Choi, Dr. Jin Young Koo, Dr. Gil Ryeong Lee and Dr. Jaejun Kim, senior members for useful advice. My juniors in our group who have shared memorable memories: Nakanishi-san, Miho-chan, Kanamaru-san, Marie-chan, Furuno-chan, Asada-chan, Ona-san, Ichinose-san, Joonsik-san, Mikami-san, Shimada-san and Tagami-san.

Further, I would like to thank the things that could entertain me during hard times like beautiful nature, food and culture in Japan, Japanese manga/anime, YouTube/Netflix during lockdown from the pandemic. In addition, thanks for my family that they can support me **everything** physically, mentally from Thailand.

Finally, I gratefully acknowledge my full funding scholarship from Thai government under the Development and Promotion of Science and Technology Talents (DPST) Project for my PhD study.

Krittanun Deekamwong

Dec 2020